

FINAL REPORT

Measurement and Modeling of Volatile Particle Emissions from Military Aircraft

SERDP Project WP-1626

OCTOBER 2011

Allen L. Robinson
Carnegie Mellon University

This document has been cleared for public release



| | | | | | |
|--|-------------|-------------------------|-------------------------------|--|---|
| REPORT DOCUMENTATION PAGE | | | | <i>Form Approved</i> <i>OMB No. 0704-0188</i> | |
| The public reporting burden for this collection of information is estimated to average 1 hour per response, including the time for reviewing instructions, searching existing data sources, gathering and maintaining the data needed, and completing and reviewing the collection of information. Send comments regarding this burden estimate or any other aspect of this collection of information, including suggestions for reducing the burden, to the Department of Defense, Executive Services and Communications Directorate (0704-0188). Respondents should be aware that notwithstanding any other provision of law, no person shall be subject to any penalty for failing to comply with a collection of information if it does not display a currently valid OMB control number. | | | | | |
| PLEASE DO NOT RETURN YOUR FORM TO THE ABOVE ORGANIZATION. | | | | | |
| 1. REPORT DATE (DD-MM-YYYY) 03-10-2011 | | 2. REPORT TYPE Final | | 3. DATES COVERED (From - To) June 2008 - September 2011 | |
| 4. TITLE AND SUBTITLE Measurement and Modeling of Volatile Particle Emissions from Military Aircraft | | | | 5a. CONTRACT NUMBER | |
| | | | | 5b. GRANT NUMBER | |
| | | | | 5c. PROGRAM ELEMENT NUMBER | |
| | | | | 5d. PROJECT NUMBER WP-1626 | |
| 6. AUTHOR(S) Allen L. Robinson | | | | 5e. TASK NUMBER | |
| | | | | 5f. WORK UNIT NUMBER | |
| | | | | | |
| 7. PERFORMING ORGANIZATION NAME(S) AND ADDRESS(ES) Carnegie Mellon University 5000 Forbes Ave Pittsburgh, PA 15213 | | | | 8. PERFORMING ORGANIZATION REPORT NUMBER | |
| 9. SPONSORING/MONITORING AGENCY NAME(S) AND ADDRESS(ES) Strategic Environmental Research and Development Program 901 N. Stuart Street, Suite 203 Arlington, VA 22203 | | | | 10. SPONSOR/MONITOR'S ACRONYM(S) SERDP | |
| | | | | 11. SPONSOR/MONITOR'S REPORT NUMBER(S) | |
| | | | | | |
| 12. DISTRIBUTION/AVAILABILITY STATEMENT Approved for public release; distribution is unlimited | | | | | |
| 13. SUPPLEMENTARY NOTES | | | | | |
| 14. ABSTRACT Experiments were performed to characterize the atmospheric evolution of volatile particulate matter emissions from military aircraft engines including CFM56-family and T63 gas-turbine engines. The data were used to develop parameterizations for use in chemical transport models to predict the contribution of aircraft to ambient fine particulate matter. A significant fraction of the particulate matter emissions is semivolatile at atmospheric conditions. Therefore, a traditional emissions factor cannot be used to represent military aircraft particulate matter emissions in inventories and models. Instead, one must measure the total emissions rate of semivolatile species and the volatility distribution of the emissions. The smog chamber experiments demonstrated that photo-oxidation creates substantial secondary particulate matter, greatly exceeding (by as much as a factor of 60) the direct particulate emissions after an hour or less of aging at typical summertime conditions. Therefore secondary particulate matter production must be accounted for in order to assess the contribution of military aircraft emissions to urban and regional air pollution. | | | | | |
| 15. SUBJECT TERMS aircraft; emissions; air pollution; fine particulate matter; PM2.5; atmospheric chemistry; secondary organic aerosol | | | | | |
| 16. SECURITY CLASSIFICATION OF: | | | 17. LIMITATION OF ABSTRACT | 18. NUMBER OF PAGES | 19a. NAME OF RESPONSIBLE PERSON |
| a. REPORT | b. ABSTRACT | c. THIS PAGE | | | 19b. TELEPHONE NUMBER (Include area code) |

Reset

Table of Contents

| | |
|--|------|
| Table of Contents | i |
| List of Tables | iii |
| List of Figures | iv |
| List of Acronyms | viii |
| Keywords | x |
| Acknowledgements | xi |
| Abstract | 1 |
| Objectives | 3 |
| Background | 4 |
| Materials and Methods | 7 |
| Field Campaigns | 7 |
| Pittsburgh Tests | 8 |
| Wright Patterson Tests | 9 |
| Alternative Aviation Fuel Experiment (AAFEX) Tests | 11 |
| Emissions sampling | 12 |
| AAEFX sampling | 18 |
| Emissions Characterization | 19 |
| Dilution sampler | 19 |
| Smog chamber | 20 |
| AAFEX | 21 |
| Photochemical Aging | 21 |
| Data Analysis | 21 |
| Fuel-based emission factors | 21 |
| Secondary Aerosol Production | 21 |
| Thermodenuder data | 23 |
| Modeling | 23 |
| Volatility Basis Set | 23 |
| VBS Terminology | 24 |
| Traditional SOA (T-SOA) | 25 |
| Non-traditional SOA (NT-SOA) | 26 |

| | |
|--|-----|
| Results and Discussion | 29 |
| Pittsburgh Tests..... | 29 |
| Primary emissions of criteria and organic gases | 29 |
| Primary PM Mass Emissions | 30 |
| Low-Volatility Organic Emissions | 33 |
| Photo-oxidation and secondary aerosol production..... | 40 |
| Wright Patterson Tests..... | 49 |
| Gaseous Emissions..... | 49 |
| Particulate Matter Emissions | 50 |
| OC Speciation | 51 |
| Organic Aerosol Volatility..... | 53 |
| Photo-oxidation and secondary aerosol production..... | 55 |
| AAFEX Tests..... | 62 |
| Modeling..... | 65 |
| Input Data..... | 66 |
| T-SOA..... | 73 |
| Mass balance: NT-SOA formed versus POC reacted | 74 |
| NT-SOA | 75 |
| Conclusions and Implications for Future Research/Implementation..... | 82 |
| Hypothesis Testing..... | 83 |
| Research needs..... | 85 |
| Implementation | 86 |
| Literature Cited | 88 |
| Appendix A. Supporting Data..... | 96 |
| Appendix B. List of Scientific/Technical Publications..... | 106 |
| Articles in peer-reviewed journals | 106 |
| In preparation | 106 |
| Conference or symposium abstracts | 107 |

List of Tables

| | |
|--|-----|
| Table 1. Summary of tests conducted with the KC-135 Stratotanker at the Pittsburgh International Airport. | 8 |
| Table 2. Fuel properties of JP8 used for the KC-135 tests at the Pittsburgh International Airport. | 8 |
| Table 3. Summary of experiments conducted with the T63 engine at Wright Patterson Air Force Base. | 10 |
| Table 4. Select properties for JP-8 and FT fuels used in the Wright Patterson Tests. | 10 |
| Table 5. List of samples collected by Carnegie Mellon University during the AAFEX test. | 12 |
| Table 6. VOC species included in traditional SOA model. | 26 |
| Table 7. Criteria gas emission factors tests measured during the Pittsburgh test with the CFM56 engine..... | 29 |
| Table 8. Summary of primary aerosol emissions and secondary aerosol production measured during Pittsburgh tests of CFM56 engine. Uncertainty estimates are presented in parenthesis. | 31 |
| Table 9. Summary of aging conditions for experiments conducted at the Pittsburgh airport. | 44 |
| Table 10. Gaseous and particulate matter emissions factor s for a T63 engine measured during the Wright Patterson experiments. | 49 |
| Table 11. Results for photo-oxidation experiments conducted at Wright Patterson.. | 58 |
| Table 12. Pittsburgh and AAFEX emissions of low volatility organics. AAFEX data are for engine operating on JP8 fuel. | 64 |
| Table 13. SOA precursor emissions (mg kg-fuel ⁻¹) used in the SOA modeling. | 69 |
| Table 14. Parameters for hybrid NT-SOA model. | 81 |
| Table A1. VOC emission factors for CFM56 engine in mg kg-fuel ⁻¹ measured during Pittsburgh experiments..... | 96 |
| Table A2. Low-volatility organic emission factors (mg kg-fuel ⁻¹) for CFM56 engine measured from Tenax sorbent and quartz samples collected at the Pittsburgh airport..... | 99 |
| Table A3. VOC emission factors for T63 engine in mg kg-fuel ⁻¹ measured during Wright Patterson experiments..... | 101 |
| Table A4. Low-volatility organic emission factors (mg kg-fuel ⁻¹) for T63 engine measured from Tenax sorbent and quartz samples collected at the Wright Patterson Air Force Base..... | 104 |

List of Figures

| | |
|---|----|
| Figure 1. Time-series of N1 fan speed (% of maximum) and exhaust gas temperature for experiments conducted (a) 4% load, (b) 7% (c) 30% and (d) 85% engine loads for the experiments conducted with the KC-135 Stratotanker at the Pittsburgh International Airport Warm-up and chamber sampling periods are indicated by vertical grey bars. | 9 |
| Figure 2. Time series of engine operating conditions for Wright Patterson experiments. | 11 |
| Figure 3. Picture of experimental set up used for the Pittsburgh tests. | 13 |
| Figure 4. Schematic (upper panel) and picture (lower panel) of the sampling rake used for the tests at the Pittsburgh International Airport. The center inlet of the rake was aligned with the oil vent, which is the cone-shaped piece protruding from the back of the engine. | 14 |
| Figure 5. Inlets probes installed in the exhaust duct immediately downstream of the T63 engine at Wright Patterson Air Force Base. (Photo credit – Wright Patterson Personnel) | 15 |
| Figure 6. Transfer line used for the Wright Patterson test. The T63 engine test cell was located inside the building. The smog chamber and other sampling equipment were located outside. | 15 |
| Figure 7. Schematic of sampling equipment at the end of the heated transfer used for the Pittsburgh Airport Tests. The same sampling configuration was used for the Wright Patterson experiment, except there was no residence time chamber (the filter samples were drawn directly off of the end of the dilution tunnel). The figure is not drawn to scale..... | 16 |
| Figure 8. Picture of the uncovered (exposed to sunlight) smog chamber at the Pittsburgh airport test. In the foreground is the dilution sampler (silver drum). | 17 |
| Figure 9. VOC emissions as function of load measured during the Pittsburgh tests (a) propene, (b) single-ring aromatics (sum of benzene, toluene, xylenes, ethyl benzene, styrene, ethyl toluene, and trimethyl benzenes) and IVOCs. APEX data in (a) are from the NASA multi-gas analyzer and in (b) from PTR-MS measurements [10]. Error bars for the APEX data show one standard deviation. | 30 |
| Figure 10. Total PM, primary organic aerosol (POA), and EC emissions as a function of load measured in the (a) smog chamber and (b) dilution tunnel during the Pittsburgh tests. As described in the text, panel (b) includes two estimates of the POA emissions. QBT = quartz behind Teflon filter, which provides an estimate of the positive sampling artifact. The data for the 4% and 7% loads shown are averages over multiple experiments conducted at those loads. The SMPS and Teflon filter data points are offset for clarity. | 32 |
| Figure 11. Partitioning plot showing the POA emission factor as a function of organic aerosol concentration (C_{OA}) measured while emissions were injected into the smog chamber at 4% load. Also shown is the BC emission factor inside the chamber, | |

which does not change as more exhaust is injected into the chamber. Lines are included to guide the eye. 35

Figure 12. Thermodenuder measurements of fresh primary organic aerosol volatility from the Pittsburgh tests. OA MFR – organic aerosol mass fraction remaining. 36

Figure 13. (a) Chromatograms of m/z 57 signal from quartz filter and Tenax sorbent samples collected at 4% and 7% load; (b) m/z 57 chromatograms of the JP8 fuel and lubricating oil used in these tests; and (c) cumulative distributions of m/z 57 chromatograms of emissions collected at 4%, 7%, 30%, and 85% loads, as well as jet fuel and jet lubricating oil. Volatility (C^* , $\mu\text{g m}^{-3}$) decreases with increasing retention time in the GC. The indicated elution times for IVOCs, SVOCs, and LVOC/ELVOC are based on n -alkanes. 37

Figure 14. Distribution of measured organic emissions at 4% and 85% load. The panels on the left side show the distribution of emissions between VOC, IVOC, SVOC, and LVOC/ELVOC. The panels on the right side show details of the low-volatility emissions, and split the IVOC and SVOC emissions into speciated and UCM fragments. 39

Figure 15. Time series of a) gas and b) particle-phase concentrations measured during a photo-oxidation experiment conducted at 4% engine load. Vertical gray bars indicate period when bag is filled with exhaust or when the aerosol was passed through the thermodenuder. 41

Figure 16. Size distributions measured a) immediately after fill, b) immediately before lights on, c) nucleation event (shortly after lights on), and d) aged aerosol (after 3 hr of oxidation). The data are from a 4% load experiment. The decrease in particle number is due to a combination of coagulation and particle losses to the chamber walls. 42

Figure 17. Changes in wall-loss corrected PM mass caused by photo-oxidation at (a) 4% load, (b) 7% load, (c) 30% load, and (d) 85% load. The top axis indicates time for OH exposure assuming a constant $[\text{OH}]$ concentration of $3 \times 10^6 \text{ molecules cm}^{-3}$. The ratio of secondary-to-primary PM mass is plotted on the right axis. Note different scales on each panel. 43

Figure 18. a) SOA mass measured at the end of the aging phase of the experiment. b) Sum of single-ring aromatic compounds and sum of IVOC emissions. Data are presented as a function of engine load. Single-ring aromatics include benzene, toluene, xylenes, ethyl benzene, styrene, ethyl toluene, and trimethyl benzenes. IVOCs includes speciated compounds and unresolved complex mixture collected on the Tenax sorbent (UCM). 45

Figure 19. a) Average AMS mass spectra of primary and aged OA. b) Time evolution of AMS f_{44} and f_{57} . Data are averages of all experiments conducted at 4% load. Only undenuded (no TD) data are shown. 47

Figure 20. a) Average thermograms for primary OA, aged OA, and AMS fragments m/z 44 and 57 for the aged aerosol. b) Evolution of total OA volatility at $T = 60^\circ\text{C}$ during the photo-oxidation phase of the experiment. Data are from a 4% engine load experiment. Lines are included to help guide the eye. 48

Figure 21. Total PM emissions from Teflon filter weights (black), bare quartz filter EC (gray), bare quartz filter OC (blue), and QBT estimate of bare quartz filter artifact. Samples for JP8, a 50/50 JP8/FT Blend, and neat FT fuel emissions taken at idle load are on the left. Samples for JP8 and neat FT taken at cruise load are on the right. 50

Figure 22. Select ion chromatogram of m/z 57 from a bare quartz filter at idle load with JP8 fuel. Several n-alkane retention times are marked with blue points and vertical, gray dashed lines. The engine oil and fuel data are shown on top panel (red and black, respectively). The quartz behind Teflon (QBT) and blank data are shown in bottom panel (red and black lines, respectively). 51

Figure 23. Chromatogram of m/z 57 from a cruise load experiment with JP8 fuel. Several n-alkane retention times are marked with blue points and vertical, gray dashed lines. In top panel, m/z 57 chromatograms for engine oil and fuel are shown. The bottom panel shows data for the quartz behind Teflon filter (QBT, artifact). 52

Figure 24. Cumulative mass spectra for OC from JP8, a 50/50 blend of JP8/FT, and neat FT at idle load. Cumulative mass spectra are also shown for the engine oil (black). The cumulative mass spectra are average over 3 time ranges in their respective gas-chromatograms. The first range is 31-53 min. and includes the full range of elution times for the engine oil (red). The second time range covers a peak at approximately 41 min. (blue), and the third range roughly centered at 50 minutes (orange). The corresponding cumulative mass spectrum for the oil is shown as a dashed, black line for all time ranges. Highly oxidized OC likely does not elute from the capillary column used in the GC. 53

Figure 25. Thermodenuder measurements of fresh primary organic aerosol volatility from the Wright Patterson tests with the T-63 engine. OA MFR – organic aerosol mass fraction remaining. 54

Figure 26. Time-series of evolution of gas- and particle-phase compounds for typical photo-oxidation experiments at idle and cruise loads. Data are shown for idle load (expt #2) and cruise load (expt #4). (a,d) CO_2 , ozone, and chamber temperature, (b,e) Concentrations of toluene and acetaldehyde (note scale is not to zero for left axis), (c,f) SMPS total volume and mass median diameter concentrations. Only undenuded data is shown. Vertical grey bars indicate chamber filling period. 56

Figure 27. Primary and secondary PM mass based on estimates from SMPS volume and EC measurements as described in the text. Uncertainty bars indicate uncertainty in assumptions for wall loss corrected (mainly due to loss of vapors). Secondary PM is shown after 3 hours of oxidation. 59

Figure 28. Secondary aerosol formation for experiments performed at idle load with JP-8, blend of JP-8/FT, and FT fuels plotted as a function of OH exposure. The ranges of estimates shown are based on uncertainty in wall-loss corrections and data for duplicate experiments. 60

Figure 29. Change in aerosol composition as measured by the AMS. Change in mass fraction m/z 44 for (a) idle and (b) cruise loads. Note the difference in vertical scales for the two panels. 62

| | |
|---|----|
| Figure 30. Comparison of volatility distributions measured during Pittsburgh and AAFEX tests: (a) idle and (b) take-off rate thrust. | 65 |
| Figure 31. Estimated OH exposure for the twelve different experiments used for the SOA modeling. The median value represented using the orange cross is what is used in our analysis; green bars indicate standard error of the mean. | 67 |
| Figure 32. Comparison SOA formed to emissions of SOA precursor emissions: POC (SVOC and IVOC) and VOC (SOA and no-SOA forming). | 68 |
| Figure 33. Modeled measured measured OA mass for the Pittsburgh / CFM56 (top row) and Wright Patterson / T63 (bottom row) field campaigns. | 73 |
| Figure 34. NT-SOA yield plotted as a function of COA. For reference, the dashed lines indicate SOA yields for <i>n</i> -dodecane, <i>n</i> -tridecane and <i>n</i> -heptadecane from Presto et al. [39]. | 75 |
| Figure 35. Model measurement comparison of SOA formation for each experiment. NT-SOA is predicted using the Hybrid method using best fits for each experiment. | 77 |
| Figure 36. Same as Figure 35 but using optimized CMU parameterization for NT SOA formation. | 77 |
| Figure 37. NT-SOA yield plotted for different POC precursors as a function of C_{OA} . For reference, we also include SOA yields for <i>n</i> -dodecane, <i>n</i> -tridecane and <i>n</i> -heptadecane (dotted black lines) from Presto et al. [39]. | 79 |
| Figure 38. Model measurement comparison of OA concentrations using (a) JP8 ground idle parameterization and (b) JP8 non-idle parameterization. The top row shows data from the Pittsburgh experiments; the bottom row shows data for the Wright Patterson experiments. | 81 |
| Figure 39. Variation in primary organic aerosol emissions (units of color bar -- mg kg-fuel ⁻¹) from the T63 across atmospheric conditions (temperature and organic aerosol concentration). The emission factors are calculated using the volatility distribution of POC emissions listed in Table 13, equilibrium partitioning theory (equation 7), and the enthalpy of vaporization values in Ranjan et al. [42]. | 85 |

List of Acronyms

AAFEX – Alternative Aviation Fuel Experiment
AMS – Aerodyne Aerosol Mass Spectrometer
ASTM -- American Society for Testing and Materials
BC – black carbon
C* -- effective saturation concentration
CMAQ – Community multiscale air quality model
CMU – Carnegie Mellon University
C_{OA} – organic aerosol concentration
CPC - condensation particle counter
DAOF - Dryden Aircraft Operations Facility
EC – elemental carbon
EF – emission factor
ELVOC—extremely low volatility organic compounds
ER – enhancement ratio
FT – Fischer Tropsch fuel
GC – gas chromatograph
GEOS-CHEM -- Goddard Earth Observing System with Chemistry
GI – ground idle
ICAO -- International Civil Aviation Organization
IVOC -- intermediate volatility organic compounds
LTO – landing takeoff
LVOC – low volatility organic compounds
MFR – mass fraction remaining
MMD – mass median diameter
MS – mass spectrometer
MSD – mass selective detector
NAAQS -- National Ambient Air Quality Standards
NASA -- National Aeronautics and Space Administration
NRP - normal rated power
NT-SOA – non-traditional secondary organic aerosol
OA – organic aerosol

OC – organic carbon
OD – outside diameter
OM/OC - organic-mass-to-organic-carbon ratio
PAH – polycyclic aromatic hydrocarbon
PIT – Pittsburgh experiment
PM – particulate matter
PM_{2.5} -- particulate matter with an aerodynamic diameter less than 2.5 µm
PMCAMx – research version of Comprehensive Air quality Model with extensions
POA -- primary organic aerosol
POC – primary organic carbon
POG – primary organic gases
ppmw – parts per million by weight
ppbv – parts per billion by volume
Q – quartz filter
QBT – quartz behind Teflon filter
RH – relative humidity
SERDP - Strategic Environmental Research and Development Program
SIM – selective ion mode
SMPS -- scanning mobility particle sizer
SOA -- secondary organic aerosol
SVOC -- semivolatile organic compounds
TD – thermal desorption
TD - thermodesorber
T-SOA – traditional SOA
UCM – unresolved complex mixture
US EPA – United States Environmental Protection Agency
UV – ultraviolet
VBS – volatility basis set
VOC – volatile organic compound
WPAT – Wright Patterson Air Force Base

Keywords

aircraft; emissions; air pollution; fine particulate matter; PM_{2.5}; atmospheric chemistry; secondary organic aerosol

Acknowledgements

Funding was provided by the U.S. Department of Defense Strategic Environmental Research and Development Program (SERDP) under project WP-1626. The views, opinions, and/or findings contained in this report are those of the authors and should not be construed as an official position of any funding agency.

Bruce Anderson from NASA and Scott Herndon from Aerodyne Research Inc. provided critical assistance early in the project on sampling aircraft emissions, including inviting the Carnegie Mellon University team to participate in AAFEX testing. This was essential for developing the expertise required to conduct the two major field campaigns.

Richard C. Miake-Lye from Aerodyne Research Inc. organized the SERDP volatile PM working group meetings, which fostered productive interactions between the different projects. Richard Miake-Lye and Scott Herndon of Aerodyne also both generously shared their expertise on aircraft emissions through many conversations.

We thank Pennsylvania Air National Guard 171st Air Refueling Wing for hosting the CFM56 tests at the Pittsburgh International Airport. Many individuals from the 171st contributed to the project, but we owe special thanks to those from the Maintenance Group and Civil Engineering. Key contributors included James Weber, Rich Kelly, and Karen Knoerdel. Pat Gallagher and his team provided invaluable support in running the emissions tests. Jeff Andrulonis also was very helpful and a cheerful escort for much of the project. Jeff Janetski and others helped us with the electronic engine test data. There were many others who contributed in many different ways including: Ray Biddle, Justin Blinkey, Cliff Rumbaugh, Randy Reese, Kite Miller, Rickey Perza, Jeff Moyer, Kris Civils, Phillip Liberto, Greg Haney, Ron Shinsky, Michael Turk, Brian Schaub, and Mark Volchko.

We thank Edwin Corporan and his team at Wright Patterson Air Force Base for hosting the T63 tests. Key contributors included Chris Klingshirn, David Anneken, Matt DeWitt and Joe Mantz from University of Dayton Research Institute and Matt Wagner, and Dean Brigalli from the Air Force Research Laboratory.

Daniel D. Riemer at the University of Miami provided and analyzed VOC canisters for the Pittsburgh and Wright Patterson tests.

Finally, this project would not have been possible without the dedication and hard work of a large team of researchers in the Center for Atmospheric Particle Studies at Carnegie Mellon University. Dr. Albert Presto (the Center for Atmospheric Particle Studies research manager) led the field campaigns and directed much of the research. Prof. Peter Adams and Prof. Neil Donahue provided critical guidance on modeling, data analysis, and modeling. Dr. Eric Lipsky (on the faculty at Penn State Greater Allegheny) was instrumental in helping to design and deploy the sampling system. The bulk of the research was performed by graduate students, former graduate students, and postdoctoral associates. Dr. Marissa Miracolo analyzed the photo-chemical aging experiments. Shantanu Jathar developed the secondary organic aerosol model. Dr. Manish Ranjan and Aaron Reeder did the majority of the work constructing the sampling system. Dr.

Greg Drozd performed the primary characterization for the Wright Patterson experiments. Others who contributed to the work include Dr. Chris Hennigan, Ngoc Nguyen and Timothy Gordon.

Abstract

Objectives: Many Department of Defense facilities are located in areas designated as nonattainment with respect to the federal fine particulate matter standard, but the impact of emissions from these facilities on local and regional air pollution levels is not well understood. The goal of this project was to gain new fundamental understanding of volatile particulate matter emissions from military aircraft. Specific objectives included: (i) measuring the amount, chemical composition, and other properties of particulate matter in emissions from military aircraft, (ii) quantifying the effects of atmospheric aging on volatile particulate matter emissions, (iii) characterizing the effects of alternative fuels on particulate matter emissions, and (iv) developing a theoretical model to predict the evolution of aircraft particulate matter emissions from the engine exit plane to highly dilute background as a function of photochemical age.

Technical Approach: Experiments were performed to characterize the atmospheric evolution of volatile particulate matter emissions from military aircraft engines including CFM56-family and T63 gas-turbine engines. The experiments featured a suite of state-of-the-art instrumentation to comprehensively characterize the gas- and particle-phase emissions. Novel aspects of the experiments included quantification of the volatility and gas-particle partitioning of the volatile particulate matter emissions and characterization of the production of secondary particulate matter in a smog chamber. The data were used to develop parameterizations for use in chemical transport models to predict the contribution of aircraft to ambient fine particulate matter.

Results: The project obtained significant data on gas- and particle-phase emissions from two CFM56 engines and one T63 engine. The composition of the primary particulate matter mass emissions from the CFM56 and T63 engines varied with engine load. For both engines, the particulate matter emissions at low load are dominated by organics (volatile particulate matter) and by elemental carbon (non-volatile particulate matter) at high load. Operating the T63 on Fischer-Tropsch fuel substantially reduced the primary particulate matter emissions.

A significant fraction of the particulate matter emissions is semivolatile at atmospheric conditions. For example, modest heating caused a large fraction of the primary organic aerosol to evaporate. Therefore, a traditional emissions factor cannot be used to represent military aircraft particulate matter emissions in inventories and models. Instead, one must measure the total emissions rate of semivolatile species and the volatility distribution of the emissions.

The smog chamber experiments demonstrated that photo-oxidation creates substantial secondary particulate matter, greatly exceeding (by as much as a factor of 60) the direct particulate emissions after an hour or less of aging at typical summertime conditions. This was observed in every smog chamber experiment except one using exhaust from the T63 engine operating at cruise load on neat Fischer-Tropsch fuel. Therefore secondary particulate matter production must be accounted for in order to assess the contribution of military aircraft emissions to urban and regional air pollution.

Benefits: The modules developed by this project will lead to more robust assessment of the impacts of both military and civilian aircraft on urban and regional air pollution.

Objectives

This project developed experimental data, modeling tools, and fundamental knowledge needed for the Department of Defense to accurately and cost effectively assess the impact of volatile PM emissions from military aircraft on local and regional air quality. Volatile PM is formed from inorganic and organic condensable gases which undergo gas-to-particle conversion when the combustion products are rapidly cooled after leaving the engine [1]. This project was in response to SERDP SON number WPSON-08-05 that identified knowledge gaps in our understanding volatile PM emissions from military aircraft.

The research was designed to investigate two hypotheses. The first is that the concentration of volatile PM concentrations depends on gas-particle partitioning of compounds that are semivolatile at atmospheric conditions. If true, this hypothesis has important implications for how we measure and simulate volatile PM emissions from aircraft. Partitioning depends on the temperature and composition of the plume; therefore this hypothesis implies that the amount of volatile PM changes with changing atmospheric conditions. To account for this dynamic character one must measure the total emissions rate of semivolatile species and then predict the fraction of these emissions that exist in the particle phase. The second hypothesis is that photo-oxidation in the exhaust plume will create significant volatile PM, greatly exceeding the non-volatile emissions or the volatile particles that form in the plume shortly after leaving the engine. If true, then aging must be accounted for in order to assess the contribution of military aircraft emissions to urban fine particle levels.

Specific technical objectives included:

1. Measure the chemical composition and properties of volatile PM in emissions from military aircraft as a function of dilution and photochemical age,
2. Quantify the effects of dilution, temperature, and photochemical age on gas-particle partitioning of volatile emissions from military aircraft, and
3. Develop a theoretical model to predict the volatile PM emissions across the entire range of atmospheric conditions from the engine exit plane to highly dilute background as a function of photochemical age.

Background

In 1997 the US EPA revised the National Ambient Air Quality Standards (NAAQS) to regulate concentrations of $\text{PM}_{2.5}$ mass (particulate matter mass with an aerodynamic diameter less than $2.5\ \mu\text{m}$). In 2006, the $\text{PM}_{2.5}$ NAAQS was tightened to account for improved knowledge of health impacts of $\text{PM}_{2.5}$ exposures. Many Department of Defense facilities are located in areas designated as nonattainment with respect to the $\text{PM}_{2.5}$ NAAQS, but the impact of emissions from these facilities on local and regional $\text{PM}_{2.5}$ concentrations is not well understood.

Aircraft directly emit particles, but the vast majority of the emissions are gases and vapors, some of which undergo gas-to-particle conversion in the atmosphere. Primary particulate matter (PM) is comprised of directly emitted particles plus any material that condenses into the particle phase without undergoing chemical reactions [2]. Secondary PM is formed from oxidation of gas-phase species such as SO_2 and organics [2]. To develop effective control strategies one must understand the overall contribution of military aircraft emissions to ambient $\text{PM}_{2.5}$ -- both direct particle emissions and $\text{PM}_{2.5}$ formed in the atmosphere.

Numerous studies have characterized primary PM emissions from aircraft [3-11]. Aircraft emit a mixture of so called non-volatile and volatile PM. Non-volatile PM is refractory material such as elemental carbon that exists in the particulate phase at the high temperatures at the engine exit plane. Volatile PM is formed from species that exist as condensable gases (e.g. sulfuric acid/ SO_3 and organics) in the hot exhaust; as the exhaust mixes with ambient air these gases are cooled, causing them to condense onto existing particles or to form new particles. It is called “volatile” PM because it is comprised of material that exists as vapors at the engine exit plane. However, the gas-particle partitioning of the volatile PM evolves in the atmosphere making it difficult to measure and even define [2]. For example, the size, composition and mass of primary organic PM emissions evolve significantly within tens of meters of leaving an aircraft engine [6]. The amount of volatile PM emissions is also very sensitive to sampling conditions [10, 12-14]. Consequently, the contribution of volatile PM emissions from aircraft to ambient $\text{PM}_{2.5}$ levels is not well understood.

A major focus of past volatile PM research has been on the particle size distribution, especially on the total particle number and formation of new particles [15-18]. Less research has focused on the overall contribution of volatile PM to the overall particle mass. In the context of the $\text{PM}_{2.5}$ NAAQS, we are interested in the total mass of volatile PM, not details of the size distribution (only that the PM smaller than $2.5\ \mu\text{m}$).

Many studies have investigated the important role that sulfur species play in the formation of volatile PM in aircraft exhaust. A key parameter is the fraction of the fuel sulfur that is emitted as SO_3 because essentially all of the SO_3 rapidly forms non-volatile sulfate as the exhaust is cooled. Although SO_3 is thermodynamically favored as the exhaust cools [19], kinetic limitations slow the oxidation of SO_2 to SO_3 . Typically only

1-10% of the fuel sulfur is emitted as SO_3 , which is rapidly converted to volatile PM in the plume. A few studies have directly measured exit plane SO_3 or plume sulfate concentrations, but many researchers have inferred concentrations based on analysis of measured particle size distributions. For engines operating on high sulfur fuel, the measured particle size distributions can be explained with plausible levels of fuel sulfur conversion [8, 20]. However, data measured downstream of engines operating on low-sulfur fuel clearly indicate that non-sulfur species, typically attributed to non-methane hydrocarbons, also contribute significantly to volatile PM [20-22].

Aircraft engines also emit significant amounts of non-methane hydrocarbons [23-26]; however relatively little is known about the contribution of organics to volatile PM emissions. Like all combustion systems [27-29], the overall mass emissions of non-methane hydrocarbons are dominated by low molecular weight species, such as propene, formaldehyde, and acetylene formed from cracking of fuel molecules [23, 24, 30, 31]. These species are much too volatile to partition into the particle phase and therefore do not contribute to volatile PM.

The least volatile fraction of the organic emissions condenses in the atmosphere to form primary organic aerosol (POA) [2]. Recent research has demonstrated that a large fraction of the POA emissions from diesel engines and biomass combustion are semivolatile (species that exist in both the gas and condensed phases) in the atmosphere [2, 32, 33]. The gas-particle partitioning of semivolatile species and therefore the amount of POA (and primary PM) will vary with changing atmospheric conditions (temperature and pollutant concentrations) [2, 32, 34]. This greatly complicates the measurement and even definition of the volatile PM emissions. However, it is not known if aircraft POA emissions are semivolatile. If they are, then the volatility distribution of the organic emissions must be known to predict how the gas-particle partitioning of POA evolves in the atmosphere.

Another important issue is the effect of photochemical aging on the volatile PM emissions. This aging begins immediately after the exhaust has exited the aircraft, initially by radicals such as OH present in the exhaust [35] and subsequently by photolysis and radicals produced in the plume [36]. Photo-oxidation creates additional condensable gases such as SO_3 (which rapidly converts to H_2SO_4) and lower volatility organics that add volatile PM mass. Therefore, knowledge of the condensable species concentrations at the engine exit plane is, by itself, insufficient to determine the ultimate contribution of the emissions to volatile PM.

Defining the ultimate amount of volatile PM produced from sulfur emissions is relatively straightforward. In the atmosphere, SO_2 emissions are oxidized to sulfate; it is simply a matter of the oxidation rate. Therefore, one simply needs to know the fuel-sulfur content to define the maximum possible sulfate emissions. Chemical transport models typically predict that about one-half of SO_2 emissions are ultimately oxidized to sulfate in the atmosphere, with the other half depositing directly to the surface. However, defining the potential contribution of other components (NO_x , organics) in the exhaust is more complex. For example, the majority of NO_x exists as NO in the plume, but is gradually converted to NO_2 as the plume mixes with background air containing ozone. NO oxidizes to HNO_2 while NO_2 oxidizes to HNO_3 . HNO_3 and HNO_2 may contribute to

volatile PM, but their contribution is currently not well understood. Under the relatively warm conditions of the lower troposphere relevant to the PM_{2.5} NAAQS, HNO₃ condenses into the aerosol phase when there is free ammonia (or another cation) available to neutralize it [36]. Therefore, we expect that nitrate aerosol formation from aircraft emissions will depend critically on the availability of free ammonia in background air as the plume dilutes. Temperature will also be a critical parameter, with greater nitrate expected during winter.

Even less is known about the fate of the complex mixture of organics in the plume. Aircraft emit organic gases and vapors, such as toluene and benzene, which are known precursors for secondary organic aerosol (SOA; organic aerosol that forms in the atmosphere from gas-phase reactions). Although many studies have characterized emissions of organic gases [4, 10, 23-26, 37], relatively little is known about the emissions of lower volatility organic vapors from aircraft. These vapors are thought to be important SOA precursors [38-40]. Low volatility vapors with effective saturation concentrations (C*) between 10³ and 10⁶ µg m⁻³ are classified as intermediate volatility organic compounds (IVOCs) and emissions with C* values between 10⁻¹ and 10² µg m⁻³ are semivolatile organic compounds (SVOCs) [41]. Spicer et al. [24] identified several C₁₃-C₁₇ branched and straight-chain hydrocarbons and naphthalenes in the IVOC volatility range. Agrawal et al. [3] quantified *n*-alkanes over a wide volatility range (10⁻¹ < C* < 10⁶) as well as polycyclic aromatic hydrocarbons (PAHs) that are IVOCs and SVOCs. However, comprehensive characterization of emissions from other combustion sources indicates that the vast majority of the IVOC and SVOC mass cannot be speciated [27]. Therefore, the available data (which are for a very limited number of compounds) probably vastly underestimate the aircraft emissions of low volatility organic vapors.

Materials and Methods

Experiments were performed to characterize the volatile PM emissions from military aircraft. Data from two major field campaigns were analyzed to quantify the volatility and gas-particle partitioning of the PM emissions and the production of secondary PM in a smog chamber. These data were used to develop parameterizations that can be used in chemical transport models to predicting the contribution of aircraft to ambient fine PM. This section describes the experimental, data analysis, and modeling methods used by this project.

Field Campaigns

Two major field campaigns were conducted during this project. In July 2009, the emissions from a CFM56-2B1 gas-turbine engine mounted on a KC-135 Stratotanker airframe were characterized at the Pittsburgh International Airport in collaboration with the Pennsylvania Air National Guard 171st Air Refueling Wing. In September 2010, the emissions from a T63 turboshaft engine mounted in a test cell were characterized in collaboration with the Fuels and Energy Branch at Wright-Patterson Air Force Base. There are nearly twenty thousand CFM56 family engines currently in use, powering military aircraft, the Boeing 737, and several Airbus models (www.cfm56.com). The T63 is an older engine that is mainly used in helicopter applications. Essentially the same experimental set-up and instrument package was used for the two major field campaigns.

In addition to these two major, Carnegie Mellon University led field campaigns; the project team also participated in two additional field campaigns led by other organizations. During these campaigns we only collected filter and sorbent samples to characterize the low volatility organic emissions. These initial campaigns were used by the project team to gain experience with aircraft sampling before conducting the major field campaigns, to test sampling and analysis methodologies for low volatility organics, and to expand the ultimate project database. The first field campaign was the NASA Alternative Aviation Fuel Experiment (AAFEX) that was conducted at the Palmdale, CA aircraft facility in January-February, 2009. This campaign characterized the emissions of a CFM56-2C engine mounted on the NASA DC-8. The second minor field campaign was conducted at Chicago Midway airport during March of 2009 led by Aerodyne Research Inc. During this campaign we sampled low load emissions approximately 100 m downstream from CFM56 engines mounted on Southwest airlines planes. This sampling strategy did not collect enough analyte for GC-MS analysis and therefore the results from Midway campaign are not discussed in this report.

We also performed experiments in the Carnegie Mellon University laboratories including tests with small diesel generator to develop and test emissions sampling methodologies and experiments conducted in a smog chamber to investigate the secondary organic aerosol production from different evaporated aviation fuels. The results from the laboratory work are described in the peer-reviewed archival literature [42].

Pittsburgh Tests

During the Pittsburgh campaign separate tests were performed at different loads while the KC-135 Stratotanker was parked and chocked. Table 1 lists the different test conditions. Each test point was set based on fan speed (N1) to correspond to different engine thrust settings, including those prescribed by the International Civil Aviation Organization (ICAO) LTO cycle. Tests were also conducted at 4% rated thrust (“ground idle”), which is lower than the ICAO idle load setting of 7%. Engine operation at 4% load may be more representative of ground operations at airports than 7% load, and PM and hydrocarbon emissions are both higher and more variable at loads less than 7% [10, 26]. The aircraft was operated on standard JP8 fuel. Fuel composition data are shown in Table 2.

After start up, the engine was run for approximately five minutes at low load (4%), allowing time for warm-up, before the test point was set. Sampling began several minutes after the test point was set. Time-series of fan speed and exhaust gas temperature for each engine run is shown in Figure 1. The engine exhaust gas temperature was stable throughout the experiment. In high load experiments, the engine oil temperature slowly increased throughout the sampling period.

Table 1. Summary of tests conducted with the KC-135 Stratotanker at the Pittsburgh International Airport.

| Date | Thrust Setting | Fan speed (N1) | Fuel Flow (kg sec ⁻¹) |
|-------------|----------------|----------------|-----------------------------------|
| 16-Jul-2009 | 7% | 24.5 | 0.10 |
| 17-Jul-2009 | 30% | 53.7 | 0.29 |
| 20-Jul-2009 | 4% | 19.2 | 0.09 |
| 21-Jul-2009 | 4% | 19.0 | 0.08 |
| 22-Jul-2009 | 85% | 82.2 | 0.76 |
| 23-Jul-2009 | 7% | 25.1 | 0.10 |
| 24-Jul-2009 | 4% | 19.7 | 0.09 |

Table 2. Fuel properties of JP8 used for the KC-135 tests at the Pittsburgh International Airport.

| Parameter | Unit | Value | ASTM method |
|--------------|--------|-------|-------------|
| Hydrogen | Wt. % | 14.0 | D3701 |
| Aromatics | Vol. % | 14.1 | D1319 |
| Olefins | Vol. % | 1.4 | D1319 |
| Saturates | Vol. % | 84.5 | D1319 |
| Naphthalenes | Vol. % | 1.26 | D1840 |
| Sulfur | ppmw | 608 | D5453 |

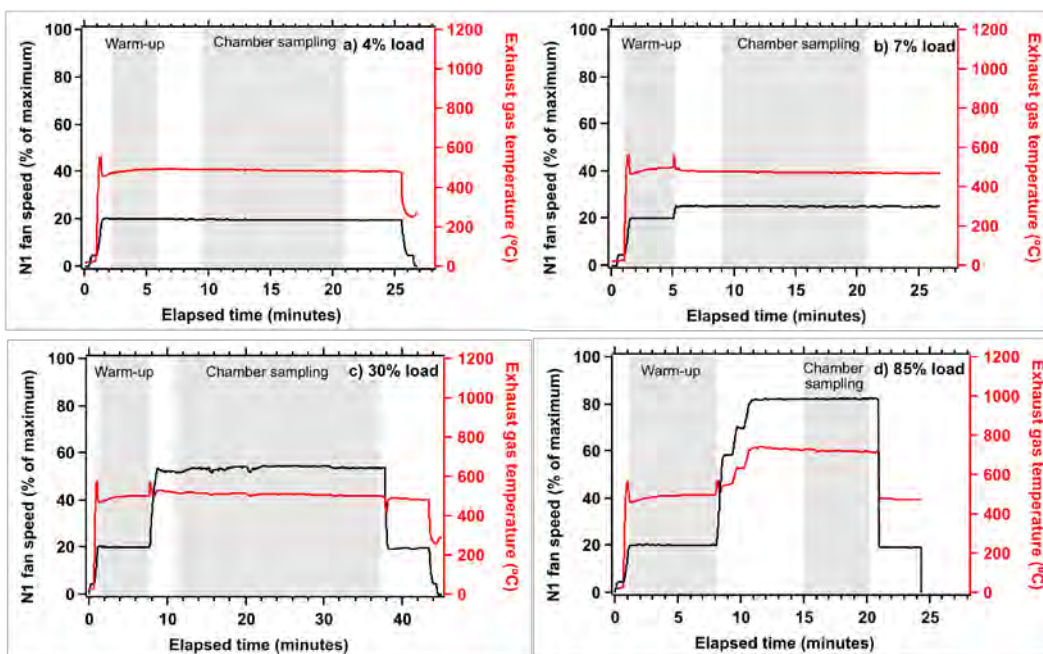


Figure 1. Time-series of N1 fan speed (% of maximum) and exhaust gas temperature for experiments conducted (a) 4% load, (b) 7% (c) 30% and (d) 85% engine loads for the experiments conducted with the KC-135 Stratotanker at the Pittsburgh International Airport. Warm-up and chamber sampling periods are indicated by vertical grey bars.

Wright Patterson Tests

The experiments at Wright Patterson were performed using a T63 turboshaft engine operated on a test cell. A list of experiments is provided in Table 3. Experiments were performed at two engine load conditions – Ground Idle (GI) and Normal Rated Power (NRP, also referred to as cruise). The idle engine condition was set with no load on the dynamometer and fixed fuel flow of $0.006 \text{ kg sec}^{-1}$. For the cruise engine condition, the engine was operated at a constant shaft speed of 6000 rpm and a constant turbine outlet temperature of $693 \text{ }^{\circ}\text{C}$ [43]. Sampling was initiated after warming up the engine for approximately 5 minutes. Time series of engine conditions for the Wright Patterson tests are shown in the Figure 2 for both idle and cruise loads.

Separate experiments were performed while operating the T63 on three different fuels: standard petroleum-based aviation fuel (JP-8), a synthetic fuel produced by the Fischer-Tropsch (FT) process derived from a coal feedstock, and a 50/50% volume blend of the two fuels. Fuel properties are listed in Table 4 for the neat JP-8 and FT fuels. Major differences between the fuels include aromatic and sulfur content. The sulfur content of the JP-8 fuel is 0.064% (640 ppmw), while the sulfur content of the FT fuel is below the detection limit of the test ($<0.001\%$). The total aromatic content of the JP-8 is 17.2% vol, while the aromatic content of the FT fuel is 0.4% vol. Total hydrocarbon

analysis shows higher concentration of normal and branched compounds in the FT fuel, while the JP-8 fuel contains more cyclic compounds. The data shown in Table 4 are similar to data for other JP-8 and FT samples [9, 44, 45].

Table 3. Summary of experiments conducted with the T63 engine at Wright Patterson Air Force Base.

| Fuel | Expt. date | Load |
|-------------|-------------------|-------------|
| JP-8 | 10/8 | Idle |
| JP-8 | 10/5 | Cruise |
| JP-8 | 10/12 | Cruise |
| Blend | 10/14 | Idle |
| FT | 10/6 | Idle |
| FT | 10/13 | Idle |
| FT | 10/7 | Cruise |

Table 4. Select properties for JP-8 and FT fuels used in the Wright Patterson Tests.

| Fuel property | JP-8 fuel | FT fuel |
|------------------------------------|------------------|----------------|
| Hydrogen content, % mass (D3343) | 13.9 | 15.1 |
| Aromatics, % vol (D1319) | 17.2 | 0.4 |
| Total sulfur, % wt (D4294) | 0.064 | < 0.001 |
| Total hydrocarbon type D2425) vol% | | |
| Paraffins (normal + iso) | 50 | 88 |
| Cycloparaffins | 31 | 12 |
| Alkylbenzenes | 12 | 0.4 |
| Indans and Tetralins | 5 | <0.4 |
| Indenes and C_nH_{2n-10} | 0.6 | <0.4 |
| Naphthalene | 1 | <0.4 |
| Naphthalenes | <0.4 | <0.4 |
| Acenaphthenes | <0.4 | <0.4 |
| Acenaphthylenes | <0.4 | <0.4 |
| Tricyclic aromatics | <0.4 | <0.4 |

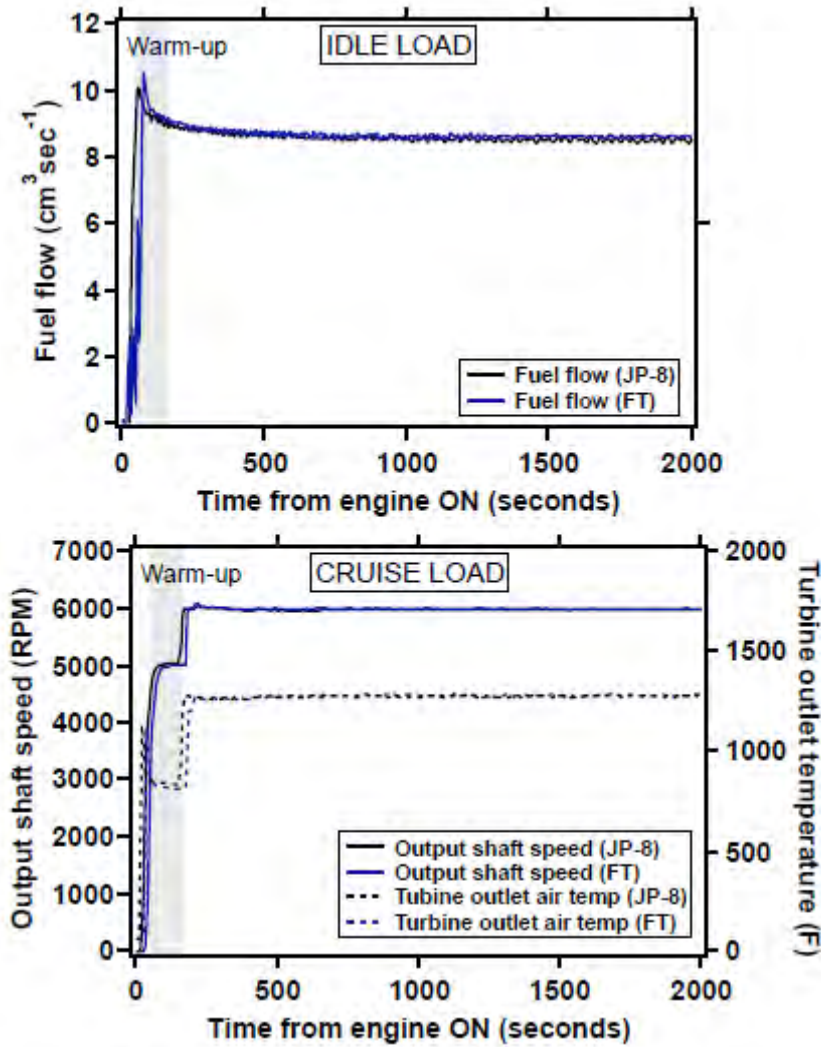


Figure 2. Time series of engine operating conditions for Wright Patterson experiments.

Alternative Aviation Fuel Experiment (AAFEX) Tests

AAFEX was a large test campaign organized by NASA that used the Dryden Flight Research Center DC-8 to assess effects of alternative aviation fuels on the aircraft's CFM-56 engine performance and emission parameters relative to operation with standard JP-8. AAFEX was conducted at the NASA Dryden's Aircraft Operations Facility (DAOF) in Palmdale, California, from January 19 to February 3, 2009. Details of AAFEX program are described by Anderson et al. [46]. The Carnegie Mellon University team only participated in the first part of AAFEX (and therefore only collected samples during at a subset of the AAFEX tests).

During AAFEX, the DC-8 aircraft was parked in an open-air run-up facility and a large number of research groups made gas and particle emission measurements as a function of engine thrust. The Carnegie Mellon University team sampled from an inlet probe installed one meter downstream of the right inboard engine (#3). Table 5 lists the

samples collected by the Carnegie Mellon University team during AAFEX. AAFEX used a test matrix in which the engines were operated over a range of different loads, remaining at a given load for 5 to 30 minutes [46]. As indicated in Table 5, we collected composited samples at AAFEX -- emissions from multiple loads were collected on the same set of media. This was done in order to collect enough sample mass. The compositing strategy was based on combining samples at similar load (e.g. idle sample

was a blend of 4% and 7% load emissions). FT1 was Fischer-Tropsch (FT) fuel synthesized from natural gas. Fuel composition data are in the AAFEX final report [46].

Table 5. List of samples collected by Carnegie Mellon University during the AAFEX test.

| Date | Load | Fuel |
|-----------|----------|------|
| 1/26/2009 | 4%-7% | JP8 |
| 1/26/2009 | 30%-45% | JP8 |
| 1/26/2009 | 65%-45% | JP8 |
| 1/27/2009 | 30%-45% | JP8 |
| 1/27/2009 | 85%-100% | JP8 |
| 1/27/2009 | 4%-7% | JP8 |
| 1/28/2009 | 4%-7% | JP8 |
| 1/28/2009 | 85%-100% | JP8 |
| 1/28/2009 | 4%-7% | JP8 |
| 1/28/2009 | 4%-7% | FT1 |
| 1/28/2009 | 30%-45% | FT1 |
| 1/28/2009 | 85%-100% | FT1 |
| 1/28/2009 | 4%-7% | FT1 |

Emissions sampling

In this section we describe the emission sampling system used for the two major field campaigns. Sampling is a major challenge for characterizing aircraft PM emissions and an area of active research [14]. A common approach is to sample emissions at 1-m downstream of the engine exit plane, which minimizes dilution with background air. However, near the engine exit plane the emissions are concentrated, hot and at high velocity, which creates significant sampling and instrumentation challenges. In addition, the gas-particle partitioning of volatile PM in the hot, concentrated exhaust is very different than in the cool, dilute ambient atmosphere [2]. Some of these challenges can be overcome, at least partially, by diluting the exhaust after sampling. An alternative approach is to sample emissions further (tens to hundreds of meters) downwind of the aircraft, which allows for some natural dilution. However, to avoid high velocities one must be hundreds of meters downwind of an aircraft where the exhaust is highly dilute, which increases the uncertainties associated with background corrections. For this research, emissions were sampled from either a rake inlet installed 1-m downstream of the engine exit plane (Pittsburgh and AAFEX tests) or directly exhaust system (Wright Patterson tests) to minimize dilution of the exhaust with ambient air.

A picture of the overall experimental set up for the Pittsburgh tests is shown in Figure 3. Emissions were sampled from a rake inlet installed 1-m downstream of the engine exit plane, which had three 3.175-mm inlets, one centered on the oil vent at the engine centerline and the other two 7.6-cm above and below the engine centerline. A schematic and picture of the rake inlet is shown in Figure 4. The flows from the three inlets were joined at the base of the sampling rake and then passed through a 20-m long, 1.27-cm O.D. stainless steel transfer line that was electrically heated to maintain an exhaust temperature of 150°C in accordance with the Society of Automotive Engineers Aerospace Recommended Practice 1256B. The dynamic pressure at the centerline inlet was likely lower than at the two inlets in the core flow, possibly affecting the flow through each inlet. We did not measure the actual flow through each inlet. The total flow through the transfer line was ~20 slpm; the residence time inside the transfer line was slightly more than 1 second.

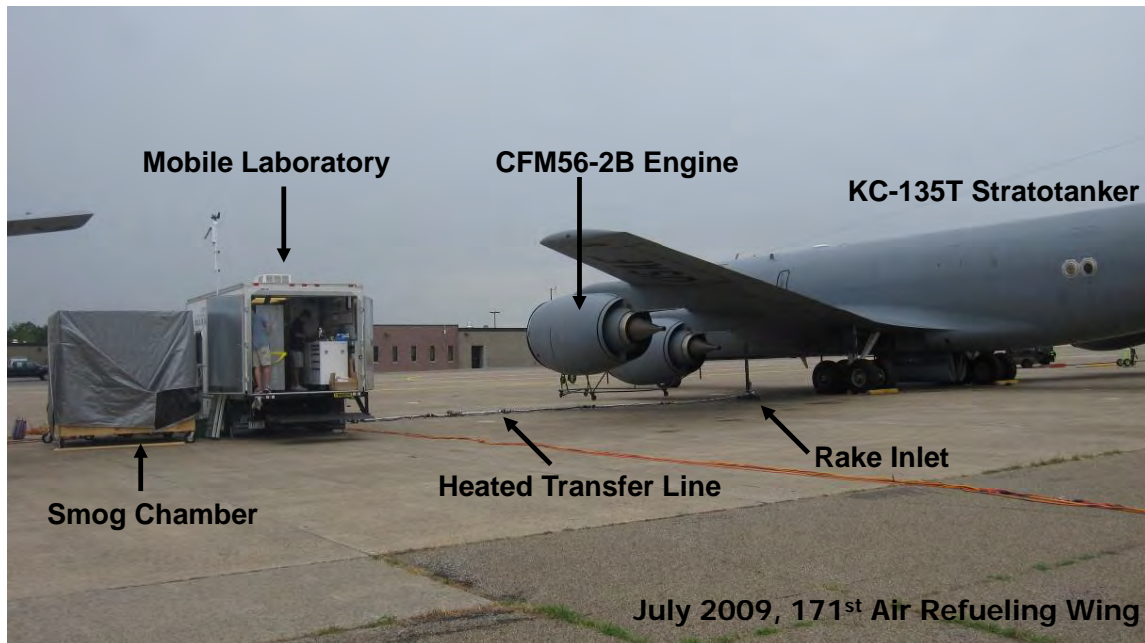


Figure 3. Picture of experimental set up used for the Pittsburgh tests.

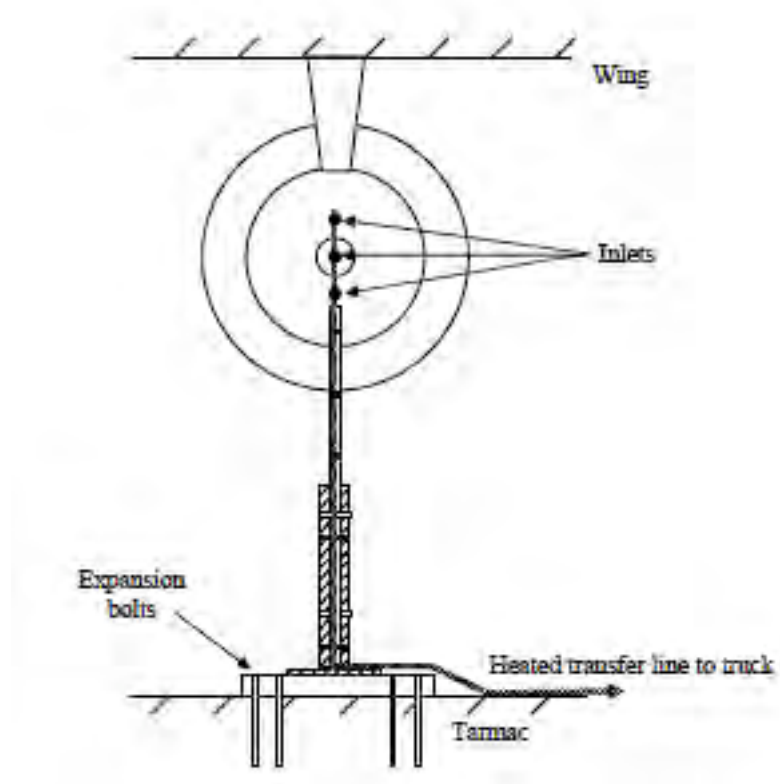


Figure 4. Schematic (upper panel) and picture (lower panel) of the sampling rake used for the tests at the Pittsburgh International Airport. The center inlet of the rake was aligned with the oil vent, which is the cone-shaped piece protruding from the back of the engine.

For the Wright Patterson test, exhaust was sampled using a 0.5 in. stainless steel probe installed in the exhaust system immediately downstream from the engine facing the flow near the exit of the engine (Figure 5). The exhaust was then passed through a roughly 20-m long, 1.27-cm O.D. stainless steel transfer line that was electrically heated to maintain an exhaust temperature of 150°C. A picture of Wright Patterson transfer line is shown in Figure 6.



Figure 5. Inlets probes installed in the exhaust duct immediately downstream of the T63 engine at Wright Patterson Air Force Base. (Photo credit – Wright Patterson Personnel)



Figure 6. Transfer line used for the Wright Patterson test. The T63 engine test cell was located inside the building. The smog chamber and other sampling equipment were located outside.

Figure 7 shows a schematic of the sampling system installed at the end of the heated transfer line. For both the Wright Patterson and Pittsburgh tests, the hot, undiluted

exhaust was divided into three streams at the end of the heated transfer line; two of these streams were rapidly diluted with HEPA- and activated-carbon filtered air to reduce the concentration and temperature of the exhaust to ambient-like conditions. As described below, one stream (~8 slpm) was passed through a dilution sampler that has been extensively used to measure PM emissions from combustion systems [33, 47]. The second stream (~12 slpm) was diluted using a large Teflon smog chamber. The third stream (<1 lpm) was passed undiluted into a five-gas exhaust gas analyzer to measure CO₂, CO, O₂, NO_x, and total hydrocarbons concentrations (Model 7462, Nova Analytical Systems). To minimize thermophoretic and condensation losses, all surfaces in contact with the exhaust up to the point where the exhaust was mixed with dilution air inside either the dilution sampler or the smog chamber were electrically heated to maintain an exhaust temperature of 150° C.

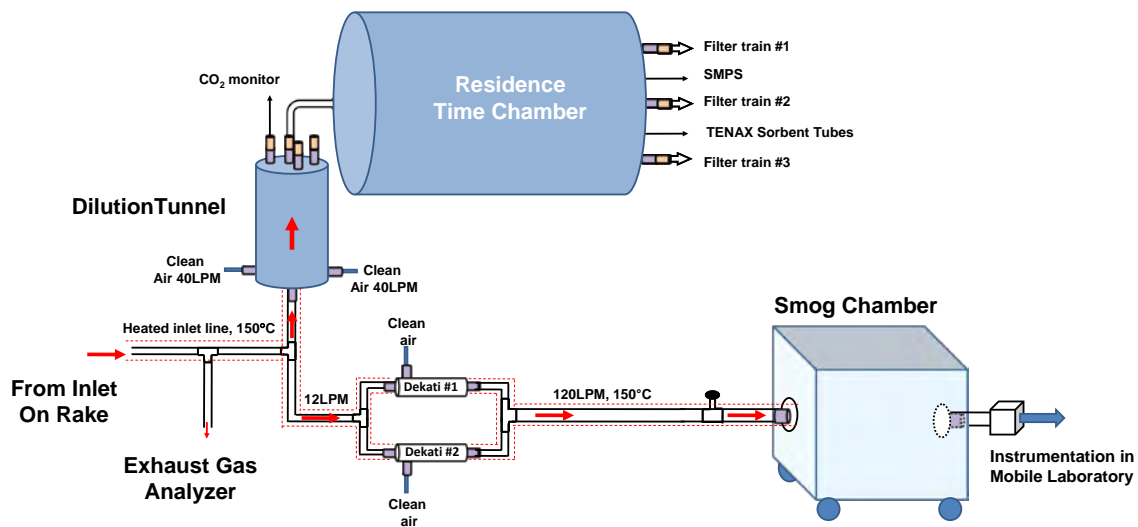


Figure 7. Schematic of sampling equipment at the end of the heated transfer used for the Pittsburgh Airport Tests. The same sampling configuration was used for the Wright Patterson experiment, except there was no residence time chamber (the filter samples were drawn directly off of the end of the dilution tunnel). The figure is not drawn to scale.

The primary PM emissions were characterized using diluted exhaust samples collected from the dilution sampler and the smog chamber. The design and operation of the dilution sampler is described in Lipsky and Robinson [33, 47]. Briefly, the dilution sampler consisted of a mixing or dilution tunnel followed by a residence time tank. Inside the dilution tunnel, a stream of 150°C exhaust is turbulently mixed with dried, HEPA- and activated-carbon-filtered ambient air at a dilution ratio around 10-to-1 (clean air to exhaust), which reduces the temperature of the exhaust to within a few degrees of ambient conditions. For the Pittsburgh experiments the diluted exhaust then passed into a stainless steel tank that provides about 1 minute of residence time to allow condensational processes to occur before collecting samples for analysis [13]. For the Wright Patterson experiments, no residence time chamber was used.

The smog chamber was a 7-m³ Teflon bag (Welch Fluorocarbon) that was initially filled with dried, HEPA- and activated-carbon-filtered ambient air. A picture of the smog chamber is shown in Figure 8. Unlike the dilution sampler, the smog chamber is not a flow through device. Instead exhaust was injected into the closed chamber for ten to thirty minutes using two ejector dilutors (Model DI-1000, Dekati) connected in parallel to the end of the transfer line (Figure 7). Therefore, during injection, pollutant concentrations inside the chamber continuously increased and the dilution ratio of the exhaust inside the chamber decreased. During and after filling, the exhaust inside the chamber was characterized using the suite of instrumentation described below.



Figure 8. Picture of the uncovered (exposed to sunlight) smog chamber at the Pittsburgh airport test. In the foreground is the dilution sampler (silver drum).

Each dilutor used to fill the chamber diluted the exhaust 8-10 to 1 with dried, HEPA- and activated-carbon-filtered ambient air that had been heated to 150° C. The total flow rate of hot diluted exhaust from the two ejector dilutors into the chamber was ~120 slpm. Upon entering the chamber the exhaust was further diluted and rapidly cooled to essentially ambient conditions (the addition of hot exhaust raised the chamber temperature by less than 1° C). The mixing time in a quiescent chamber (with no flow of mixing air or diluted exhaust) was 5-10 minutes; it was shorter when diluted exhaust (or mixing air) was introduced. After filling, the particle concentrations inside the smog chamber ranged from 1 to 50 µg m⁻³ and the dilution ratio of the exhaust ranged from 43 – 127 (mean of 88). This corresponds to plume conditions about 100-m downstream of the engine exit plane [10].

During filling the smog chamber was covered so that the fresh exhaust was not exposed to sunlight in order to prevent photo-oxidization. Between each experiment the smog chamber was cleaned by rapidly flowing conditioned (dried, HEPA- and activated-carbon-filtered) ambient air through the chamber for several hours; a variety of instruments (described below) were used to verify that the chamber was pollutant free (e.g., particle concentration <100 cm⁻³ and CO₂ ~ 400 ppm).

During engine start up HEPA- and activated-carbon-filtered air were back flowed through the transfer line to minimize contamination. Engine operations were then stabilized and flow through the transfer line was reversed with the exhaust flowing out a bypass at the end of the transfer line. Sampling through dilution sampler and into smog chamber was not initiated until after the engine was stabilized at the final test condition.

To minimize contamination all wetted surfaces of the sampling system were stainless steel and carefully cleaned with organic solvents and flushed with high temperature purified (HEPA- and activated-carbon-filtered) air prior to installation at the airport. After assembly at the airport, leak testing was performed to verify that the entire sampling system was leak free. Between every experiment, the entire sampling system was flushed with high temperature purified air.

Separate experiments were conducted to characterize the mass penetration of particles through the sampling system as a function of size at 150°C. The particle transmission efficiency was, on average, 0.94 across a size range of 50-400 nm. All data presented here have been corrected for particles loss as a function of size.

The sampling approach used by this study – dilution after the transfer line – is somewhat different from that used by some recent studies, which diluted the exhaust with dry nitrogen at the probe tip (where the emissions enter the sampling system) [4, 10, 14, 26]. The probe-tip dilution approach tries to preserve the state of PM, such as mass, number, size, and composition in the sampling system [14]. Essentially it tries to preserve the PM as it exists 1 m from the engine exit plane. That is not the goal of our study. Instead, we are investigating the total PM mass in aircraft exhaust after it has been diluted to ambient-like conditions, with a focus on the volatile PM (organics and sulfate). We are investigating PM mass because it is the target of most U.S. and international ambient air quality regulations. Therefore, for our purposes, dilution after the transfer line offers several important advantages over probe tip dilution. First, it greatly simplifies the design and operation of the sampling system. Second, it allows for higher exhaust sample flow rates than standard probe tip dilution systems. Finally, heating the transfer line reduces thermophoretic particle losses and losses of condensable vapors to transfer line walls. In fact, losses of particles and condensable vapors are a greater concern for our work than preserving the exact size distribution. A recent intercomparison of probe tip versus downstream dilution suggests that the downstream approach may have lower losses [14]. Other recent studies have also not used probe tip dilution to characterize aircraft PM emissions [3, 14].

AAEFX sampling

During the AAEFX campaign, sampling was done using a single port on a sampling rake installed 1-m downstream of the right inboard engine (#3). The sample was then passed through a roughly 25-m electrically heated, stainless steel transfer line that was maintained at 150 °C. At the end of the transfer line, four sampling trains were operated on the undiluted exhaust. The tubing immediately upstream of the sampling trains was not electrically heated and therefore some cooling occurred before sample collection.

Two of the sampling trains consisted of a 25-mm quartz filter upstream of a Tenax TA sorbent bed. The other two trains contained a 47-mm bar quartz filter and a 47-mm Teflon filter upstream of a quartz filter, respectively.

Emissions Characterization

During the two major field campaigns, the gas and particle-phase emissions were characterized by drawing samples from the dilution sampler and smog chamber. During the AAFEX experiments, the emissions were characterized using undiluted samples collected on filters and sorbents.

Dilution sampler

Three identical filter trains were connected to the dilution sampler to collect samples for offline analysis (Figure 7). Each train consisted of a sharp cut PM_{2.5} cyclone followed by two lines; one line contained a quartz filter (47 mm, Tissuquartz 2500 QAOUP) and the second line contained a Teflon filter (47 mm, Teflo R2PJ047, Pall-Gelman) followed by a quartz filter. The quartz filter behind the Teflon filter provides an estimate of the sampling artifacts [48, 49]. Tenax TA sorbent samples were also collected downstream of a quartz filter from either the residence time chamber (Pittsburgh tests) or dilution tunnel (Wright Patterson tests). A scanning mobility particle sizer (SMPS, Model 3071a DMA and Model 3025a CPC, TSI) was connected to the residence time tank (Pittsburgh tests) or dilution tunnel (Wright Patterson tests) to measure particle size distributions. The CO₂ concentration of the diluted exhaust was measured at the end of the dilution tunnel (Model LI-820, Li-Cor Biosciences).

The Teflon filters were weighed on a microbalance located inside a temperature and relative humidity controlled chamber before and after sampling. The filters were allowed to equilibrate at 22° C and 35% RH for 24 hours prior to weighing. After weighing, exposed Teflon filters were extracted in deionized water and analyzed by ion chromatography for determination of particulate sulfate [50]. Before sampling the quartz filters were baked in air at 550°C for at least six hours to remove any residual carbon. After sampling, the quartz filters were analyzed with a Sunset Laboratories OC/EC analyzer using the temperature protocol of Subramanian et al [48]. Before sampling, the Tenax sorbent samples were cleaned by thermal desorption in He at 350°C. After sampling, the Tenax sorbent samples and 1.2 cm² punches of the upstream quartz filters were separately analyzed for 60 organic compounds using a Thermal Desorption System (TDS3, Gerstel Inc.) coupled to a gas chromatograph equipped with a mass-selective detector (Agilent 6890 GC and 5975 MSD). Before GC-MS analysis, each sorbent and filter sample was spiked with a deuterated internal standard to track analyte recovery. The internal standard contained five deuterated *n*-alkanes ranging from *n*-hexadecane-d₃₄ (C₁₆D₃₄) to *n*-hexatriacontane-d₇₄ (C₃₆D₇₄). Each analyte was matched to one of the deuterated internal standards based on volatility, e.g. *n*-tetracosane-d₅₀ was used as an internal standard for C₂₃ - C₂₇ *n*-alkanes, to track recovery.

During desorption, the TDS3 was ramped from an initial temperature of 30° C to a final hold temperature of 320° C (5 min) at 100° C min⁻¹. The transfer line connecting the TDS3 to the CIS4 was maintained at 320° C during extraction. The CIS4 used a glass

wool inlet liner and was held at an initial temperature of -120° C during sample transfer. Following transfer, the CIS4 was ballistically heated to a final hold temperature of 320° C (3 min). A 10:1 split ratio was implemented at the CIS4 during transfer to the GC column. The GC method used a column flow of 1.2 mL min⁻¹ and a temperature protocol consisting of: initial hold temperature 60° C (3 min); ramp 5° C min⁻¹ to a final hold at 320° C (6 min). The MSD was operated in combined SIM/scan mode. Multipoint calibration curves for each target analyte were developed using authentic standards. Concentrations of each target analyte were determined using the calibration curves developed and a deuterated internal standard to track analyte recovery.

All of the filter and sorbent sample data were blank corrected. Dynamic blanks were collected before each engine run by placing HEPA and activated carbon filters upstream on the sampler inlet and holding the transfer line at 150°C. Blank corrections for EC on the quartz filters and mass on the Teflon filters were negligible. Dynamic OC blanks from bare quartz filters were approximately 20% of typical bare quartz filter OC. Since negligible PM mass was measured on the Teflon filters collected as part of the dynamic blank, the OC dynamic blank is presumably adsorbed vapor. This hypothesis is supported by the fact that most of the dynamic blank OC evolved in the lowest temperature step of the He-mode of the OC/EC analysis and that the species collected on the Tenax sorbent tubes in the dynamic blanks were IVOCs or more volatile with $C^* \geq 1000 \mu\text{g m}^{-3}$ (roughly species more volatile than a C₂₁ *n*-alkane). The OC dynamic blanks were essentially constant over the course of the study, suggesting that organic material did not build up in the transfer line with each successive engine test.

Smog chamber

A suite of state-of-the-art instrumentation was used to characterize the gas- and particulate-phase pollutants inside the smog chamber. Particle-phase measurements included an SMPS (Model 3080 DMA and Model 3772 CPC, TSI), an Aerodyne quadrupole aerosol mass spectrometer (AMS), a seven-channel Aethalometer (Model AE-31, Magee Scientific), and an *in situ* OC/EC analyzer (Sunset Laboratories). In addition to the real time instrumentation, quartz filter samples and Tenax TA sorbent samples were also collected from the chamber for offline analysis using the previously described techniques.

The AMS quantitatively measures the size and composition of the non-refractory fraction of the aerosol [51, 52]. The AMS data were analyzed using the fragmentation table of Allan et al [53]. The contribution of CO₂(g) at *m/z* 44 was corrected by replacing the default CO₂ concentration used in the fragmentation table (370 ppm) with the measured CO₂ concentration in the chamber. A parallel plate carbon denuder was placed upstream of the OC/EC analyzer to reduce sampling artifacts.

Gas-phase measurements made on the chamber included monitors for CO (Model 300A, API-Teledyne), CO₂ (Model LI-820, Li-Cor Biosciences), SO₂ (Model 100A, API Teledyne), NO_x (Model 200A, API Teledyne), and O₃ (Model 400A, API Teledyne). SUMMA canister samples were collected from the chamber for offline analysis of organic gases via GC-MS at either a commercial laboratory (EMSL Analytical, Inc.) or the University of Miami (Riemer et al., 1994).

AAFEX

The quartz filter, Teflon filter, and Tenax sorbent samples collected at AAFEX were analyzed using the same procedures as those used to analyze the dilution sampler samples.

Photochemical Aging

During the two major field campaigns, the dilute exhaust inside the smog chamber was photochemically aged to investigate secondary aerosol formation. During filling and the primary characterization period immediately after filling, the chamber was covered to prevent exposure to sunlight. Photo-oxidation was initiated by removing the cover to expose the chamber to ambient sunlight. In select experiments banks of UV lights (General Electric, model 10526) were also used to initiate photo-oxidation. The photo-oxidation period of each experiment typically lasted three hours. After the photo-oxidation period, the chamber was covered or the UV lights were turned off and the aged aerosol was characterized in the dark for approximately one hour. Since the portable smog chamber was located outside, it was subject to ambient temperature changes. Prior to photo-oxidation, the average initial chamber temperature was 23 ± 2.5 °C with a relative humidity of 14.7 ± 3.8 % across the set of experiments. The chamber temperature increased, on average, by 4.4 °C during the photo-oxidation phase of the experiments conducted at the Pittsburgh International Airport. The temperatures of the Wright Patterson experiments were somewhat larger, on average, by 11.6 °C during photo-oxidation. This increase in temperature will modestly shift the gas-particle of semivolatile organics towards the vapor phase.

Data Analysis

Fuel-based emission factors

Emissions data measured in both the dilution sampler and smog chamber are reported as fuel-based emission factors (e.g., mg PM_{2.5} kg-fuel⁻¹),

$$EF = \frac{\chi_P}{\chi_{CO_2} + \chi_{CO} + \chi_{HC}} \left(\frac{MW_P}{MW_C} \right) C_f \quad (1)$$

where χ_P is the measured, blank corrected pollutant mixing ratio; χ_{CO_2} , χ_{CO} , and χ_{HC} are the background-corrected CO₂, CO, and unburned hydrocarbon mixing ratios; MW_P/MW_C is the ratio of the molecular weight of the pollutant to carbon; and C_f is the mass fraction of carbon in the fuel (e.g. Table 2).

Secondary Aerosol Production

To estimate secondary PM production, the smog chamber data must be corrected for loss of both particles and semivolatile vapors to the chamber walls. While accounting for the loss of particles to the chamber walls is relatively straightforward, losses of condensable vapors to the chamber walls can introduce significant uncertainty to the wall loss correction [54].

Two independent methods were used to correct chamber data for wall-losses. The first approach follows the method of Weitkamp et al. [55]. A first-order wall-loss rate was estimated from measurements taken during the dark characterization of primary and aged aerosol from the SMPS. Briefly, the change in the suspended particle mass in the chamber (C_{sus}) is given by:

$$\frac{d}{dt}[C_{sus}] = -k_w C_{sus} + \dot{P}_{sus} \quad (2)$$

where k_w is the first-order wall loss rate constant and \dot{P}_{sus} is the production rate of SOA on the suspended particles. The change in mass on the walls of the chamber (C_{wall}) is given by:

$$\frac{d}{dt}[C_{wall}] = k_w C_{sus} + \dot{P}_{wall} \quad (3)$$

where \dot{P}_{wall} is the loss rate of condensable vapors to the walls. The first-order wall loss rate constant was estimated using the measured decay of black carbon (non-reactive) as measured by the Aethalometer and/or the measured decay of primary PM mass before the lights are turned on.

To determine the wall-loss corrected concentration in the chamber, we solve for the production rate of new mass in the chamber, $\dot{P}_{wall} + \dot{P}_{sus}$. \dot{P}_{sus} is calculated by numerically integrating eq. (2) using the time-series of SMPS measurements of suspended mass concentrations. The production rate on the walls is calculated by relating particle mass on the walls to the particle mass in suspension:

$$\dot{P}_{wall} = \dot{P}_{sus} \left(\frac{\omega C_{wall}}{C_{sus}} \right) \quad (4)$$

We consider two limiting cases for calculating production rate to the walls: when the condensable products only partition to the suspended particles ($\omega=0$) and when the material lost to the walls remains completely in equilibrium with the gas phase ($\omega=1$) for the organic mass in the chamber. The sulfate mass in the chamber was corrected using the case of $\omega=0$ while the organic mass in the chamber is corrected using the case of $\omega=0$ and $\omega=1$.

The second method follows that of Grieshop et al. [56], in which black carbon is used as an inert wall-loss tracer. We quantify changes in the OA concentrations in the chamber as an enhancement ratio (ER) defined as:

$$ER = \frac{OA_t / BC_t}{OA_{t0} / BC_{t0}} \quad (5)$$

where OA_t and BC_t are the OA and BC concentrations at a given time t and OA_0 and BC_0 are the OA and BC concentrations at $t=0$. This second approach assumes that the material on the walls remains in equilibrium with the phase composition ($\omega=1$ case).

Thermodenuder data

Aerosol volatility was measured using a thermodenuder (TD) system based on the design of Huffman et al. [57]. The aerosol from the chamber was alternately sampled through the TD or a bypass line maintained at ambient temperature (25 °C) every 15 minutes using the AMS and SMPS. The TD system was operated with two different temperature programs. Prior to photo-oxidation, the primary aerosol was characterized at 40, 60 and 80 °C. During photo-oxidation, the TD was held at 60 °C. After photo-oxidation, the aged aerosol was characterized at 40, 60 and 80 °C. The centerline residence time of the heated section was 18.6 seconds at ambient temperature.

Aerosol volatility is expressed in terms of a mass fraction remaining (MFR). The MFR is defined as the ratio of the AMS organic aerosol concentration measured downstream of the TD to that measured downstream of the bypass line (C_{BP}):

$$MFR = \frac{C_{TD}}{C_{BP}} \quad (6)$$

In this work, MFRs were calculated for both total AMS OA concentrations and individual AMS mass fragments measured, such as m/z 44 and 57. For the temperatures used in this study particles losses in the TD are small (<10%) and no corrections were made for these losses [57, 58].

Modeling

SOA is the fine particle mass arising from the atmospheric oxidation of organic vapors and gases emitted by various natural and anthropogenic sources. The very large number of organic species present in the emissions prevents the development of a bottom-up model to explicitly represent SOA formation. Instead, we seek to parameterize the measured SOA formation using available precursor data.

A limitation of SOA experiments – and smog chamber experiments in general – is that it only captures the evolution of the first few generations of oxidation or about 5-10% of the time spent by these species in the atmosphere. In this work, we focus on the SOA generation from only the first few generations of oxidation. In the atmosphere, however, the first generation products will continue to react and presumably form additional SOA. This multi-generational oxidation remains relatively unconstrained.

Volatility Basis Set

To parameterize the SOA formation, we use the volatility basis set (VBS) framework [59], which separates organics into decadal spaced bins of effective saturation concentration (C^*) between 0.01 to $10^6 \mu\text{g m}^{-3}$. C^* (inverse of the Pankow-type partitioning coefficient, K_p) is proportional to the saturation vapor pressure and is a semi-

empirical property that describes the gas-particle partitioning of an organic mixture [60]. The gas-particle partitioning can be calculated using the following equations:

$$\zeta_i = \left(1 + \frac{C_i^*}{C_{OA}}\right) ; C_{OA} = \sum_{i=1}^N \zeta_i \times M_i|_{g+p} \quad (7)$$

where, ζ_i is the fraction of mass in volatility bin ‘ i ’ in the particulate phase, C_i^* is the effective saturation concentration of bin ‘ i ’ in $\mu\text{g m}^{-3}$, C_{OA} is the total particulate OA concentration in $\mu\text{g m}^{-3}$, $M_i|_{g+p}$ is the total organic concentration (gas+particle) in bin ‘ i ’ in $\mu\text{g m}^{-3}$ and N is the number of basis set bins.

Using the VBS, we can write equations for the conservation of mass for the precursor and SOA mass in the VBS:

$$\frac{d[X_j]}{dt} = -k_{Ox, X_j}[Ox][X_j] \quad (8)$$

$$\frac{d[M_i|_{g+p}]}{dt} = \underbrace{\sum_j \alpha_{i,j} k_{Ox, X_j}[Ox][X_j]}_{\text{first-generation}} + \underbrace{\sum_k \beta_k k_{Ox, M_k}[Ox][M_k|_g]}_{\text{multi-generation}} \quad (9)$$

Equation 8 represents the decay of the fresh precursors where k_{Ox, X_j} is the reaction rate between the oxidant $[Ox]$ and reactant $[X_j]$. The index j indicates the different precursors. Equation 9 represents the evolution of mass in the VBS where $M_i|_{g+p}$ represents the gas-plus-particle-phase mass in the ‘ i ’th C* bin, $[OH]$ is the OH concentration, $\alpha_{i,j}$ represents the mass-yield matrix for all C* bins (‘ i ’) and precursors (‘ j ’) and β_k is the multi-generational aging kernel for the VBS mass. Equation 8 accounts for the formation of new VBS mass from precursor oxidation, which is parameterized using laboratory data. The second term accounts for continuous aging of the products in the VBS. The following sections describe how we use this set of equations to represent SOA formation from different precursors.

VBS Terminology

Organic aerosol has conventionally been classified into primary organic aerosol (POA) and secondary organic aerosol (SOA). POA refers to direct particulate emissions from sources that include combustion of fossil fuels, bio fuels or biomass burning. SOA refers to the particle mass that arises from the condensation of low volatility products formed through the oxidation of gas-phase organic species. Recent research has blurred those conventional definitions. Using the VBS, we define primary organic carbon (POC) as a sum of all the low volatility organic emissions that have a C* lower than $10^6 \mu\text{g m}^{-3}$. We assume that organic emissions with C* higher than $10^6 \mu\text{g m}^{-3}$ are explicitly accounted as VOC species. As some of the POC is semi-volatile, some of it partitions into the gas and particle phases with changes in dilution and temperature. Therefore, we define POA as the particle phase component and POG as the gas phase component of

POC. The aerosol mass arising from the oxidation of POC vapors is defined as non-traditional-SOA (NT-SOA). The particle phase products from the oxidation of VOCs are called traditional SOA (T-SOA).

To simplify discussion of different classes of organics, we shall refer to a number of volatility ranges [41]. Range limits are 3×10^n because volatility bins are centered on powers of 10 (i.e. 0.3–3.0, etc.). In order of increasing volatility, we have:

- Extremely low volatility organic compounds (**ELVOC**, $C^* < 3 \times 10^{-4} \mu\text{g m}^{-3}$). ELVOC are almost entirely in the particle phase under any ambient conditions, but they can evaporate in a thermodenuder.
- Low volatility organic compounds (**LVOC**, $3 \times 10^{-4} < C^* < 0.3 \mu\text{g m}^{-3}$). These are predominantly in the particle phase in the atmosphere.
- Semi-volatile organic compounds (**SVOC**, $0.3 < C^* < 300 \mu\text{g m}^{-3}$). Depending on ambient conditions, these compounds can be in either phase but often have sizable mass fractions in both. Note that this definition of “semi-volatile” includes much lower vapor pressures than those commonly viewed as semi-volatile [61]: SVOCs have vapor pressures ranging from 10^{-5} – 10^{-8} torr. The difference between common perception and this aerosol-specific definition of semi-volatile can be a source of confusion.
- Intermediate volatility organic compounds (**IVOC**, $300 < C^* < 3 \times 10^6 \mu\text{g m}^{-3}$). Myriad compounds of quite low vapor pressure that none-the-less reside almost exclusively in the gas phase under atmospheric conditions [40, 41]. Compounds often described as “semivolatile” in non-atmospheric contexts lie near the high end of the IVOC range.
- Volatile organic compounds (**VOC**, $C^* > 3 \times 10^6 \mu\text{g m}^{-3}$). VOCs are always represented in models either explicitly or as lumped species.

Traditional SOA (T-SOA)

T-SOA is the SOA mass formed through the oxidation of VOC precursors. In this work, we use the equations described earlier, in conjunction with data published in literature, to predict T-SOA formation from VOCs. In equation (8), X_j represents individual VOCs, i.e. benzene, toluene, n-dodecane, cyclohexane etc., and OH is assumed to be the only oxidant. We use the SAPRC 2007 lumping and the mass-yields ($\alpha_{i,j}$) proposed by Murphy and Pandis [62] for all VOCs listed in Table 6. For multi-generational oxidation, we use the recent set of parameters used to model anthropogenic SOA in regional and global models [62-66]. Any gas-phase mass in the VBS is reacted with the OH radical ($k_{OH} = 1 \times 10^{-11} \text{ cm}^3 \text{ molecules}^{-1} \text{ s}^{-1}$) to form a product that is one order of magnitude lower in volatility than the precursor or shifted by one C^* bin relative to the precursor. To account for the addition of oxygen, 7.5% of the precursor’s mass is added to the product. Hence, for T-SOA, β takes the form:

$$\beta = \begin{cases} -1 & \text{if } k=i; \\ +1.075 & \text{if } k=i+1; \\ 0 & \text{otherwise} \end{cases}$$

Table 6. VOC species included in traditional SOA model.

| | | | |
|----------------------------|----------------------------|------------------|---------------------|
| 1-butene | 2-methylpentane | cis-2-pentene | methylcyclohexane |
| 1-heptene | 2,2-dimethylbutane | cis-3-hexene | methylcyclopentane |
| 1-hexene | 2,3-dimethyl-2-pentene | cyclohexane | Naphthalene |
| 1-methylcyclohexene | 2,3-dimethylbutane | cyclohexene | Nonane |
| 1-octene | 2,3,4-trimethylpentane | cyclopentane | o-xylene |
| 1-pentene | 2,4-dimethylpentane | cyclopentene | Octane |
| 1,2-butadiene | 3-ethyltoluene | cyclopropane | p-xylene |
| 1,2-diethylbenzene | 3-methyl-1-butene | decane | Pentane |
| 1,2,3-trimethylbenzene | 3-methylheptane | dodecane | Propane |
| 1,2,4-trimethylbenzene | 3-methylhexane | ethane | Propene |
| 1,2,4,5-tetramethylbenzene | 3-methylpentane | ethene | Propylbenzene |
| 1,3-butadiene | 4-ethyltoluene | ethylbenzene | Propyne |
| 1,3-diethylbenzene | 4-methyl-1-pentene | heptane | sec-butylbenzene |
| 1,3,5-trimethylbenzene | 4-methylheptane | hexane | Styrene |
| 1,4-diethylbenzene | a-pinene | hexylbenzene | Tetradecane |
| 2-ethyltoluene | Acetylene | isobutane | Toluene |
| 2-methyl-1-butene | Benzene | isobutene | trans-1,3-hexadiene |
| 2-methyl-1-pentene | Butane | isopentane | trans-2-butene |
| 2-methyl-2-butene | Butylbenzene | isoprene | trans-2-hexene |
| 2-methyl-2-pentene | c-1,3-dimethylcyclopentane | isopropylbenzene | trans-2-pentene |
| 2-methylheptane | cis-2-butene | limonene/indan | Tridecane |
| 2-methylhexane | cis-2-hexene | m-xylene | Undecane |

Non-traditional SOA (NT-SOA)

NT-SOA is the SOA mass formed through the oxidation of POC vapors. In this section, we present two approaches to parameterize NT-SOA formation of NT-SOA using the VBS and equations (8) and (9).

CMU method

Robinson et al. [40] proposed a novel method to model the formation of NT-SOA. At that time, relatively little was known about the magnitude and composition of POC emissions from different sources. This meant that they could not identify specific POCs and conduct laboratory experiments, similar to those done on VOCs, to determine first generation oxidation products. Instead, they proposed that both the first generation and multi-generational POC oxidation be represented using the multi-generational mechanism, i.e. in the first generation term in equation 9, X_j equals $M_j|_g$ and $\alpha_{i,j}$ equals β . Using gas-particle partitioning data, they were able to distribute POC emissions across the set of C^* s to determine M_k s. Similar to the treatment of multi-generational oxidation for VOCs, any gas-phase mass in the VBS is reacted with the OH radical to form a product that is several orders of magnitude lower in volatility than the precursor. For NT-SOA (CMU), β takes the form:

$$\beta = \begin{cases} -1 & \text{if } k=i; \\ +(1 + f_{oxy}) & \text{if } k=i+q; \\ 0 & \text{otherwise} \end{cases}$$

where, q is the shift in volatility for the product and f_{oxy} is the fraction of oxygen added to the product per reaction.

Previously, Robinson et al. [40] and Shrivastava et al. [61] have used a $k_{OH,M}$ of $4 \times 10^{-11} \text{ cm}^3 \text{ molecules}^{-1} \text{ s}^{-1}$, a f_{oxy} of 0.075 a q of 1 to model NT-SOA formation over the eastern United States; this set of parameters was derived using SOA data for diesel exhaust. Grieshop et al. [56] proposed a $k_{OH,M}$ of $4 \times 10^{-11} \text{ cm}^3 \text{ molecules}^{-1} \text{ s}^{-1}$, a f_{oxy} of 0.40 a q of 2 to model NT-SOA formation based on SOA data for woodsmoke. Dzepina et al. [67, 68] and Hodzic et al. [69] have had some success with these parameterizations to predict the SOA formation over Mexico City. In this work, we determine $k_{OH,M}$, f_{oxy} and q that are able to reproduce the SOA data.

Hybrid method

A potential shortcoming of the CMU method is that it assumes a modest reduction (1-2 C^* bins) in volatility with each oxidation reaction. Kroll and Seinfeld [70] calculated that the oxidation of a volatile hydrocarbon to form a carbonyl, alcohol, nitrate or acid reduced its volatility approximately by 1, 3, 3 or 4 orders of magnitude respectively. In addition, oxidation products of VOCs such as benzene, toluene and xylenes must be 7-8 orders of magnitude lower in volatility than their precursor in order to form SOA [71-73]. Hence, it would be more realistic if each oxidation reaction resulted in a volatility shift that was much more drastic than that proposed by the CMU method.

For NT-SOA, we propose that the first generation of oxidation be treated similar to T-SOA while the multi-generational oxidation is kept the same for all OA. Therefore, this approach provides a consistent and similar treatment of T-SOA and NT-SOA considering that, apart from the volatility of their precursors, they are formed via similar chemical processes.

For the first generation of oxidation, the POC emissions distributed by C^* bin are treated as precursors or as X_j . We assume that the POC emissions only react with the OH radical and that k_{OH} is $4 \times 10^{-11} \text{ cm}^3 \text{ molecules}^{-1} \text{ s}^{-1}$ since it suitably represents the reactivity of species (C_{12+} isoalkanes, C_{10+} cycloalkanes, multi-ring aromatics) found in the POC range [74]. In this method, we determine a mass-yield matrix ($\alpha_{i,j}$) which is able to reproduce the SOA data. Since there are nine VBS precursors ($C^* = 0.01$ to $10^6 \mu\text{g m}^{-3}$) and each precursor's products are fit across 4 VBS bins, there are potentially 36 free parameters. Presto et al. [39] found that for n-alkanes, the addition of 2 carbon atoms to an n-alkane shifted its corresponding SOA product distribution, on average, by one C^* bin or one order of magnitude in C^* space; Lim and Ziemann [75] had hinted at the same trend earlier. Hence, based on the work of Presto et al. [39], we assume that precursor mass in each volatility bin forms the same product distribution but shifted in volatility space by one order of magnitude. For example, if the $C^*=10^3 \mu\text{g m}^{-3}$ surrogate forms a product that has a volatility of $0.1 \mu\text{g m}^{-3}$ with a yield of 20%, the $C^*=10^2 \mu\text{g m}^{-3}$ surrogate will form a product with same yield of 20% but shifted to a volatility of $0.01 \mu\text{g m}^{-3}$. This approach couples the POC precursors together and reduces the fitting procedure to 4 free parameters. For the multi-generational oxidation, we use the same set of parameters used to model the multi-generational oxidation of T-SOA.

O:C ratio

The AMS signal at mass to charge ratio of 44 (m/z 44) can be used to infer the oxygen-to-carbon (O:C) ratio for the OA formed in each experiment [76]. For the PIT-JP8-Idle(1) experiment, the O:C of OA increases from around 0.2 before the formation of SOA to 0.55 after the formation of SOA. Smaller increases were measured during the WPAT-Idle experiments, where the O:C of OA goes from 0.11-0.16 to 0.23-0.35. We did not see any change in O:C during the WPAT-Cruise experiments.

We use the model to calculate an O:C ratio for OA. The O:C of the POA is measured before the oxidation phase of the experiment.. For T-SOA, we use the work of Chhabra et al. [77] to define the O:C for SOA formed from alkenes (α -pinene) and aromatics (m-xylene, toluene, naphthalene) and the work of Presto et al. [39] to define the O:C for SOA formed from alkanes (n-pentadecane).

Model Implementation

The SOA data collected from smog chamber experiments are analyzed using a box model that is composed of two modules: a T-SOA module and a NT-SOA module. The T-SOA module processes VOC and oxidant information to predict the amount of T-SOA that is formed. In the NT-SOA module, the amount of NT-SOA formed is first estimated by subtracting off the predicted T-SOA from the measured SOA. Then, parameters for each NT-SOA method are determined that reproduce the SOA formed in each experiment. Next, the parameters are used to (1) compare how well each method does in reproducing the SOA in each experiment, (2) gain insight into the chemical pathways that define NT-SOA formation and (3) predict the formation of SOA on longer timescales beyond the smog chamber. Each smog chamber experiment is modeled separately.

Results and Discussion

Pittsburgh Tests

Primary emissions of criteria and organic gases

Table 7 lists emission factors for NO, NO_x, CO, and SO₂ measured during the Pittsburgh tests. The SO₂ emission factor was approximately constant (1.2 ± 0.1 g kg-fuel⁻¹), consistent with the fuel-S data listed in Table 2. CO emissions are highest at low load and fall with increasing load, while NO_x emissions are smallest at low load and increase with load. The NO/NO_x ratio increases from 0.2-0.3 at 4% load to 1.0 at 30% and 85% loads. Some NO to NO₂ conversion could have occurred via reaction with ozone in the transfer line, however this would only account for a 5% loss of NO under our sampling conditions.

Table 7. Criteria gas emission factors tests measured during the Pittsburgh test with the CFM56 engine.

| Date | Thrust Setting | NO (g kg-fuel ⁻¹) | NO _x (g kg-fuel ⁻¹) | CO (g kg-fuel ⁻¹) | SO ₂ (g kg-fuel ⁻¹) | CO ₂ at engine exit plane (%) |
|-------------|----------------|----------------------------------|--|----------------------------------|---|--|
| 16-Jul-2009 | 7% | a | a | a | a | a |
| 17-Jul-2009 | 30% | 8.7±0.6 | 8.7±0.6 | 7.5±0.7 | 1.3±0.2 | 3.00±0.3 |
| 20-Jul-2009 | 4% | 0.4±0.02 | 1.6±0.1 | 56.0±5.6 | 1.2±0.1 | 2.8±0.3 |
| 21-Jul-2009 | 4% | 0.4±0.02 | 1.9±0.1 | 66.5±6.6 | 1.1±0.1 | 2.8±0.3 |
| 22-Jul-2009 | 85% | 15.4±1.1 | 15.4±1.1 | 4.3±4.3 | 1.4±0.2 | 4.1±0.4 |
| 23-Jul-2009 | 7% | 1.3±0.09 | 2.5±0.2 | 60.4±6.0 | 1.2±0.1 | 2.8±0.3 |
| 24-Jul-2009 | 4% | 0.6±0.04 | 1.8±0.1 | ^b | 1.0±0.1 | ^b |

^aGas-phase data not available.

^bExhaust gas analyzer was not operated during this test; all measurements for this test are based on chamber data.

Table A1 (Appendix A) lists the emission factors (mg-pollutant kg-fuel⁻¹) for the volatile organic compounds (VOCs) measured using SUMMA canisters. The trends with load are illustrated in Figure 9, which plots the emissions of propene and the sum of single-ring aromatics. The hydrocarbon emissions at low load are dominated by small ($\leq C_4$) species, which fall off dramatically with increasing load. For example, propene emissions at 85% load are two orders of magnitude lower than at 4%. Emissions of single ring aromatics are highest at 4% and the fall off with load is less severe. Emissions of aromatics at 85% load are similar to those at 7%, and only a factor of 4 smaller than emissions at 4% load. Overall, the emissions of criteria and organic gases were similar to other CFM56 engines [10, 24].

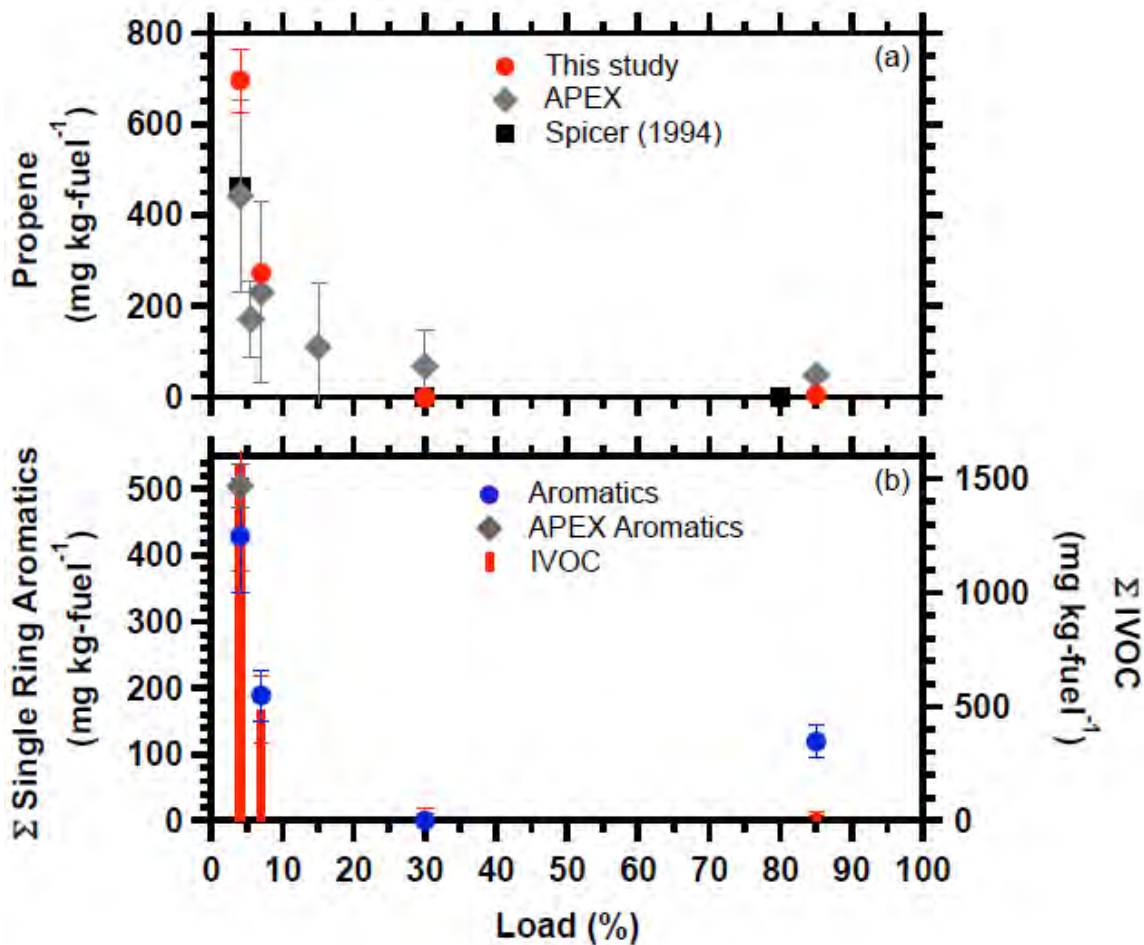


Figure 9. VOC emissions as function of load measured during the Pittsburgh tests (a) propene, (b) single-ring aromatics (sum of benzene, toluene, xylenes, ethyl benzene, styrene, ethyl toluene, and trimethyl benzenes) and IVOCs. APEX data in (a) are from the NASA multi-gas analyzer and in (b) from PTR-MS measurements [10]. Error bars for the APEX data show one standard deviation.

Primary PM Mass Emissions

Figure 10 compiles the measured the $\text{PM}_{2.5}$ mass, POA and EC emissions as a function of load measured during the Pittsburgh tests with the CFM56 engine. Data are presented for both the smog chamber (Figure 10a) and dilution sampler (Figure 10b). Particle emissions data based on the smog chamber measurements are shown in Table 8.

Table 8. Summary of primary aerosol emissions and secondary aerosol production measured during Pittsburgh tests of CFM56 engine. Uncertainty estimates are presented in parenthesis.

| Engine load | Primary PM emissions | | | Secondary PM production @ t = 3 hrs | | | |
|-------------|----------------------|-----------|-----------|-------------------------------------|----------|------------|-------------------------|
| | Mass ¹ | OC | EC | SOA | Sulfate | Nucleation | Primary-to-secondary PM |
| 4% | 27 (12) | 22 (9) | 3.0 (0.5) | 920 (170) | 244 (15) | Y | 35 (4.1) |
| 7% | 4.5 (0.5) | 9.5 (9) | 0.4 (0.1) | 42 (15) | 50 (5) | Y | 17 (2.5) |
| 30% | 3.0 (0.3) | 1.5 (0.4) | 1.8 (0.2) | 15 (8) | 70 (25) | Y | 60 (2.2) |
| 85% | 37 (12) | 13 (4) | 24 (4) | 15 (9) | 74 (15) | Y | 2.7 (1.1) |

*All units are expressed as mg kg-fuel⁻¹, unless otherwise noted

¹ PM mass is estimated using particle volume measured using SMPS and assumed particle density

For the smog chamber, PM mass was estimated from the particle volume measured using the SMPS measurements and an estimated particle density. For the dilution sampler, PM mass emissions are based on gravimetric analysis of Teflon filter samples. PM_{2.5} POA and EC emission factors are based on quartz filters samples collected in both the dilution sampler and chamber. We calculated the POA emission factor by multiplying the OC measured on the quartz filter by an assumed organic-mass-to-organic-carbon (OM/OC) ratio of 1.2, which assumes that the organic emissions are dominated by hydrocarbons. This assumption is appropriate for organic aerosol emissions from fossil-fuel based combustion systems [78].

Both the dilution sampler and smog chamber data indicate that the total PM_{2.5} mass emissions are highest at ground idle (4%) and high load (85%). However, there were more differences between the two sets of data at the intermediate load settings (7% and 30%). The trends of fine PM mass with load measured inside the smog chamber (Figure 10a) – higher emissions at 4% and 85%, lower emissions at 7% and 30% – are consistent with previous studies using CFM56 engines [3, 6, 10]. In comparison, the dilution sampler data suggest less load dependence.

The chemical composition data provides insight into both the variation in PM mass emissions with load and the differences between the dilution sampler and chamber data. Figure 10a indicates that the total PM mass measured in the smog chamber can be largely explained by the emissions of POA and EC. With the exception of 7% load, the PM mass balance for the in-chamber data (SMPS versus POA +EC) agrees to within 10%. As discussed below, evaluating the PM_{2.5} mass balance for the dilution sampler data is complicated by sampling artifacts on the quartz filter measurements of POA.

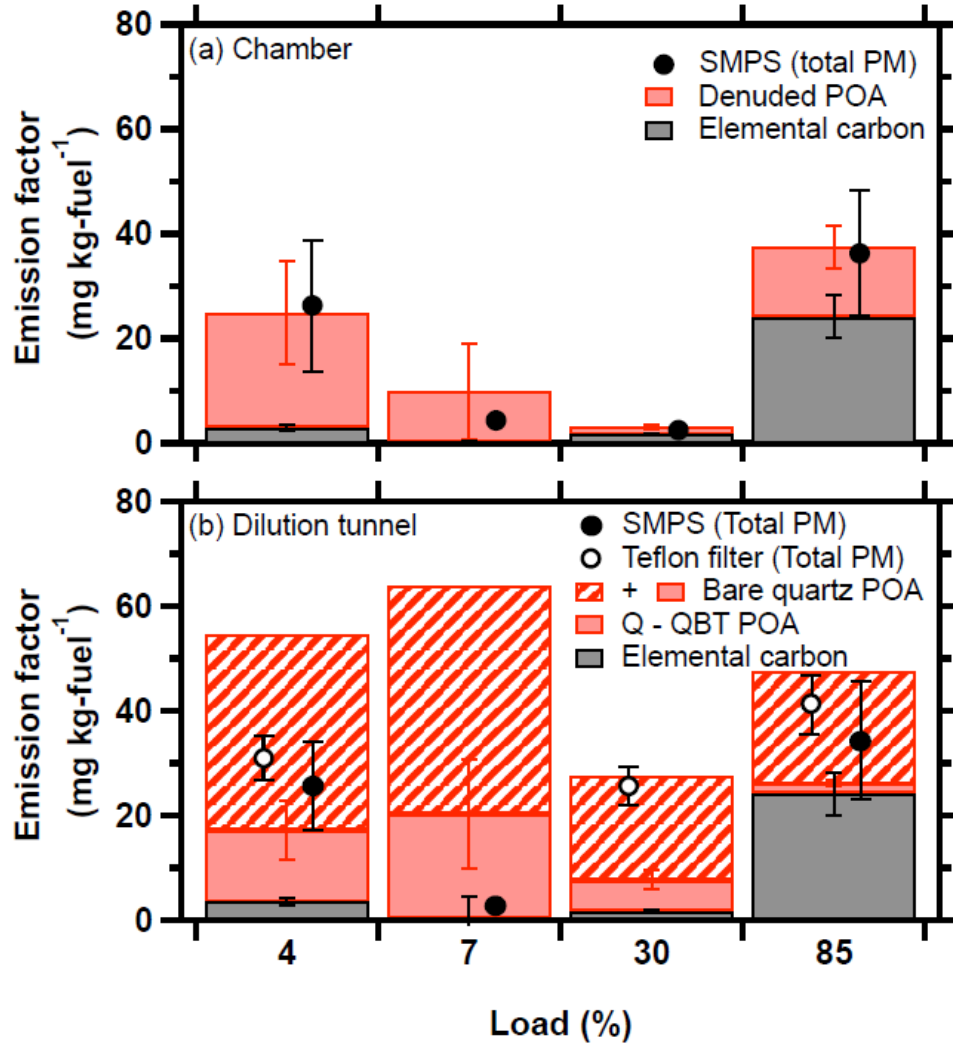


Figure 10. Total PM, primary organic aerosol (POA), and EC emissions as a function of load measured in the (a) smog chamber and (b) dilution tunnel during the Pittsburgh tests. As described in the text, panel (b) includes two estimates of the POA emissions. QBT = quartz behind Teflon filter, which provides an estimate of the positive sampling artifact. The data for the 4% and 7% loads shown are averages over multiple experiments conducted at those loads. The SMPS and Teflon filter data points are offset for clarity.

The emissions of EC are about an order of magnitude higher at the highest engine load (85%) than at the other load settings tested, similar to previous studies conducted with CFM56 engines [3, 6, 10]. Emissions of EC at 4% load are modestly higher than at 7% and 30%. Although this has been previously observed [3, 6, 10], the reason for the higher EC emissions at 4% is not obvious, as engine temperatures are lowest at that power setting. Our EC emission factors are in good agreement with the data of Agrawal et al. [3] except at 85% load where they are about a factor of two lower than the lowest EC emission factor reported by Agrawal et al. [3] at the same load. This difference could be due to our aircraft engine simply having lower emissions than previously studied

engines. It may also be due to non-isokinetic sampling at high engine loads or to differences in the aromatic content of the fuels. There is excellent agreement between the EC measurements in the chamber and dilution tunnel (Figure 10). Therefore, the discrepancies between the dilution sampler and in chamber PM measurements are not due to problems measuring non-volatile PM.

Figure 10 indicates poor agreement between the POA emissions measured using the chamber and dilution sampler. These measurements are discussed in detail in a subsequent section of this report. A major issue is that different techniques were used to measure the POA levels in the chamber and dilution sampler. However, despite the variability in the POA data, all of the measurements indicate that the POA emissions are substantial, exceeding the emissions of EC, at all of the tested loads except for 85%. The POA emissions are also the dominant component of the volatile PM emissions.

The lack of primary sulfate emissions is surprising given the relatively high fuel sulfur content (608 ppmw). Ion chromatography of the Teflon filters indicates small, load-independent emissions of PM_{2.5} sulfate (0.2 mg kg-fuel⁻¹). This implies either very little conversion of SO₂ to SO₃ in the engine (~0.01% of fuel sulfur by mass) or substantial losses of SO₃/H₂SO₄ in the sampling system. Other staged tests with similar fuel sulfur levels have also observed similarly small amounts of sulfate in samples collected using 1-m probes but significant sulfate in samples collected at 30 m [6]. Aircraft chase studies estimate SO₂ to sulfate conversions greater than 0.3% by mass [8].

Low-Volatility Organic Emissions

The data shown in Figure 10 indicate that POA is a major component of the PM mass, but the exact magnitude of the POA emissions is uncertain. In this section we investigate this uncertainty by comparing different measurements of POA: thermal-optical analysis of quartz filter samples, Aerosol Mass Spectrometer (AMS) analysis of chamber samples, and GC/MS analysis of sorbent and filter samples.

Sampling artifacts and Quartz filter measurements of POA

Sampling artifacts are a major challenge for measuring POA emissions with quartz filters. Adsorption of low-volatility organic vapors causes a positive artifact (overestimate of POA) while evaporation of particulate carbon causes a negative artifact [48, 49, 79]. We are not aware of data on filter sampling artifacts for aircraft exhaust, but tests with other combustion systems generally report large positive sampling artifacts on quartz filters [2]. Sampling artifacts are commonly estimated using a combination of back up filters and/or denuders. We used both approaches in this study.

Figure 10 shows three different estimates of the POA emissions based on quartz filter data collected using the dilution sampler and smog chamber. Two estimates are available for the dilution sampler: the OC collected on a bare quartz filter (red plus red hatched bar in Figure 10b) and an artifact corrected estimate (red bar in Figure 10b). The smog chamber OC measurements were made using a quartz filter downstream of an activated carbon denuder, which removes organic vapors to reduce artifact. Unfortunately the same method was not used in both the smog chamber and dilution sampler, complicating comparisons between the two datasets.

The non-artifact corrected bare quartz filter measurements collected using the dilution tunnel provides the highest estimate of POA emissions, exceeding the EC emissions at all loads. However, a substantial fraction of that carbon is likely positive artifact. The OC measured on a quartz-behind-Teflon (QBT) filter provides an estimate for positive sampling artifacts associated with adsorption of organic vapors [48, 49]. The basic idea is that the Teflon filter removes the particles so the back-up quartz filter collects only vapors.

Figure 10b shows QBT data collected using the dilution sampler at different engine loads. At every load, the OC measured on the QBT filter was more than half of that measured on the bare quartz filter, indicating substantial adsorption of organic vapors (positive artifact). In fact, at 4% load, the POA measured on the bare quartz filter was larger than the total PM mass measured using the Teflon filter. Therefore the bare quartz data collected with the dilution sampler substantially overestimate the POA emissions. The large sampling artifact indicates that there are large amounts of low-volatility organic vapors in the diluted exhaust.

Figure 10 also presents two artifact corrected estimates of the POA emissions. The first is the bare quartz filter OC minus the QBT OC measured with the dilution sampler (Figure 10b). The second is the denuded OC measured with the smog chamber (Figure 10a). Although there are some differences between these two estimates, both estimates indicate that the POA emissions are the dominant component of the PM mass emissions at every load except 85%. We attribute the discrepancy between the two artifact corrected estimates of POA to two factors. First, both the denuder and the backup filter approaches are imperfect. For example, ambient measurements suggest that both approaches likely overestimate by different amounts the sampling artifacts and therefore underestimate the POA emissions [48]. Second, gas-particle partitioning of the POA is likely different in the dilution chamber and the smog chamber. This second explanation is discussed in the next section.

Semivolatile POA and evolving gas-particle partitioning

Differences in gas-particle partitioning likely contribute to the variability of the POA emissions data shown in Figure 10. SVOCs dynamically partition between the particle and vapor phases as the exhaust is diluted or cooled [40, 80]. If SVOCs contribute a significant fraction of the POA mass then the POA emission factor depends on temperature and the total concentration of organic species in the diluted exhaust [40, 80]. However, the relative contribution of SVOCs to the POA in aircraft emissions is not known.

To investigate the gas-particle partitioning of POA, Figure 11 presents a partitioning plot in which the POA emission factor is plotted as a function of C_{OA} (organic aerosol concentration) while exhaust was being injected into the chamber during an experiment conducted at 4% load. The experimental approach is described by Ranjan et al. [42]. As the chamber was filled the concentration of organic aerosol (C_{OA}) inside the chamber increased. According to partitioning theory [2, 80], the POA emission factor should increase with increasing C_{OA} due to changes in gas-particle partitioning. Increasing either C_{OA} or the total concentration of low-volatility organic compounds drives up the POA

emission factor because of condensation of organic vapors. This is exactly what is shown in Figure 11. The POA emission factor as measured with an SMPS increased by more than a factor of 2 as the C_{OA} inside the chamber changed from 0.7 to $4 \mu\text{g m}^{-3}$. This implies a substantial fraction of the POA emissions are SVOCs. As expected, Figure 11 shows that the black carbon emission factor (a non-volatile component of the PM) remains constant as the chamber is filled with diluted exhaust.

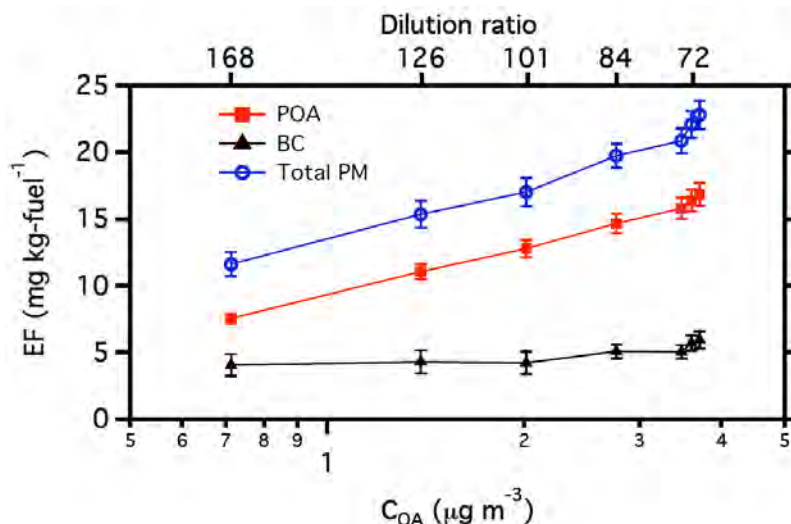


Figure 11. Partitioning plot showing the POA emission factor as a function of organic aerosol concentration (C_{OA}) measured while emissions were injected into the smog chamber at 4% load. Also shown is the BC emission factor inside the chamber, which does not change as more exhaust is injected into the chamber. Lines are included to guide the eye.

Figure 11 cannot be explained by particle-particle interactions such as coagulation. Coagulation alters particle number, but not particle mass. The most likely explanation for the behavior observed in Figure 11 is dynamic gas-to-particle partitioning of organic species accompanied by constant emissions of nonvolatile (and therefore non-partitioning) BC.

The thermodenuder measurements support the conclusion that the POA emissions from the CFM56 engine are semivolatile. Figure 12 plots the organic aerosol mass fraction remaining (MFR) measured downstream of the thermodenuder as a function of thermodenuder temperature. At all load conditions, there was significant evaporation of the POA with modest heating. The temperature at which 50% of the POA emissions have evaporated is between 80 and 100 °C.

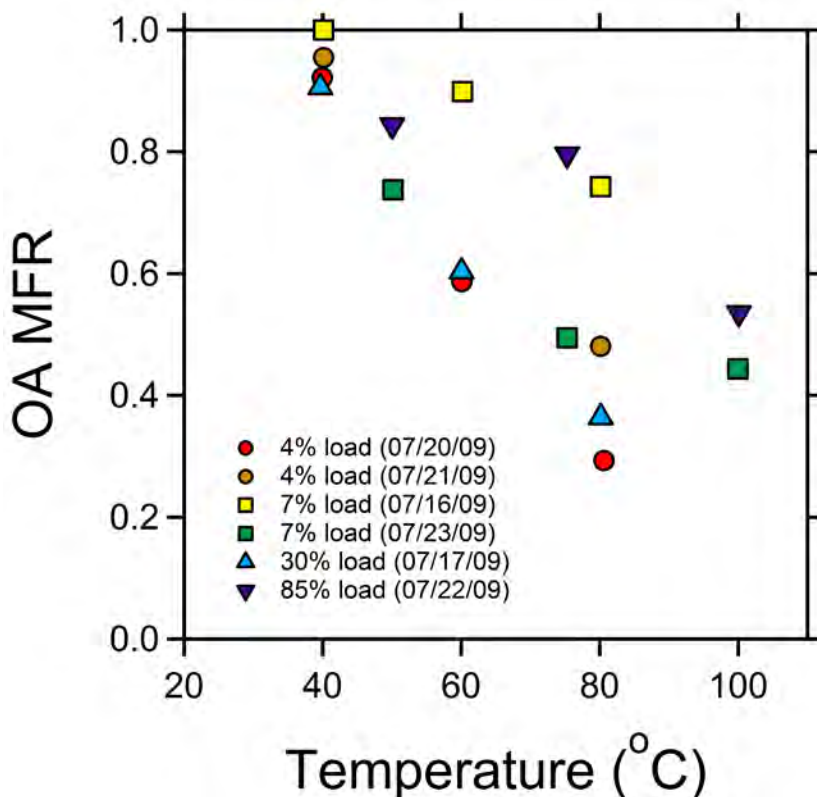


Figure 12. Thermodenuder measurements of fresh primary organic aerosol volatility from the Pittsburgh tests. OA MFR – organic aerosol mass fraction remaining.

Variable gas-particle partitioning of POA likely explains some of the differences between the dilution sampler and smog chamber shown in Figure 10. Because a substantial portion of the POA appears to be semivolatile, the POA emission factor depends on temperature and concentration of organic aerosol (C_{OA}) at the measurement point [40, 80]. The C_{OA} inside the dilution sampler and chamber were different, the gas-particle partitioning of the POA in these two systems was different.

GC-MS analysis of low-volatility organics

GC-MS analysis of the quartz filter and Tenax sorbent samples were also used to quantify the emissions of low-volatility organics. The filters collected the particulate organics plus some vapors as positive artifact; the Tenax sorbent collected vapors. Table A2 (Appendix A) lists emission factors for about 60 individual compounds including C_{12} and larger *n*-alkanes, naphthalene, substituted naphthalenes, 3-ring PAHs, and select petroleum biomarkers. However, the identified species contribute only a small fraction (5-15%) of the low volatility organic emissions.

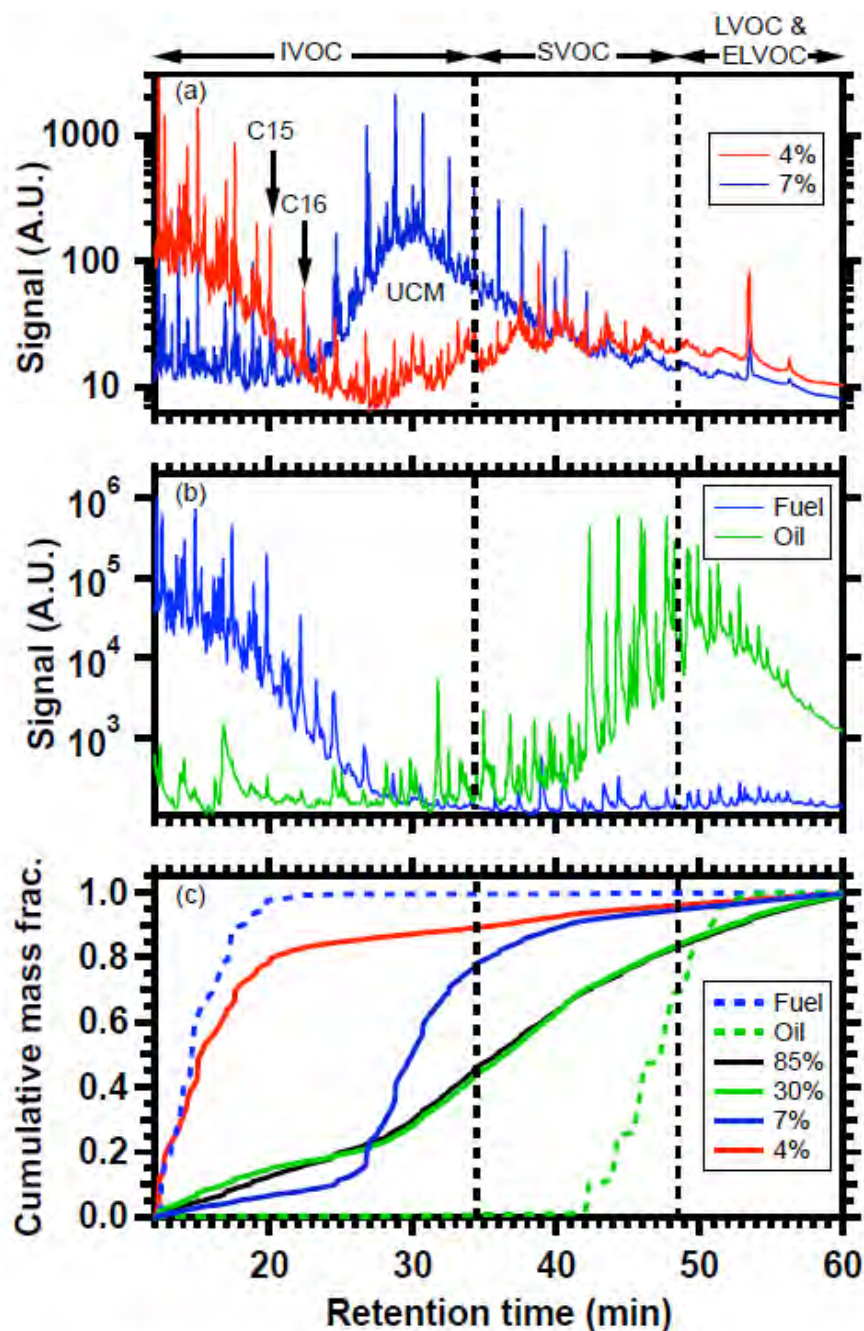


Figure 13. (a) Chromatograms of m/z 57 signal from quartz filter and Tenax sorbent samples collected at 4% and 7% load; (b) m/z 57 chromatograms of the JP8 fuel and lubricating oil used in these tests; and (c) cumulative distributions of m/z 57 chromatograms of emissions collected at 4%, 7%, 30%, and 85% loads, as well as jet fuel and jet lubricating oil. Volatility (C^* , $\mu\text{g m}^{-3}$) decreases with increasing retention time in the GC. The indicated elution times for IVOCs, SVOCs, and LVOC/ELVOC are based on n -alkanes.

To examine the properties of the bulk of the low-volatility organic emissions, Figure 13 shows selected ion mode chromatograms for m/z 57 for samples collected at 4% and 7% load and for the JP8 fuel and lubricating oil used in the aircraft. M/z 57 is the dominant hydrocarbon fragment in the mass spectrum. The emissions data shown in Figure 13 are the sum of the quartz filter plus the downstream Tenax signals, which were scaled using the recovery of the deuterated internal standard and for flow through the different media. Peaks corresponding to resolved species, such as n -alkanes, are clearly visible. However, the majority of the signal appears as broad humps of unresolved hydrocarbons commonly called the “unresolved complex mixture” or UCM [27, 81]. For example, Figure 13a shows there are two UCM humps at 4% load and a single broad hump at 7% load. The UCM is thought to be composed of branched and cyclic hydrocarbons that are not separated by standard one-dimensional chromatography [27, 81].

The GC was equipped with an Agilent HP-5ms capillary column, which primarily separates analytes by volatility. Therefore, the elution time provides a measure of the UCM volatility [82, 83]. Using the elution time and literature C^* values for n -alkanes we categorized the volatility of the UCM humps. We classified the organics into three volatility categories: IVOCs ($10^6 \geq C^* \geq 10^3 \mu\text{g m}^{-3}$); SVOCs ($10^2 \geq C^* \geq 10^{-1} \mu\text{g m}^{-3}$); and LVOCs/ELVOCs (low-volatility and extremely-low volatility organic compounds; $C^* < 10^{-1} \mu\text{g m}^{-3}$). The elution times for these different categories are shown in Figure 13.

Cumulative distributions of the m/z 57 chromatograms are plotted in Figure 13c to compare the volatility distribution of emissions at different loads to each other and to the JP8 fuel and aircraft lubricating oil. The first hump in the 4% data (<27 minutes) is comprised of IVOCs, which closely resembles the JP8 fuel m/z 57 chromatogram shown in Figure 13b. About 80% of the low-volatility organics emitted at 4% load appear to be unburned fuel. A strong fuel signal was only observed at 4% load. The later-eluting UCM humps show some overlap with the jet lubricating oil chromatogram shown in Figure 13b, but the emissions have a broader range of volatilities than the oil and don't show a clear peak in the SVOC or LVOC/ELVOC range. For example, all of the emissions data in the SVOC range are shifted to higher volatility (lower retention time) compared to the oil. Therefore, the SVOC emissions are likely composed of mixture of partially burned fuel and oil.

Mass balance on organic emissions

We combined the GC-MS data for the Tenax and filter samples with the VOC data to evaluate the overall mass balance of the organic emissions. This sort of analysis has been done for emissions from other combustion systems [27-29], but not for aircraft exhaust. The UCM mass was estimated using calibration factors based on the m/z 57 signal of fuel and oil samples collected from the aircraft. The precision in this UCM quantification is estimated to be $\pm 30\%$.

The distribution of organics measured at 4% and 85% loads is presented in Figure 14 (these are the two loads with comprehensive VOC data). Speciated VOCs contribute about 80% of the measured organic emissions at 4% load. The next most abundant portion of the organic emissions is the IVOCs (~20%). SVOCs and LVOC/ELVOC

emissions contribute <1% of the total organic emissions. At 85% load, speciated VOCs contribute 90% of the organic emissions. IVOCs make up 7% of the organic emissions, and SVOCs and LVOC/ELVOC contribute 3%. Similar to emissions from other combustion systems [27, 28, 84], the vast majority (>90%) of the low volatility organics (IVOC, SVOC, LVOC/ELVOC) could not be speciated and are classified as UCM.

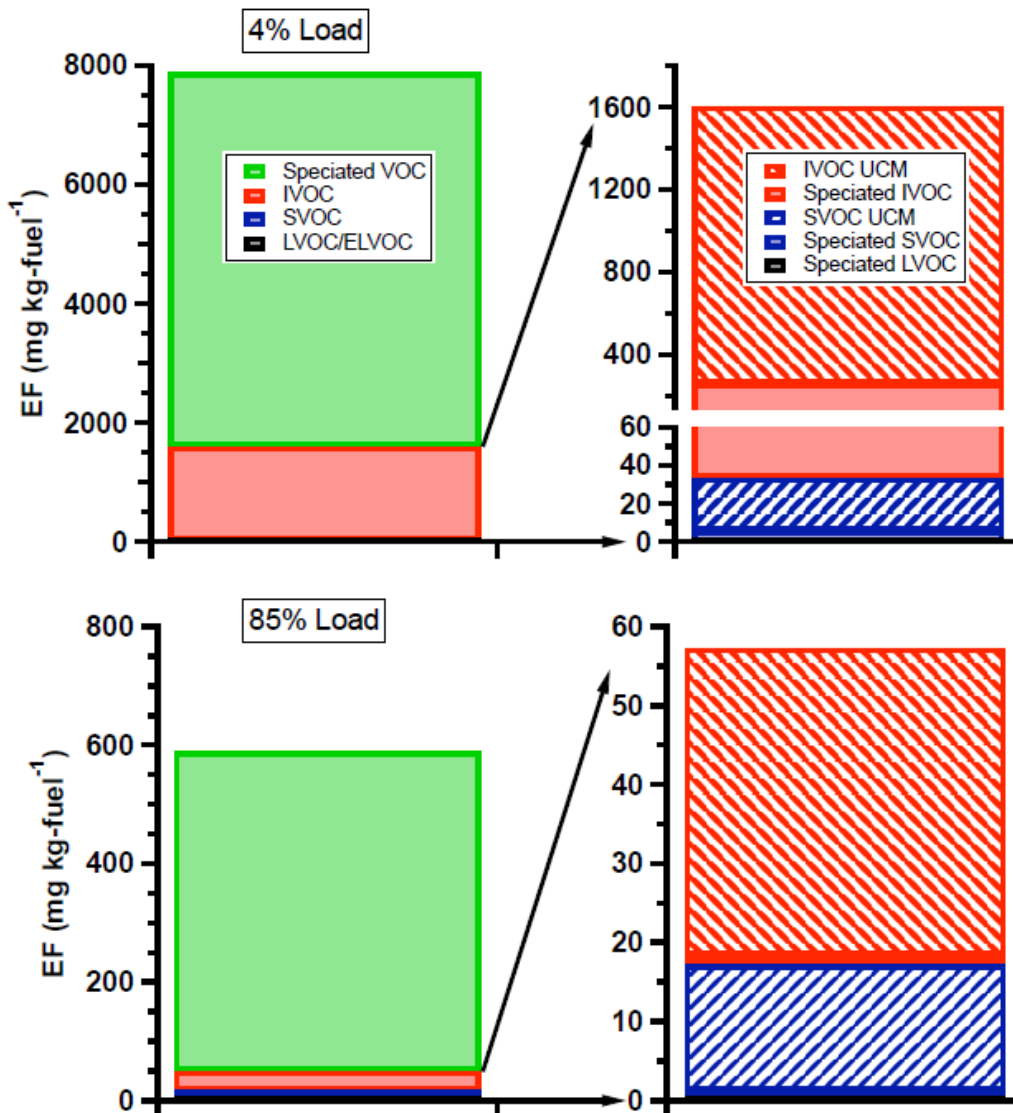


Figure 14. Distribution of measured organic emissions at 4% and 85% load. The panels on the left side show the distribution of emissions between VOC, IVOC, SVOC, and LVOC/ELVOC. The panels on the right side show details of the low-volatility emissions, and split the IVOC and SVOC emissions into speciated and UCM fragments.

The sum of SVOC+LVOC+ELVOC in Figure 14 (and Table A2) should be larger than the POA emission factors because the SVOCs partition between the vapor and condensed phases while the LVOC/ELVOC exist almost exclusively in the condensed phase. At 85% load, the POA EF (Figure 10a) is 13.3 ± 4.0 mg kg-fuel⁻¹, which is less than

the sum of SVOC+LVOC+ELVOC (17 ± 6 mg kg-fuel⁻¹). At 4% load, the POA EF is 22.0 ± 10 mg kg-fuel⁻¹, which is less than SVOC+LVOC+ELVOC of 33 ± 10 mg kg-fuel⁻¹. The large amounts of low-volatility vapors explain the substantial adsorption artifact measured on the quartz filters.

To illustrate the load dependence of the low-volatile organic emissions, Figure 9b plots the total IVOC emissions at the four tested engine loads. The total IVOC emissions are the sum of the UCM and speciated emissions (Table A2, Appendix A). The variation in IVOC emissions with load is qualitatively similar to the emissions of organic PM and single-ring aromatic species: IVOC emission factors are more than three times higher at 4% load than at the other loads, consistent with substantial unburned fuel emissions at ground idle. The lowest IVOC emissions are at 30% and 85% load, suggesting more efficient combustion than at idle (4% and 7% load). The total SVOC emissions (UCM + speciated, Table A2) do not show a strong dependence on load. They are equivalent (within measurement uncertainty) at 4%, 7%, and 30% load.

Photo-oxidation and secondary aerosol production

After characterizing the primary emissions, the emissions were aged in the smog chamber. Figure 15 shows time-series of gas- and particle-phase concentrations measured inside the smog chamber during a typical experiment conducted with exhaust from 4% engine load. Each experiment can be divided into three periods: bag filling, during which exhaust was added to the chamber; primary emission characterization, when the chamber contents were characterized in the dark; and photo-oxidation, when the chamber was exposed to UV light.

Figure 15a plots measured NO, CO₂, CO, SO₂, and O₃ data measured inside the smog chamber. Concentrations of primary species (NO, CO₂, CO, SO₂) increased during bag-filling phase of the experiment as exhaust was added to the chamber. In the experiment shown in Figure 15, the concentration of CO₂ increased from approximately 400 to 950 ppmv and then remained constant throughout the primary characterization and photochemical aging periods. When the lights were turned on, the concentration of O₃ increased, while NO decreased due to photochemistry. Photo-oxidation also reduced the concentration of SO₂; the measured decay of SO₂ was used to estimate OH concentrations inside the chamber using an OH rate constant of 1.5×10^{-12} cm³ molecules⁻¹ s⁻¹ [85]. The average OH concentration in the experiment shown in Figure 15 was 1.4×10^7 molecules cm⁻³ which is representative of typical summertime conditions.

Time-series of particle-phase data from the AMS and SMPS are plotted in Figure 15b, including AMS non-refractory mass and SMPS total volume, number concentrations and volume median diameter. The vertical gray bars in Figure 15b indicate periods when the aerosol was through the thermodenuder (TD).

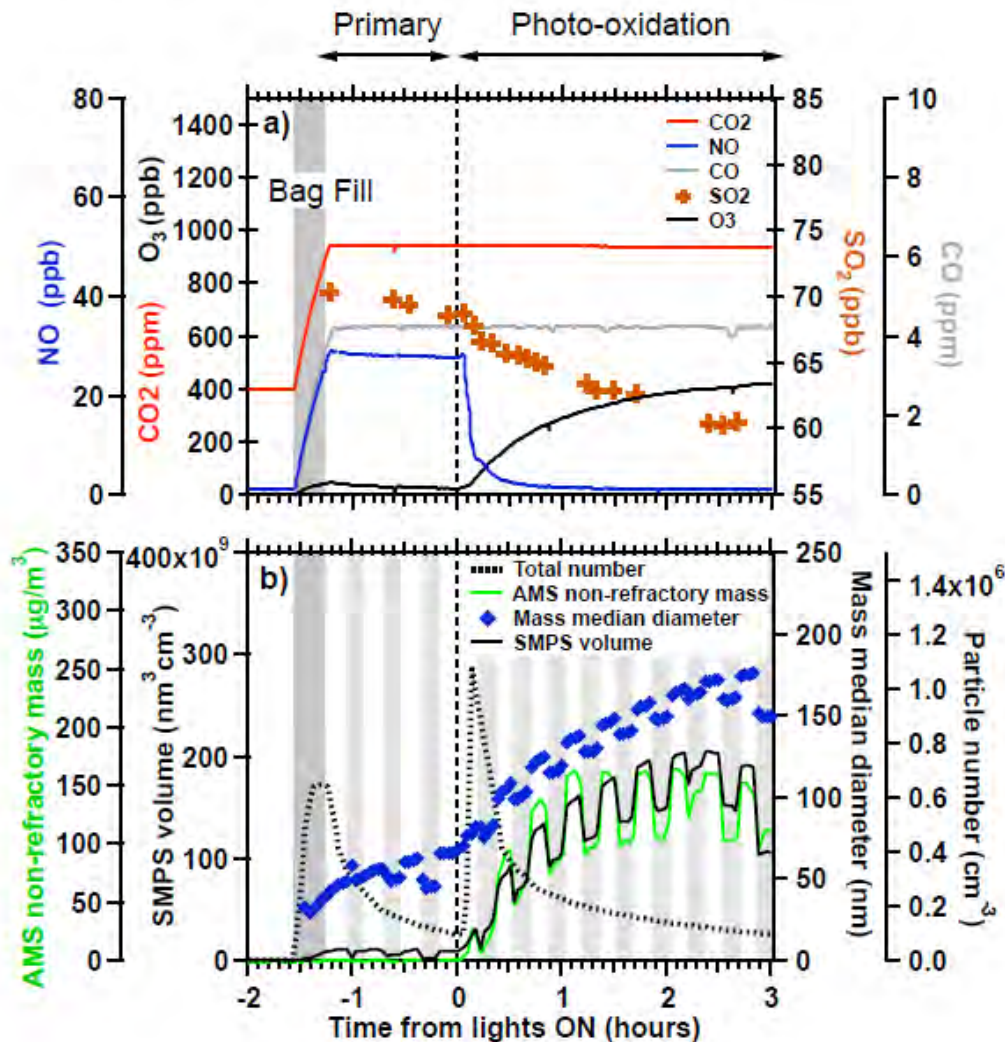


Figure 15. Time series of a) gas and b) particle-phase concentrations measured during a photo-oxidation experiment conducted at 4% engine load. Vertical gray bars indicate period when bag is filled with exhaust or when the aerosol was passed through the thermodenuder.

Aerosol concentrations increased when exhaust was injected into the chamber. During the primary characterization phase of the experiment, the measured aerosol mass and number decreased, as particles were lost to the chamber walls (Figure 15b). Coagulation also caused the particles to grow; the mass-weighted median diameter increased from approximately 35 to 65 nm over the 1 hour primary characterization period. After the UV lights were turned on ($t = 0$ hrs), there was substantial secondary PM mass production and the particle volume median diameter grew to about 180 nm. Evaporation inside the TD caused the particles to shrink and the measured non-refractory AMS mass and SMPS total volume concentrations to decrease.

Figure 15b shows that photo-oxidation also sharply increased particle number concentrations indicating nucleation inside the chamber. Figure 16 plots particle size distribution measured inside the smog chamber at four different times during this experiment. Immediately after filling, the number median diameter of the primary PM emissions inside the chamber was 35 nm, which grew to about 65 nm due to coagulation during the 1-hr primary characterization period. Immediately after turning on the lights, there was a strong burst of new particle formation which created a bimodal size distribution with a 20 nm “nucleation” mode and a larger primary mode (~75 nm). Therefore, nucleation created an externally mixed aerosol, with a nucleation mode comprised of sulfate and organic particles and larger mode with primary core. The AMS data indicate that the larger size mode is composed of both organic and sulfate particles. Additional photo-oxidation caused rapid and substantial growth in the median particle diameter of both modes. By the end of the experiments, the two modes have largely merged due to coagulation.

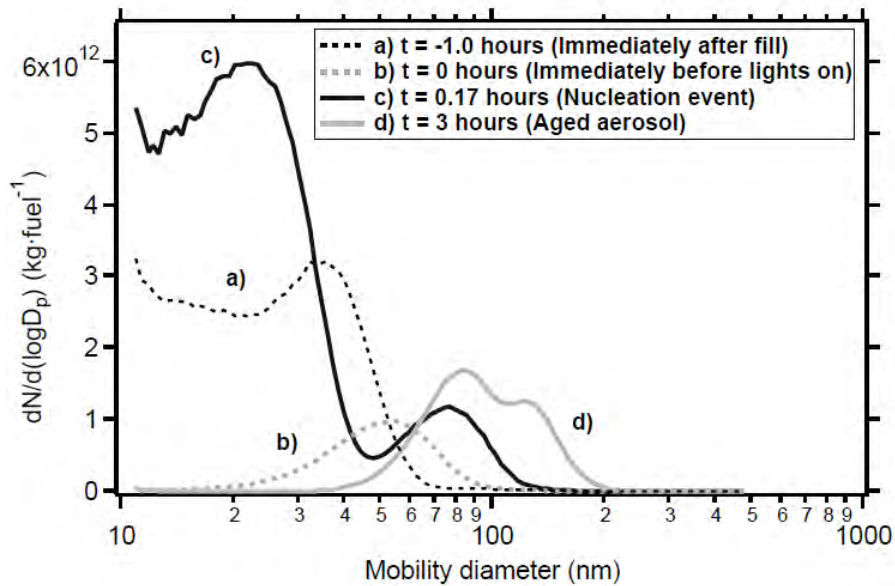


Figure 16. Size distributions measured a) immediately after fill, b) immediately before lights on, c) nucleation event (shortly after lights on), and d) aged aerosol (after 3 hr of oxidation). The data are from a 4% load experiment. The decrease in particle number is due to a combination of coagulation and particle losses to the chamber walls.

Nucleation was observed in every experiment (all engine loads) shortly after the onset of photo-oxidation ($t=0$). Particle nucleation events are strong, increasing particle concentrations in the chamber between a factor of 3 (85% load) and 15 (30% load). However, the particles quickly coagulate, decreasing the particle number enhancement ratio throughout the oxidation period.

To summarize the effects of photo-oxidation on PM mass across the set of experiments, Figure 17 plots time-series of the wall-loss corrected mass inside the chamber measured at the four different engine loads. All of the data are wall-loss corrected assuming $\omega=0$, which provides a lower-bound estimate of the formation of

secondary aerosol because it does not account for the loss of condensable vapors to the chamber. To quantify the relative importance of secondary PM production, the ratio of the secondary-to-primary PM is plotted on the right axis.

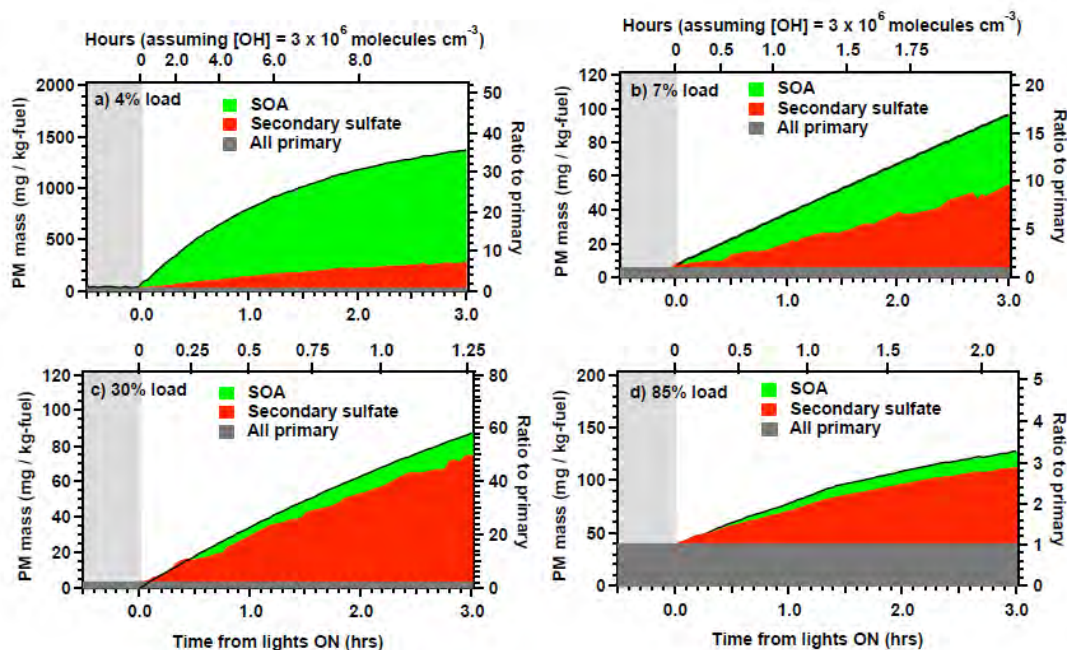


Figure 17. Changes in wall-loss corrected PM mass caused by photo-oxidation at (a) 4% load, (b) 7% load, (c) 30% load, and (d) 85% load. The top axis indicates time for OH exposure assuming a constant [OH] concentration of 3×10^6 molecules cm^{-3} . The ratio of secondary-to-primary PM mass is plotted on the right axis. Note different scales on each panel.

Figure 17 indicates that photo-oxidation created substantial secondary PM mass in every experiment. At the end of the experiment, the ratio of secondary to primary PM mass was 35 ± 4.1 , 17 ± 2.5 , 60 ± 2.2 , and 2.7 ± 1.1 times greater than the primary PM for the 4, 7, 30, and 85% load experiments, respectively. Therefore, secondary PM production rapidly exceeds the direct, primary particle emissions.

In order to compare formation of secondary PM across experiments at different engine loads, one must account for differences in hydroxyl radical (OH) concentrations. OH concentrations were inferred from the measured decay of SO_2 using published kinetic data. The average OH concentration for each experiment is listed in Table 9. OH concentrations for 4% load experiments were an order of magnitude higher ($\sim 10^7$ molecules cm^{-3}) than for the higher load (7, 30, 85 %) experiments ($\sim 10^6$ molecules cm^{-3}). Therefore, several hours of oxidation for the 4% load experiment results in a greater integrated OH exposure ([OH] x time) than for the higher load experiments.

Table 9. Summary of aging conditions for experiments conducted at the Pittsburgh airport.

| Experiment date | Thrust setting | UV light source | Average [OH] (molecules/cm ³) |
|-----------------|------------------|-----------------|---|
| 07/15/09 | 7% | Black lights | ^a |
| 07/16/09 | 7% | Sunlight | ^a |
| 07/17/09 | 30% | Black lights | 1.3 x 10 ⁶ |
| 07/20/09 | 4% | Black lights | 1.4 x 10 ⁷ |
| 07/21/09 | 4% | Sunlight | 1.2 x 10 ⁷ |
| 07/22/09 | 85% | Sunlight | 1.9 x 10 ⁶ |
| 07/23/09 | 7% (center port) | Black lights | 1.9 x 10 ⁶ |
| 07/24/09 | 4% | Black lights | 1.0 x 10 ⁷ |

^aNo SO₂ data collected.

The top axes on Figure 17 indicates the OH exposure expressed in units of time by assuming a constant OH concentration of 3×10^6 molecules cm⁻³, which is a typical summertime OH concentration. Therefore, this axis illustrates the evolution of PM emissions on an atmospherically relevant time scale. It takes only minutes of exposure to typical summertime OH levels for the secondary PM concentrations to exceed the primary PM emissions at every load. Therefore, secondary PM production must be accounted for when assessing influence of aircraft emissions on ground-level PM concentrations near airports.

The composition of secondary PM formed varied for each engine load, depending on the amount of SOA production. For emissions at 4% load, SOA formation dominated the secondary aerosol production (Figure 17a). At higher loads, sulfate contributed the majority of the secondary PM mass. Since sulfate formation is a function of fuel sulfur content and OH exposure (and not engine load), the load dependence in secondary PM production are driven by differences in SOA production.

Figure 18a compares the total SOA production as measured at the end of each experiment at the four different engine loads. The error bars in Figure 18a represent the uncertainty associated with the particle wall-loss rate, the loss of semivolatile vapors to the chamber walls ($\omega=0$ and $\omega=1$), and the two estimates of secondary sulfate production. On a fuel basis, SOA production at 4% was a factor of 20, or more, higher than that measured at the other load conditions. The peak production was at 4% load and a minimum at 30% engine load.

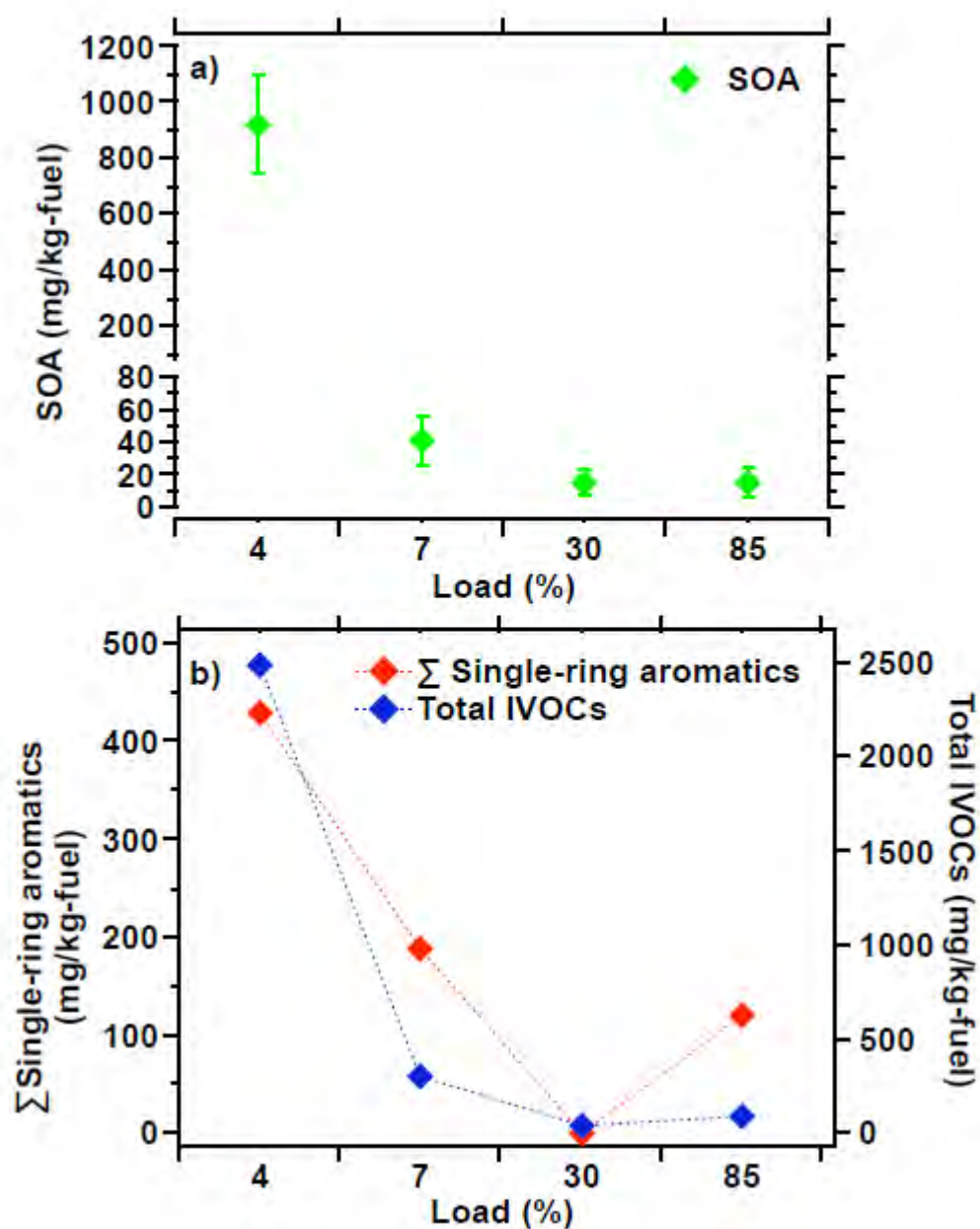


Figure 18. a) SOA mass measured at the end of the aging phase of the experiment. b) Sum of single-ring aromatic compounds and sum of IVOC emissions. Data are presented as a function of engine load. Single-ring aromatics include benzene, toluene, xylenes, ethyl benzene, styrene, ethyl toluene, and trimethyl benzenes. IVOCs includes speciated compounds and unresolved complex mixture collected on the Tenax sorbent (UCM).

Organic aerosol composition and volatility

Figure 19 plots OA mass spectra measured using the AMS. A comparison of average primary and aged OA mass spectra from three 4% load experiments is shown in Figure 19a. The POA mass spectrum was dominated by the C_nH_{2n-1} and C_nH_{2n+1} mass fragments, which are typical of fresh hydrocarbon-like aerosol [86]. Aircraft POA also has significant contributions from ions in the C_nH_{2n+1} (43, 57, etc.) series as well as m/z 44 (4.3%). The m/z 44 fragment (CO_2^+) is an indicator of oxygen content in organic aerosol; aircraft POA is somewhat more oxygenated than POA emitted by other sources such as diesel engines [51].

Photo-oxidation increases the AMS signal at oxygenated fragments (m/z 29, 43, 44, etc.) and decreases the signal in the fragments associated with the primary emissions (m/z 41, 55, 57 etc.). These general trends are similar to that observed during photo-oxidation of emissions from other combustion sources [87, 88].

Figure 19b shows the average time evolution of AMS fragments m/z 44 and 57 for the 4% load experiments. The AMS signal at m/z 44 (CO_2^+) is a widely used marker for the extent of oxygenation in organic aerosol [86], while the signal at m/z 57 is used as a tracer for primary organic aerosol (POA) [87]. The data show a dramatic change in OA composition during the first 20 minutes of oxidation due to SOA production, with the contribution of f_{57} (fractional contribution of m/z 57 to the total OA signal) decreasing from approximately 5% to 1.4% and the contribution of m/z 44 increasing from 6% in the POA to approximately 8.5% in the aged aerosol. After approximately 20 minutes of oxidation, the AMS mass spectrum of OA stops changing. At this point the OA inside the chamber is dominated by SOA at 4% load (Figure 19a). Even though SOA is produced throughout the experiment, the composition of the SOA (as measured with the AMS) does not appear to change.

Changes in OA volatility with photo-oxidation are shown in Figure 20a, which plots OA mass fraction remaining (MFR) as a function of temperature (thermograms) for POA, aged OA, and the AMS fragments m/z 44 and 57 for aerosol sampled at 4% engine load. Both the primary and aged aircraft OA are semivolatile and that photo-oxidation reduces volatility of the OA. The thermogravimetric data indicate that the differences in volatility are due to a “tail” of lower volatility material. Similar to other types of OA, the compounds that contribute to the AMS signal at m/z 44 are less volatile than the total OA, while the material contributing to the m/z 57 signal is more volatile. This behavior is similar to data from wood smoke aging experiments [56] and ambient measurements.

Changes in OA volatility as a function of time are shown in Figure 20b, which plots the evolution of the OA MFR at 60 °C throughout the photo-oxidation period. The dip immediately after photo-oxidation begins indicates that the initial SOA formed in the chamber is much less volatile than the POA or the SOA formed in the later stages of the experiment. This change in volatility is the opposite of f_{44} (Figure 19b), which indicates that the low-volatility SOA formed immediately after the lights are turned on is comprised of relatively reduced compounds. As the SOA becomes more oxygenated (larger f_{44}), the MFR at 60 °C increases to around the same value as the POA.

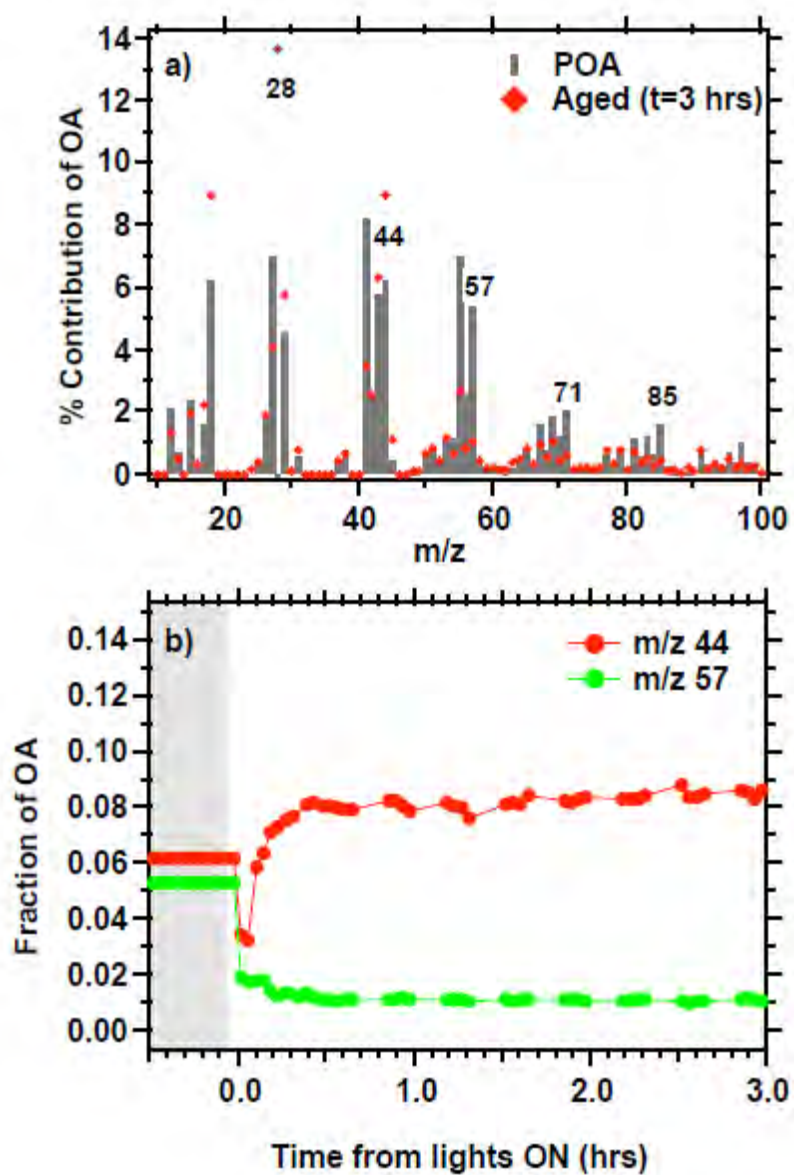


Figure 19. a) Average AMS mass spectra of primary and aged OA. b) Time evolution of AMS f_{44} and f_{57} . Data are averages of all experiments conducted at 4% load. Only undenuded (no TD) data are shown.

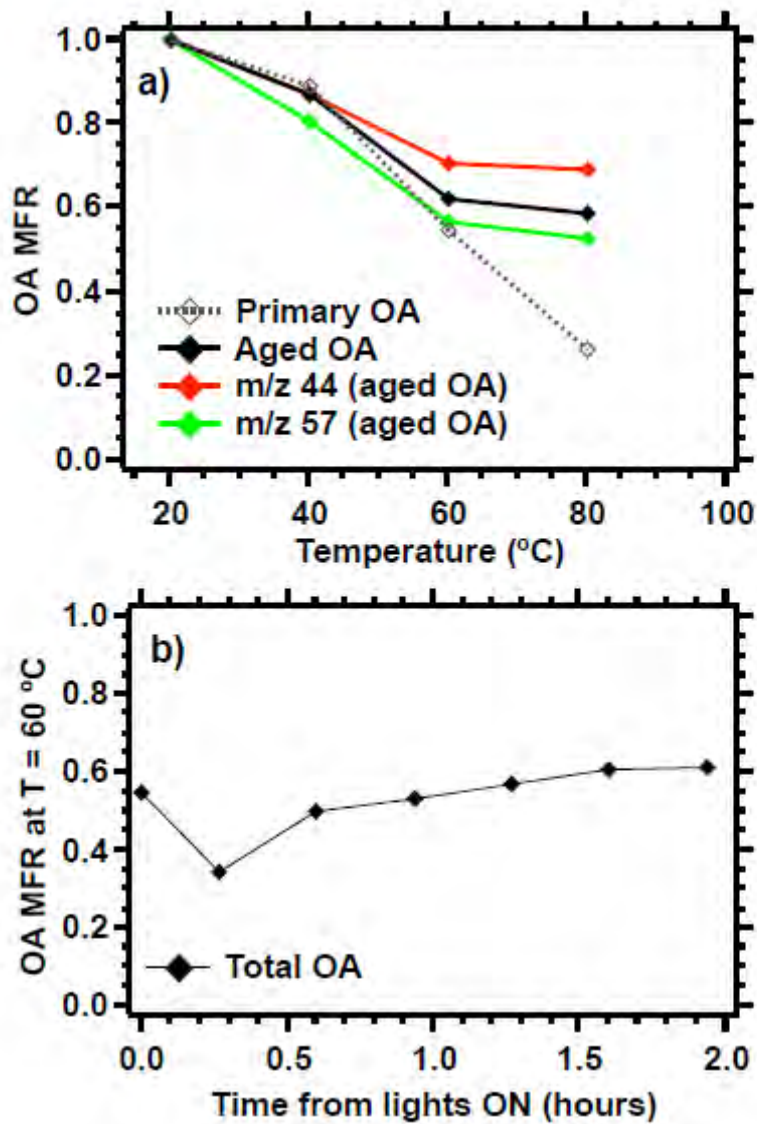


Figure 20. a) Average thermograms for primary OA, aged OA, and AMS fragments m/z 44 and 57 for the aged aerosol. b) Evolution of total OA volatility at $T = 60$ °C during the photo-oxidation phase of the experiment. Data are from a 4% engine load experiment. Lines are included to help guide the eye.

Wright Patterson Tests

Gaseous Emissions

A summary of the gaseous emission measurements from the Wright Patterson experiments is shown in Table 10. Speciated VOC emissions are shown in Table A3. The total VOC emissions were high at idle load, 9-11 g/kg-fuel, and about a factor of ten lower at cruise load, 0.2 - 0.5 g/kg-fuel. The VOC emissions are primarily comprised of small, unsaturated hydrocarbons. At idle, VOC with carbon numbers less than 6 contribute 70-80% of total HC emissions. At cruise, the contribution of small VOCs ($\leq C_6$) emissions was $\sim 70\%$ of the total hydrocarbon emissions when the engine was operated on JP8 but more than 98% when operated on FT. At idle, the total hydrocarbon emissions were about 80% unsaturated (olefinic or aromatic) VOCs versus 40 to 50% at cruise load.

While the magnitude of the VOC emissions were relatively similar when the engine was operated on JP8 and FT at a given engine load, the emissions of other gaseous species exhibited a stronger dependence with fuel composition. As expected (given the negligible sulfur content of the FT), SO_2 emissions were much higher when operating the engine on JP8 than FT. Naphthalene and alkylated naphthalene emissions were much lower when the engine was operated on JP8 than FT. For the blend, the emissions of gaseous species generally fell between the two neat cases.

Table 10. Gaseous and particulate matter emissions factors for a T63 engine measured during the Wright Patterson experiments.

| | Units | Idle | | | Cruise | |
|---|--------------|------|-------|------|--------|------|
| | | JP8 | Blend | FT | JP8 | FT |
| <u>Gases</u> | | | | | | |
| CO ₂ | % vol. | 2.74 | 2.67 | 2.73 | 1.94 | 2.54 |
| CO | g/kg-fuel | 0.69 | 0.59 | 0.69 | BDL | BDL |
| SO ₂ | g/kg-fuel | 1.02 | 0.63 | 0.01 | 1.54 | 0.1 |
| Total VOC | g/kg-fuel | 9.62 | 11.45 | 9.21 | 0.53 | 0.22 |
| Low MW VOC(≤C5) | % VOC | 82 | 70 | 78 | 69 | 98 |
| Unsaturated VOC | % VOC | 87 | 81 | 80 | 40 | 50 |
| Low-volatility organics (Tenax + quartz filter) | g/kg-fuel | 5.4 | 3.92 | 1.21 | 0.04 | 0.02 |
| <u>Particulate Matter</u> | | | | | | |
| Total PM | mg/kg-fuel | 550 | 285 | 191 | 430 | 84 |
| OC (artifact corrected / Q - QBT) | mg-C/kg-fuel | 469 | 229 | 122 | 14 | 3 |
| EC | mg/kg-fuel | 85 | 30 | 3 | 229 | 108 |
| Sulfate | mg/kg-fuel | 1.9 | 1.9 | 0.44 | 5.5 | 0 |

Particulate Matter Emissions

Table 10 summarizes the particulate matter emissions measurements from the Wright Patterson experiments. These data are plotted in Figure 21. There were large reductions in PM mass emissions when operating the engine with FT versus JP8 fuel, as has been measured previously with a T-63 engine [44]. Total PM mass emissions were reduced by more than 60% in switching from JP8 to FT fuel. For the 50/50 blend, the PM mass emissions were slightly less than the arithmetic mean of the PM emissions when the engine was operated on the neat fuels. Therefore the changes are almost linear with blend ratio, which is similar to the results of Corporan et al. [44]. At cruise load we measure ~ 80% reduction of PM mass emissions in using FT over JP8 fuel, a bit less than the 95% reduction reported by Corporan et al. [44]. No blend experiments were performed at the cruise load.

Figure 21 indicates that the PM emissions are dominated by organic (OC) and elemental (EC). The relative contributions of OC and EC to PM mass varied significantly with both load and fuel composition. Similar to the Pittsburgh data, the idle emissions were dominated by OC while the cruise emissions were dominated by EC. On an absolute basis, the EC emissions were higher at high load (cruise) than at low load (idle). There are also significant fuel composition effects. At a given load, both the OC and EC emissions were higher when the engine was operated JP8 versus FT. For example, at idle EC emissions are ~ 1 % of the total PM emissions when the engine was operated on FT versus 15% when the engine was operated on JP8. We attribute the different EC emissions to the higher aromatic content of the JP8 fuel; aromatics have a higher propensity to soot.

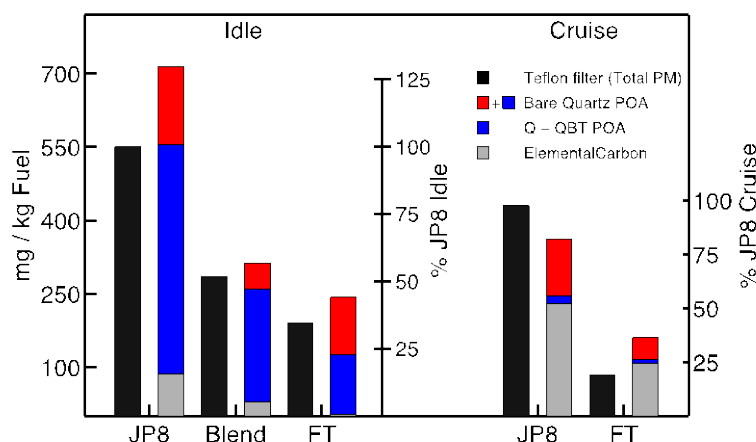


Figure 21. Total PM emissions from Teflon filter weights (black), bare quartz filter EC (gray), bare quartz filter OC (blue), and QBT estimate of bare quartz filter artifact. Samples for JP8, a 50/50 JP8/FT Blend, and neat FT fuel emissions taken at idle load are on the left. Samples for JP8 and neat FT taken at cruise load are on the right.

Figure 21 also shows artifact corrected estimates of the OC emissions ($Q - QBT$). At cruise, the Q and QBT filters collected essentially the same amount of OC, suggesting essentially no particulate OC. At idle, the fraction of OC collected on the QBT filter (artifact) was much smaller than at cruise. The largest artifact at idle was measured when operating the engine on neat FT, approximately 50% of the bare Q OC.

OC Speciation

The PM collected on the quartz filters during the Wright Patterson experiments with the T63 engine was analyzed using GC-MS to determine the specific chemical makeup of the OC fraction. The results from the speciated emissions are summarized in Table A4. Fuel and oil samples were also analyzed to provide a reference to help interpret the emissions data. Less than 15% of the OC collected on a quartz filter could be specifically related to known compounds at idle load. Roughly half of the speciated compounds were n-alkanes and the remainder consisted of PAH, alkylated naphthalenes, and cycloalkanes with long-chain substituents. The emission factors for these speciated compounds are listed in Appendix A.

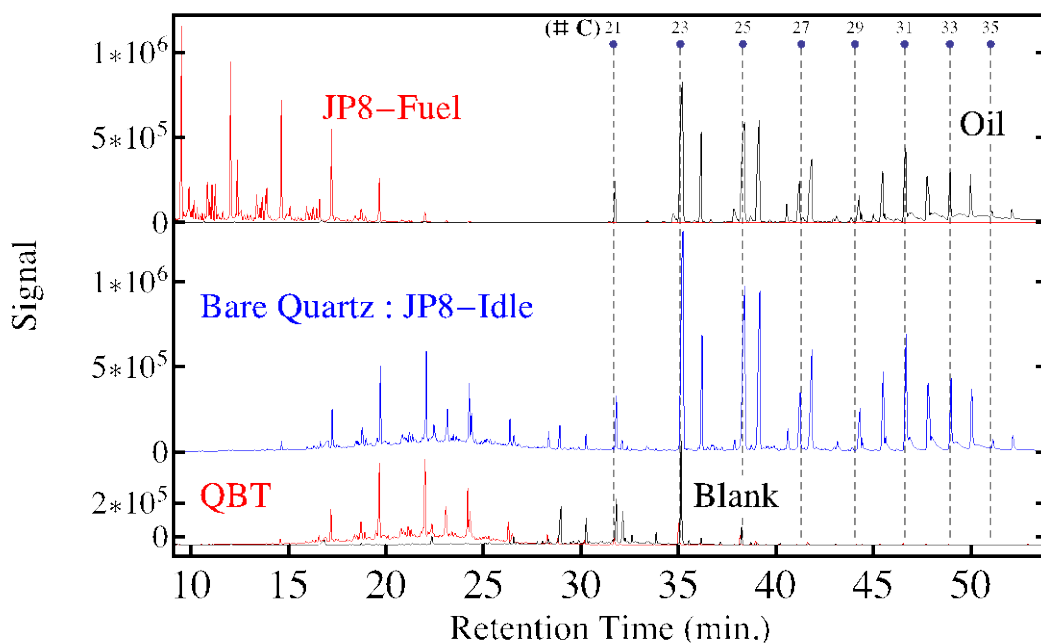


Figure 22. Select ion chromatogram of m/z 57 from a bare quartz filter at idle load with JP8 fuel. Several n-alkane retention times are marked with blue points and vertical, gray dashed lines. The engine oil and fuel data are shown on top panel (red and black, respectively). The quartz behind Teflon (QBT) and blank data are shown in bottom panel (red and black lines, respectively).

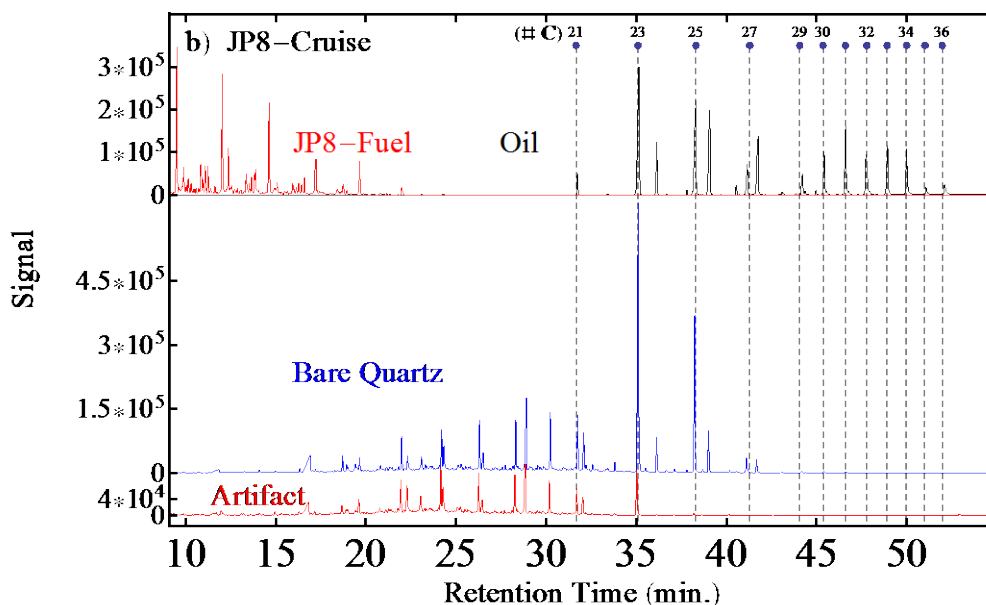


Figure 23. Chromatogram of m/z 57 from a cruise load experiment with JP8 fuel. Several n-alkane retention times are marked with blue points and vertical, gray dashed lines. In top panel, m/z 57 chromatograms for engine oil and fuel are shown. The bottom panel shows data for the quartz behind Teflon filter (QBT, artifact).

Although only a small fraction of the OC mass can be attributed to individual compounds, both the mass spectra and selected ion chromatograms clearly that a large fraction of the OC mass is likely engine oil, especially at idle. In Figures 22 and 23 the m/z 57 chromatogram is shown for the idle and cruise emissions, respectively. The m/z 57 chromatograms for the QBT filter and the bare quartz filters are strongly correlated at elution times less than about 35 minutes. This indicates that a large component of the artifact is IVOC vapors (hydrocarbons smaller than about C_{20}).

Figure 22 shows that, at idle, the emissions and oil m/z 57 chromatograms are strongly correlated for retention times greater than about 35 minutes. Therefore, lubricating oil appears to contribute a large fraction of the OC in the idle emissions. In comparison, the JP8-cruise data shown in Figure 23 indicates that only emissions contain only the first several peaks of the oil chromatogram, and hence does not contain intact oil.

To further investigate the source of the PM at idle loads as engine oil, we also examined the average mass spectra for the PM material eluting after 34 minutes in the GC-MS. While the m/z 57 chromatograms shown in Figures 22 and 23 target hydrocarbons, the total mass spectra better represent the full range of chemical composition of material passing through the GC column.

Figure 24 plots the cumulative mass spectra for idle samples collected while operating the engine on all three fuels and engine oil. In a cumulative mass spectrum, sharp increases indicate a prominent mass fragment. We focus on the cumulate mass

spectra of all of the material that eluted between 31-53 minutes, which corresponds when the bulk of the oil elutes. In addition, the cumulative mass spectra at 39 and 50 minutes are also shown.

Over this range of elution times (31 – 53 minutes), the idle samples at all three loads have a very similar mass spectrum to oil. This suggests that the OC fraction of the PM emissions (or at least the fraction that elutes from the GC column) has a similar chemical composition to oil. Furthermore, the OC fractions of the PM samples all have similar mass spectra across the range of non-artifact retention times.

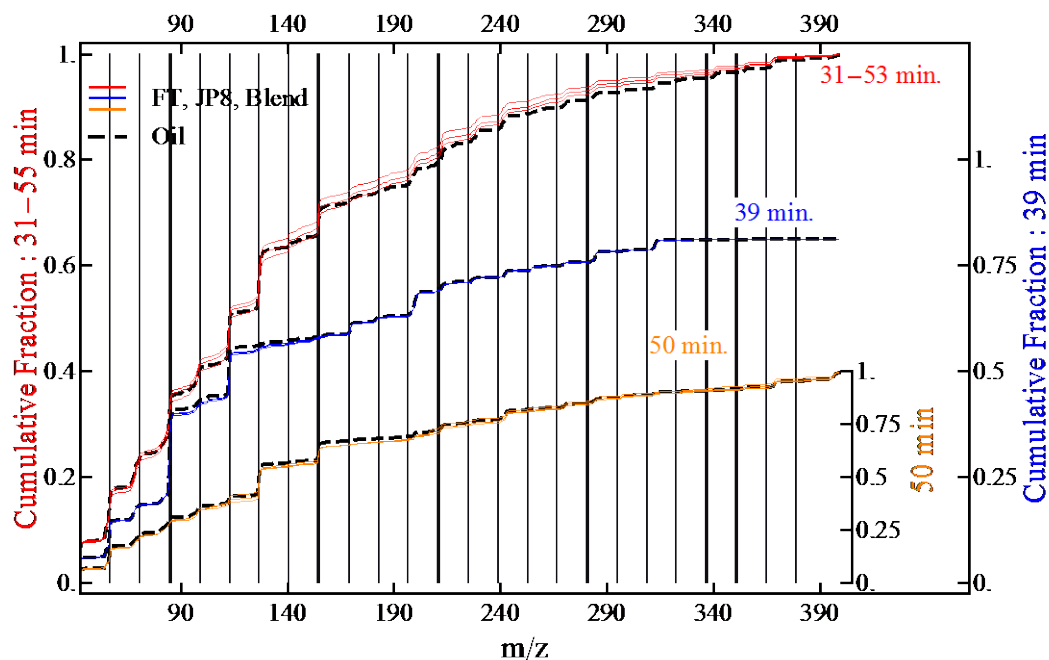


Figure 24. Cumulative mass spectra for OC from JP8, a 50/50 blend of JP8/FT, and neat FT at idle load. Cumulative mass spectra are also shown for the engine oil (black). The cumulative mass spectra are average over 3 time ranges in their respective gas-chromatograms. The first range is 31-53 min. and includes the full range of elution times for the engine oil (red). The second time range covers a peak at approximately 41 min. (blue), and the third range roughly centered at 50 minutes (orange). The corresponding cumulative mass spectrum for the oil is shown as a dashed, black line for all time ranges. Highly oxidized OC likely does not elute from the capillary column used in the GC.

Organic Aerosol Volatility

Figure 25 plots thermograms of the POA emissions. At idle load, a very large fraction of the POA evaporate at low temperature with a T_{50} (temperature at which 50% of the POA emissions evaporate) of less than 40°C. This was observed for all three fuels (neat JP8, neat FT, and blend). Therefore the idle emissions are clearly semivolatile and their gas-particle partitioning will vary with atmospheric conditions (temperature and

organic aerosol concentration). The idle POA emissions for the T63 are much more volatile than those of the CFM56 engine tested at the Pittsburgh International Airport. In comparison, the POA emissions at cruise were much less volatile, with only about 20% evaporating at 80 °C. This may be due to very low OC content of the cruise emissions (Figure 21).

The GC-MS analysis also indicates that a large fraction of the POA emissions are semivolatile. The elution time from the GC provides an estimate of the volatility of the material [82, 83]. A number of selected ion chromatograms were used to determine the fraction of material in the SVOC range, including m/z 41, 55, 57, 68, 85, 97, 113, and 129. The fraction of the signal area between 34.5 and 48.5 minutes, with artifact and blank correction, was taken as the fraction of SVOC material. This time interval was defined based on the elution times of semivolatile *n*-alkanes. At idle, SVOCs contributed about 90% of the total, artifact corrected POA that eluted from the GC. The remaining 10%, eluting between 48.5 and 58 minutes, is the less volatile, low-volatility organic compounds (LVOC). In comparison, about 83% of the engine oil is SVOC with the balance (17%) being lower volatility compounds. At cruise load POA emissions elute from the GC appear to be nearly completely SVOC, with an averages $\geq 94\%$ SVOC. Although the cruise results might seem to contradict the relatively non-volatile thermograms shown in Figure 25, only a fraction of the POA elutes through the GC.

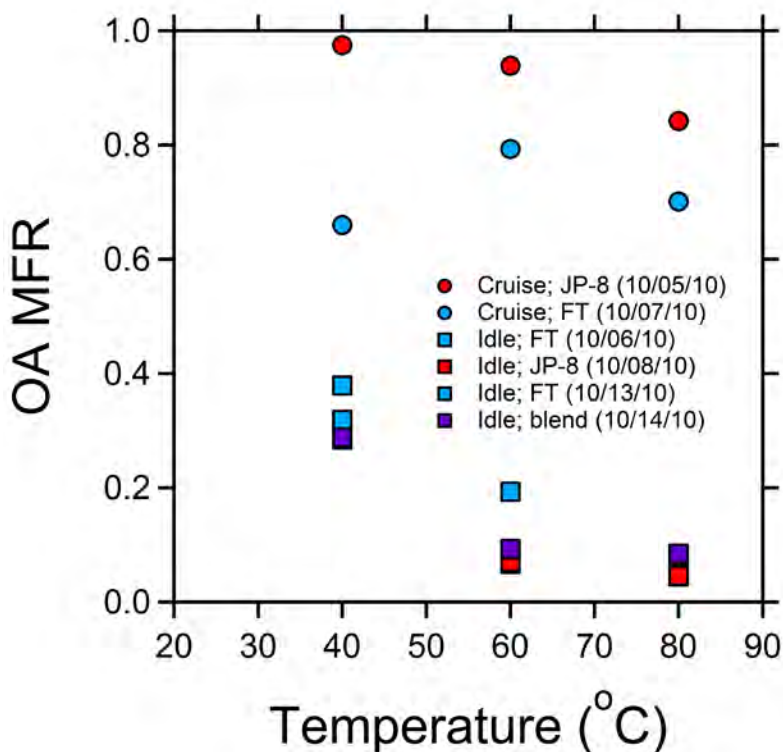


Figure 25. Thermodenuder measurements of fresh primary organic aerosol volatility from the Wright Patterson tests with the T-63 engine. OA MFR – organic aerosol mass fraction remaining.

Photo-oxidation and secondary aerosol production

After characterizing the primary emissions, the emissions were aged in the smog chamber. Figure 26 plots time-series of gas- and particle-phase concentrations measured in the chamber during idle and cruise load experiments when the engine was operated on neat JP-8. The other aging experiments demonstrated similar behavior to those shown in Figure 26.

Each experiment can be divided into four different periods: (I) bag filling during which exhaust was added to the chamber, (II) primary emission characterization during which chamber contents were characterized in the dark, (III) photo-oxidation during which the chamber was exposed to sunlight or artificial UV light, and (IV) aged emission characterization during which aged chamber contents were characterized in the dark. Vertical grey bars in each panel indicate the filling periods.

During the chamber filling period, concentrations of primary gas-phase species (CO_2 and single-ring aromatics (e.g. toluene)) increased. Initial toluene concentrations were around 11 ppbv and 2.2 ppbv for the idle and cruise load experiments, respectively. These concentrations are not unreasonable for typical atmospheric concentrations. Measured concentrations of SMPS volume also increased when exhaust was injected into the chamber (vertical grey bars), as shown in Figures 26c and 26f. The initial particle size in the chamber was approximately 50 nm at idle load and 90 nm at cruise load. The mass median diameter increases as particles quickly coagulate during the filling and primary characterization periods.

During the primary characterization period, there are no measured changes in gas-phase emissions. The measured aerosol mass decreased, as particles were lost to the chamber walls. We fit the decay of particle mass during the primary characterization to determine a first-order wall-loss rate constant to correct the data for wall losses. Coagulation causes the mass median diameter to grow to 85 nm and to about 120 nm by the end of the primary characterization period for the idle and cruise load experiments, respectively.

Photo-oxidation results in substantial changes in gas- and particle-phase concentrations in the chamber. During the idle load experiment, photo-oxidation produced about 35 ppbv of ozone, while for the cruise load experiment there was no measured ozone formation because of the much higher NO_x levels. Concentrations of single-ring aromatic compounds decrease due to reaction with OH and concentrations of oxygenated organics such as acetaldehyde increased.

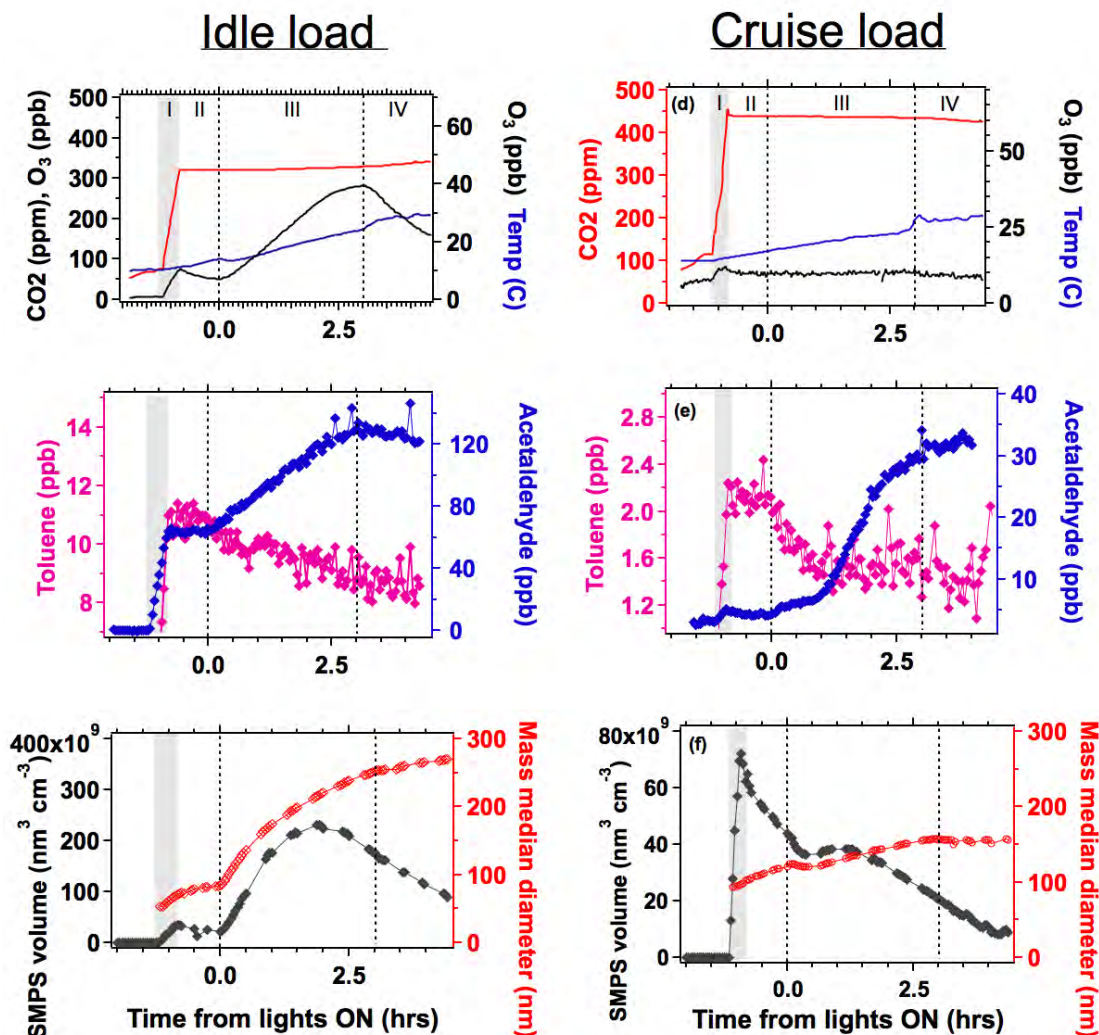


Figure 26. Time-series of evolution of gas- and particle-phase compounds for typical photo-oxidation experiments at idle and cruise loads. Data are shown for idle load (expt #2) and cruise load (expt #4). (a,d) CO₂, ozone, and chamber temperature, (b,e) Concentrations of toluene and acetaldehyde (note scale is not to zero for left axis), (c,f) SMPS total volume and mass median diameter concentrations. Only undened data is shown. Vertical grey bars indicate chamber filling period.

After the UV lights were turned on ($t = 0$ hrs), total particle volume inside the chamber increased dramatically for the idle load experiment (Figure 26c), increasing by a factor of 10 after two hours of oxidation. This increase indicates substantial production of secondary PM mass. For the cruise experiment, initiating photo-oxidation creates a more modest increase in the particle volume. Photo-oxidation results in the growth of the particle mass median diameter (MMD) from 85 to 280 nm for the idle experiment. For the cruise load, there was less change in the size distribution of the particles, with the MMD growing from 120 to 150 nm after several hours of oxidation. Unlike in the Pittsburgh experiments, nucleation was not observed in any of the Wright Patterson experiments. The increase in wall-loss corrected particle mass in the chamber mirrors the

decay of single-ring aromatics such as toluene. These aromatics are important SOA precursors [89]; their decay also provides a generic indicator of photo-oxidation.

CO₂ concentrations in the chamber slightly increased over the course of photo-oxidation due to leakage of air into of the chamber. Gas- and particle-phase pollutant concentrations were corrected for this dilution. After addition of exhaust, the initial temperature of the chamber was 14.2 ± 2.3 °C and the relative humidity was than 20%, across the entire set of experiments. The chamber temperature increased throughout the oxidation phase of the experiment as the ambient temperature increased (chamber experiments were started first thing in the morning). The temperature in the chamber increased, on average, by 11.6 °C during photo-oxidation. This increase in temperature will modestly shift the gas-particle partitioning of semivolatile material towards the vapor phase, reducing the amount of SOA.

The results shown in Figures 26d-26f are from an experiment in which HONO was added to the chamber as an additional OH source. In the one other JP8 cruise experiment, there was no secondary PM formation (Table 11). However, in this experiment there was also no measured decay of VOC suggesting no photo-oxidation.

A summary of the results from the photo-oxidation experiments is presented in Table 11. Initial VOC/NO_x ratios were calculated for each experiment based on reported NO_x emission factors for the T63 engine used in these experiments [44]. The idle load experiments are low-NO_x while the cruise load experiments are considered high-NO_x, reflecting the trends in VOC and NO_x emissions with engine load. The addition of HONO shifted the VOC/NO_x ratio toward even higher NO_x conditions compared to those at the engine outlet. To quantify the relative importance of secondary PM production, the ratio of the secondary-to-primary PM is given for each experiment.

Table 11. Results for photo-oxidation experiments conducted at Wright Patterson.

| | | | | | | After 3 hrs of oxidation | | |
|--------|--------|--------|--------------|-------------------------------------|----------------------------|------------------------------|-------------------------------|--|
| Expt # | Fuel | Load | Light source | VOC/NO _x (ppbC / ppb) | Primary PM (mg/kg-fuel) | Secondary PM (mg/kg-fuel) | Primary-to-Secondary ratio | OH exposure molecules cm ⁻³ hr |
| 1 | JP-8 | Idle | UV lights | chamber shakedown | | | | |
| 2 | JP-8 | Idle | Sunlight | 13.5 | 170 | 7200 | 42 ± 30 | 1.1 x 10 ⁷ |
| 3 | JP-8 | Cruise | UV lights | 0.14 | 25 | 0 | - | * |
| 4 | JP-8 * | Cruise | Sunlight | 0.2 | 510 | 1100 | 2.1 ± 1.4 | 5.0 x 10 ⁶ |
| 5 | Blend | Idle | Sunlight | 18 | 73 | 2700 | 37 ± 16 | 6.5 x 10 ⁶ |
| 6 | FT | Idle | Sunlight | 13 | 75 | 330 | 3.0 ±1.3 | 8.0 x 10 ⁶ |
| 7 | FT | Idle | Sunlight | 11 | 37 | 130 | 3.4 ±2 | 8.6 x 10 ⁶ |
| 8 | FT | Cruise | Sunlight | 0.07 | 68 | 0 | - | 1.6 x 10 ⁷ |

* HONO was added to the chamber as an additional OH source

Figure 27 plots primary PM, EC measured during the primary characterization period, secondary sulfate, and SOA measured after three hours of photo-oxidation. The primary and secondary PM estimates are determined from subtracting EC measurements for each experiment from the total SMPS volume, assuming a constant density of 1.0 g/cm^3 for OA and 2.0 g/cm^3 for EC. Estimates of secondary sulfate were derived from an average of AMS, SO_2 monitor, and filter measurements.

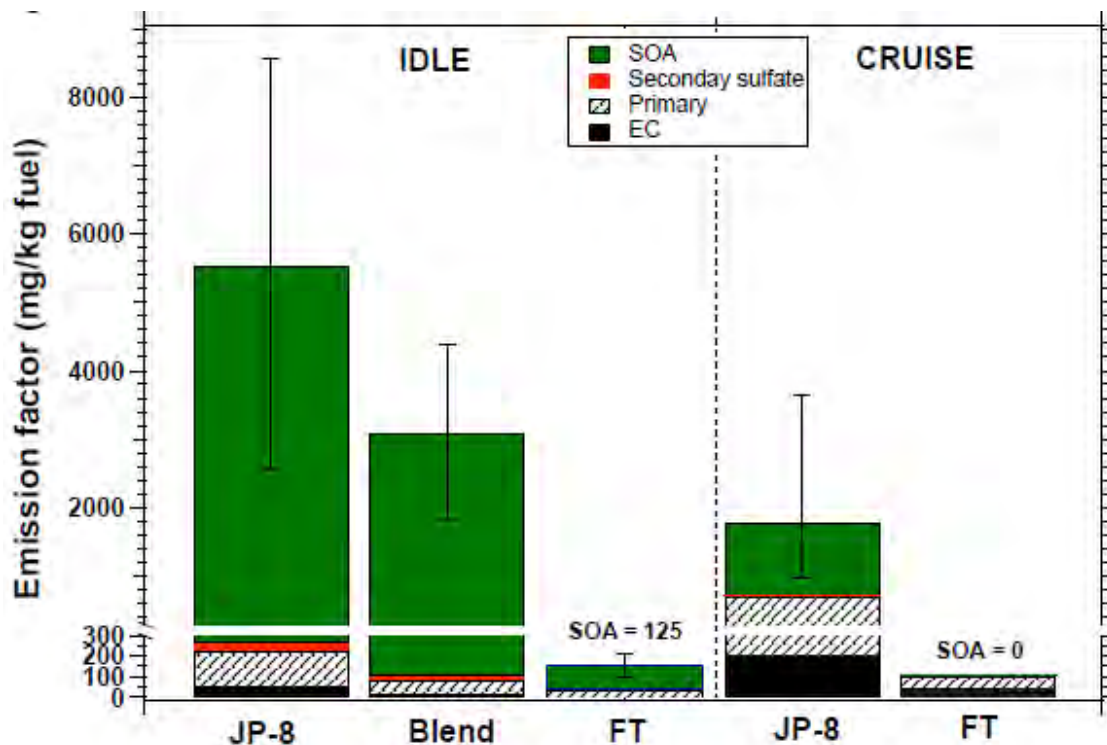


Figure 27. Primary and secondary PM mass based on estimates from SMPS volume and EC measurements as described in the text. Uncertainty bars indicate uncertainty in assumptions for wall loss corrected (mainly due to loss of vapors). Secondary PM is shown after 3 hours of oxidation.

Error bars indicate uncertainty with the wall-loss correction, which is mainly due to uncertainty in losses of condensable vapors. The particle mass wall loss rate inferred from the BC measurements and measured during the primary characterization period generally agreed to within 5%.

At idle load, photo-oxidation produced substantial SOA for all three fuels (relative to the primary emissions). On a fuel basis, secondary PM formation was higher at idle load compared to cruise load. After three hours of photo-oxidation, about five times more SOA was produced at idle ($\sim 7200 \text{ mg/kg fuel}$) compared to cruise load ($\sim 1100 \text{ mg/kg fuel}$) for the neat JP-8 experiment. For experiments with neat FT, no SOA was formed at cruise load versus 125 mg/kg fuel at idle load. For experiments at idle load, the relative importance of secondary PM is much greater compared to primary PM. This result

agrees with the Pittsburgh results, where emissions of secondary aerosol were higher at 4% load (ground-idle) compared to 85% load (take-off).

The use of neat FT fuel reduced the formation of SOA by about a factor of 40 at idle (there was not measured SOA production at cruise load with FT fuel). The use of the blend 50:50 fuel also reduces formation of secondary aerosol at idle load. Compared to the use of neat JP-8, the blend fuel reduces secondary formation by a factor of 3.

In order to compare formation of secondary PM across different experiments, one must account for differences various experimental conditions such as hydroxyl radical (OH) concentrations, NO_x levels, and partitioning effects. Table 11 lists average OH exposure for each experiment. Figure 28 plots secondary PM formation as a function of OH exposure for the idle load experiments with the JP-8, JP-8/FT blend, and FT fuels. The ranges of estimates shown were estimated based on uncertainty with the wall-loss correction and data obtained for duplicate experiments (FT idle experiments).

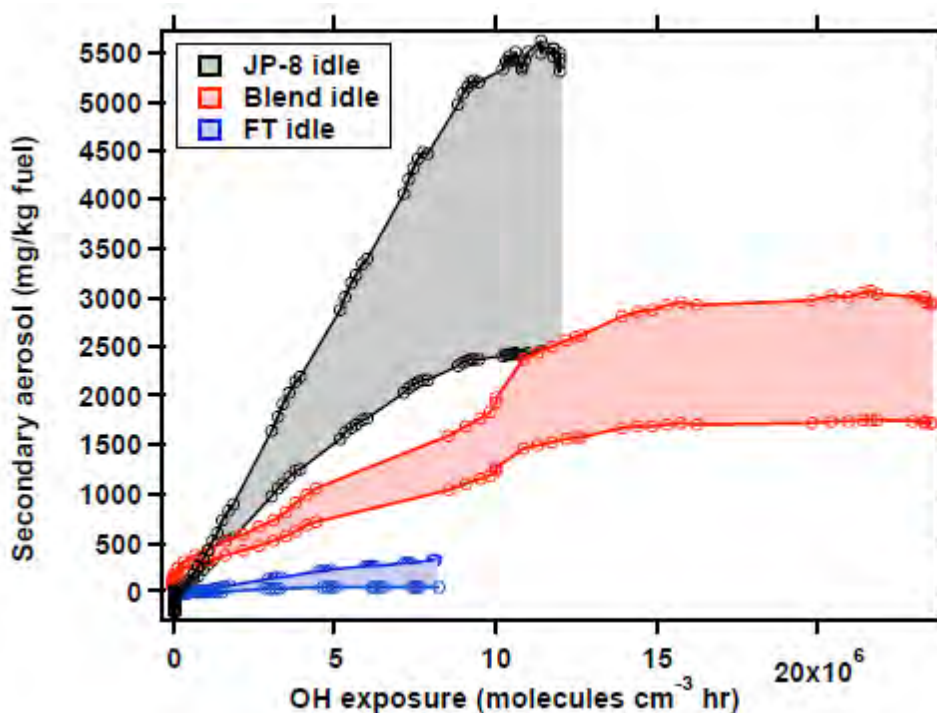


Figure 28. Secondary aerosol formation for experiments performed at idle load with JP-8, blend of JP-8/FT, and FT fuels plotted as a function of OH exposure. The ranges of estimates shown are based on uncertainty in wall-loss corrections and data for duplicate experiments.

Figure 28 also compares SOA formation on atmospheric time scales. This figure indicates that the conclusion that the use of neat FT fuel dramatically reduced the secondary PM formation compared to use of neat JP-8 fuel is robust after controlling for OH exposure. The wide range of uncertainty in the JP-8 idle experiments (due to the

wall-loss corrections) complicates the comparisons between the blend and JP-8 idle experiments.

Figure 28 suggests that the 50/50% blend fuel does not translate into a 50% reduction in secondary aerosol formed at idle load compared to JP8. However, one must also account for the effects of gas-particle partitioning. Essentially the SOA formed from the JP8 component of the blend increases the OA concentration in the chamber, shifting the gas-particle partitioning of FT SOA towards the condensed phase, increasing the yield. After correcting for partitioning, we believe that blends with FT with the blend fuel. This issue is discussed in more detail in the modeling section.

Aged Aerosol Composition

The chemical composition of the non-refractory particle mass was measured with the AMS (except for expt. #3) and with filter samples. However, the AMS data from the primary aerosol characterization and initial photo-oxidation periods are complicated by the small particle size. The aerodynamic lens on the AMS only transmits particle between approximately 70-800 nm at 100% efficiency [90]. As shown in Figure 26, the median size of the particles was less than 100 nm until after photo-oxidation was initiated; therefore, during the primary characterization period of the experiment the AMS only samples a fraction of the aerosol mass. The small size of the particles also introduces significant uncertainty in the calculation of the POA emission factor in the chamber, especially in the idle load experiments when the initial particle size is smaller than at cruise load. As the particles grow into the size window of the AMS during the photo-oxidation phase of the experiment, it is possible to quantify the composition of the aerosols.

Both the filter and AMS data indicate that the secondary PM is dominated by organics in every experiment. The highest contribution for inorganics was measured for the JP-8 idle experiment (expt #2) for which ~3% of the total secondary PM was inorganic. For experiments performed with FT fuel, no secondary sulfate was observed, consistent with the negligible sulfur content of that fuel. The secondary sulfate measured with the AMS agreed well with the measured decay of SO₂. Ion-chromatography of filter samples also indicates little contribution from inorganic species, such as sulfate, after several hours of photo-oxidation.

There were significant changes in the chemical composition of the OA as measured by the AMS in every experiment. Figure 29 shows the time evolution of the AMS mass fragment m/z 44 for the idle and cruise load experiments. The AMS signal at m/z 44 (mainly CO₂⁺) is a widely used marker for the extent of oxygenation in organic aerosol [86]. Data for the idle load experiments show an increase in the aerosol oxidation at the onset of photo-oxidation. The data at idle load for the JP-8 and FT experiments show similar behavior; a significant change in organic aerosol oxidation during the first hour of oxidation due to SOA production, with the contribution of m/z 44 increasing from approximately 2 to 5%. Results for the blend experiment show a smaller increase in the aerosol oxidation at the onset of photo-oxidation, with the contribution of m/z 44 increasing from approximately 1 to 2.6%. After the initial stages of photo-oxidation, subsequent changes in m/z 44 show a more gradual increase.

Due to low concentrations of primary OA in the cruise load experiments, data were averaged to reduce noise. At the start of photo-oxidation, the cruise load data show a gradual increase in the contribution of m/z 44 (Figure 29b). For the JP-8 cruise experiment, the contribution from m/z 44 increases from 4-8%, and in the FT cruise experiment from 6-10%. This difference between the idle and cruise experiments is most likely due to the SOA rapidly overwhelming the POA in the idle experiments, whereas POA contributes a larger fraction of the OA in the cruise experiments. It is interesting to note that although no SOA was formed in the FT cruise experiment, we still see significant chemical transformation of the OA. The organic aerosol (both POA and SOA) is more oxygenated in the cruise load experiments.

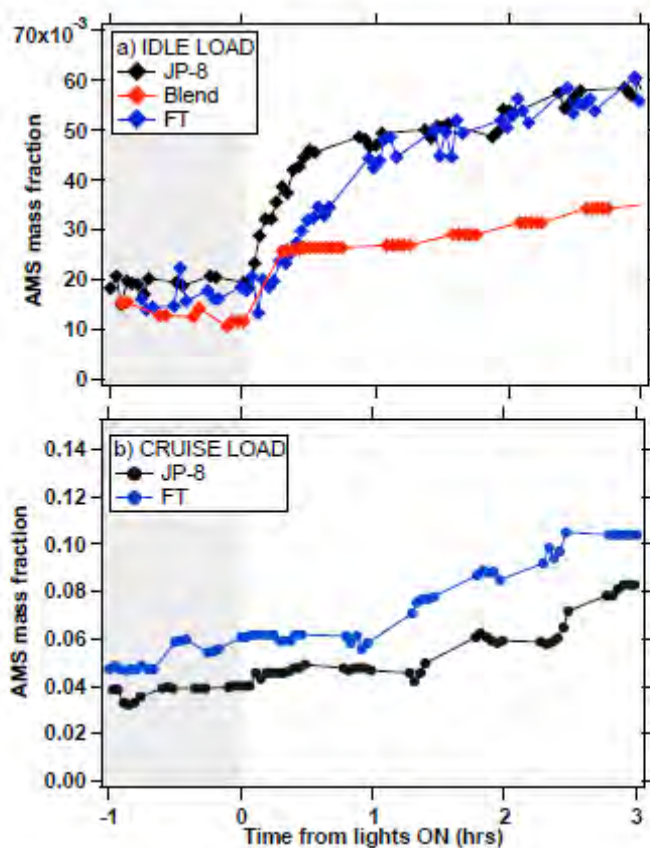


Figure 29. Change in aerosol composition as measured by the AMS. Change in mass fraction m/z 44 for (a) idle and (b) cruise loads. Note the difference in vertical scales for the two panels.

AAFEX Tests

The analysis of the AAFEX samples focused on GC-MS analysis of low volatility organics collected on quartz filter and Tenax sorbet tubes. These data are summarized in Table 12, which presents volatility distributions for JP8 experiments. It also compares the AAFEX and Pittsburgh data. Both experiments used CFM56 engines and therefore

this comparison provides insight into the variability of low volatility organic emissions and potential representativeness of the Pittsburgh experiments.

Low volatility organic emissions collected from the CFM-56 engines used at the AAFEX and PIT studies appear to be quite similar. In both studies, these emissions were highest at low load and fell with increasing load. At idle load (4-7%), IVOCs dominate the low-volatility organic emissions. For both AAFEX and PIT, IVOCs constituted >90% of the low volatility organic emissions at idle load. The idle emissions from both engines were similar in magnitude and distribution. The total emissions of low volatility organics at ground idle from the PIT engine were approximately double than those measured at AAFEX. However, this difference is likely the result of combining 4% and 7% operation emissions into a single integrated sample at AAFEX, whereas the PIT sample was collected at 4% load. The PIT data shows large reductions in IVOC emissions when the engine load is increased from 4% to 7% (similar to other VOCs). The volatility distributions at idle load measured at AAFEX and PIT are quite similar (Figure 30), with the largest fraction of the low volatility organic emissions in the $10^6 \mu\text{g m}^{-3}$ bin. The AAFEX samples have slightly more mass in the SVOC bins than the PIT samples. This may be indicative of higher oil emissions from this engine.

The emissions from the two engines were also similar at take-off rated thrust. The total emissions of low-volatility organics were similar: 48 mg/kg-fuel for AAFEX and 57 mg/kg-fuel for PIT. The volatility distributions are also similar. Unlike the idle emissions, IVOCs do not dominate and the $10^6 \mu\text{g m}^{-3}$ bin is not the most abundant, consistent with more efficient combustion and less emission of unburned fuel at higher load. The PIT engine has higher IVOC emissions than AAFEX, and this may be the result of differences between the two engines. As with idle operation, the AAFEX samples have slightly more mass in the SVOC bins.

Table 12. Pittsburgh and AAFEX emissions of low volatility organics. AAFEX data are for engine operating on JP8 fuel.

| C* bin ($\mu\text{g m}^{-3}$) | Pittsburgh Tests | | | | AAFEX Tests | |
|------------------------------------|--|-------|-------|-------|-------------|---------|
| | 4% | 7% | 30% | 85% | 4-7% | 85-100% |
| | <u>Mass Fractions</u> | | | | | |
| 10^6 | 0.912 | 0.070 | 0.259 | 0.197 | 0.826 | 0.095 |
| 10^5 | 0.050 | 0.061 | 0.052 | 0.103 | 0.096 | 0.099 |
| 10^4 | 0.016 | 0.510 | 0.135 | 0.146 | 0.019 | 0.189 |
| 10^3 | 0.007 | 0.284 | 0.212 | 0.234 | 0.009 | 0.176 |
| 10^2 | 0.003 | 0.042 | 0.091 | 0.085 | 0.009 | 0.120 |
| 10^1 | 0.003 | 0.019 | 0.091 | 0.078 | 0.017 | 0.116 |
| 10^0 | 0.004 | 0.006 | 0.061 | 0.066 | 0.012 | 0.103 |
| 10^{-1} | 0.003 | 0.005 | 0.057 | 0.055 | 0.007 | 0.078 |
| 10^{-2} | 0.003 | 0.003 | 0.042 | 0.036 | 0.004 | 0.024 |
| | <u>Total Emission Factor (mg kg-fuel)*</u> | | | | | |
| | 1600 | 559 | 77.2 | 57.2 | 709 | 48 |

*Sum of emissions in all volatility basis set bins.

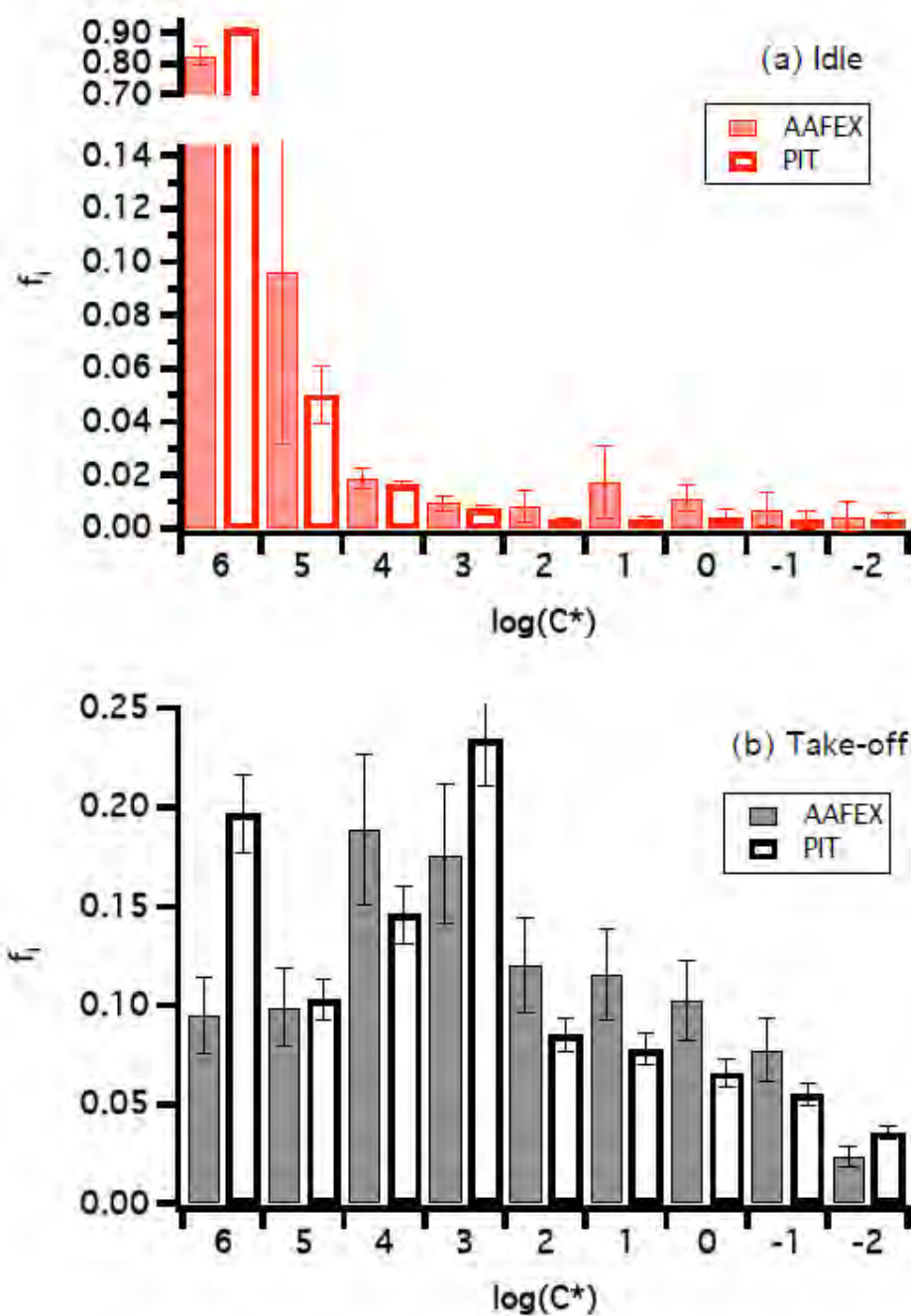


Figure 30. Comparison of volatility distributions measured during Pittsburgh and AAFEX tests: (a) idle and (b) take-off rate thrust.

Modeling

In this section, we compare predictions of the traditional SOA model to smog chamber data from the two major field campaigns. We also develop parameterizations for non-traditional SOA using the VBS approach. We use the following mnemonic to refer to the different experiments: PIT = Pittsburgh (CFM56) data; WPA = Wright

Patterson (T63) data; JP8 = standard jet fuel; FT = Fischer Tropsch fuel; idle = (4% load experiment at PIT, idle experiment at WPAT); Taxi = (7% load experiment at PIT); Takeoff = (85% load for PIT); and cruise = (cruise experiment at WPAT). Therefore, PIT-JP8-Taxi = CFM56 operated on JP8 and 7% load.

Input Data

SOA models require comprehensive data on gas-phase organic emissions. Table 13 compiles VOC and POC emissions data for each experimental condition. As described in previous sections of this report, the VOC emissions were characterized by collecting samples in SUMMA canisters and analyzing them using a GC-MS. For the PIT-JP8-Taxi experiments, only a small number of VOCs were measured and therefore we estimated VOC emissions using results from the APEX study, which characterized the VOC emissions from a CFM56-2B engine on a DC-8 [91]. The APEX study reported that the VOC emissions at taxi (7% load) are about 40% of the VOC emissions at ground idle (4%). Therefore, we estimated VOC emissions at taxi by multiplying VOC emissions at idle by 0.4.

Low-volatility organics (POC) were characterized by analyzing quartz filter and Tenax TA sorbent tube samples. The POC emissions are the sum of all the organic emissions that have a C^* lower than $10^6 \mu\text{g m}^{-3}$; we refer to these emissions as primary organic carbon (POC). We assume that organic emissions with C^* higher than $10^6 \mu\text{g m}^{-3}$ are explicitly accounted as VOC species. Only a small fraction of the POC emissions could be quantified on a compound-by-compound basis (Figure 14). To estimate the total mass of POC emissions, we developed a calibration curve for the unresolved complex mixture (UCM) using fuel and lubricating oil used by the aircraft and then distributed those emissions into the VBS based on the GC elution time.

For the SOA modeling, we assume that the oxidation chemistry in the smog chamber is driven by the hydroxyl radical (OH). OH concentrations were not directly measured but inferred from the measured decay of various organic (e.g. toluene) and inorganic (e.g. SO_2) species. Figure 31 plots the median OH exposure (orange cross) with the standard error of the mean (green bars) for each experiment. The label “N=x” denotes the number of compounds included in the analysis in particular experiment. The “N>1” experiments represent data where multiple organic species were used while the “N=1” experiments represent data where only SO_2 was used.

Figure 31 indicates that the amount of OH exposure varied widely across the set of experiments from 0.4 to 5×10^7 molecules hr cm^{-3} (median value of 1×10^7 molecules hr cm^{-3}). This corresponds to 2 to 25 hours photochemical aging assuming a typical daily average OH concentration of 2×10^6 molecules cm^{-3} .

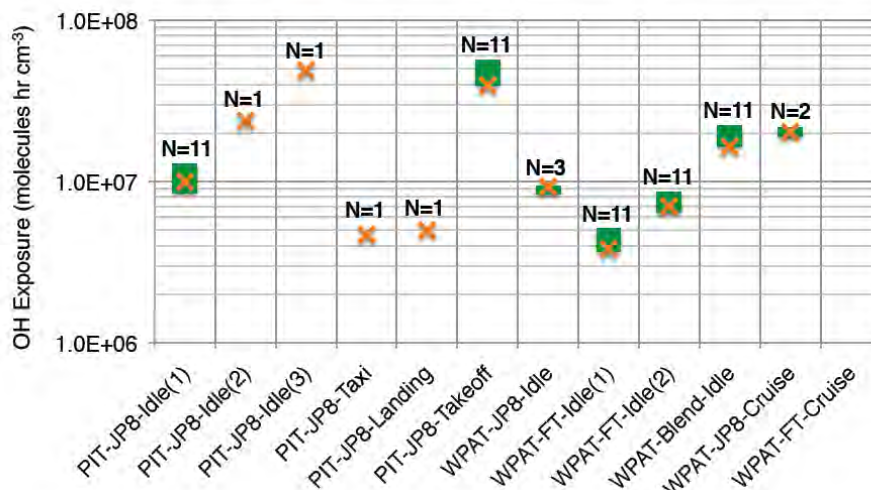


Figure 31. Estimated OH exposure for the twelve different experiments used for the SOA modeling. The median value represented using the orange cross is what is used in our analysis; green bars indicate standard error of the mean.

We assume that ozone produced as a result of the VOC-NO_x chemistry does not significantly contribute to the formation of additional SOA since alkanes and aromatics have a very low reactivity with ozone while alkenes form relatively little SOA from ozone photochemistry.

Before describing the results from the SOA modeling, we compare the measured SOA mass to the measured precursor mass. Figure 32 plots the measured SOA and its precursors – POC and VOC – for the different experiments. POC is split into SVOC and IVOC. The VOCs are further split into VOCs that according to Murphy and Pandis [62] form SOA (VOC(SOA)) and those that do not (acetylene, ethane, ethene, propane, propene, propyne and butene; VOC(no SOA)). Except for the WPAT-JP8-Cruise experiment, the measured SOA is smaller than the sum of the precursors (POC + VOC(SOA)). The POC emissions are lower but still comparable to the VOC(SOA) emissions and therefore likely to be at least as important. Most of the POC emissions are IVOCs while a large fraction of the VOCs are too small to form SOA. The eventual amount of SOA formed is a competition between the higher emissions but lower SOA-potential of VOCs and the lower emissions but higher SOA-potential of POCs. Both the SOA formation and precursor emissions decrease with increasing engine load, i.e. idle to takeoff for the CFM56 tests and idle to cruise for the T63 tests.

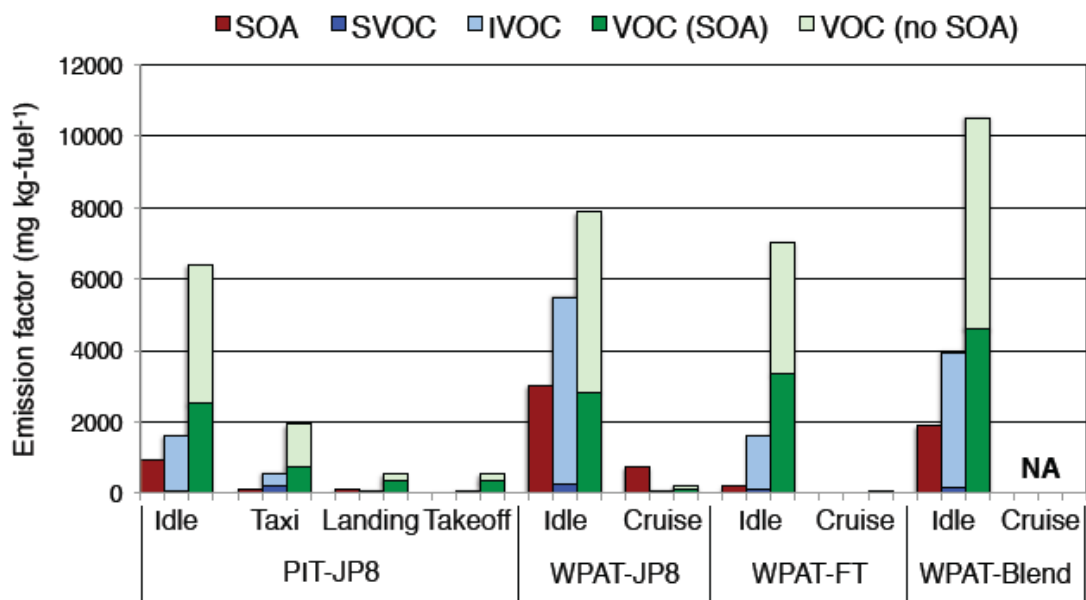


Figure 32. Comparison SOA formed to emissions of SOA precursor emissions: POC (SVOC and IVOC) and VOC (SOA and no-SOA forming).

Table 13. SOA precursor emissions (mg kg-fuel⁻¹) used in the SOA modeling.

| | PIT-JP8 | | | | WPAT-JP8 | | WPAT-FT | | WPAT-Blend | |
|----------------------------|---------|------|---------|---------|----------|--------|---------|--------|------------|--------|
| | Idle | Taxi | Landing | Takeoff | Idle | Cruise | Idle | Cruise | Idle | Cruise |
| VOCs | | | | | | | | | | |
| 1-butene | 194.6 | 58.4 | 2.2 | 2.2 | 388.6 | 1.2 | 155.2 | 1.4 | 379.3 | - |
| 1-heptene | 61.5 | 18.5 | - | - | 0.1 | 0.0 | 6.2 | 0.0 | 15.0 | - |
| 1-hexene | 81.1 | 24.3 | - | - | - | - | - | - | - | - |
| 1-methylcyclohexene | 5.2 | 1.6 | - | - | - | - | - | - | - | - |
| 1-octene | 5.9 | 1.8 | 1.2 | 1.2 | - | - | - | - | - | - |
| 1-pentene | 91.2 | 27.4 | 10.8 | 10.8 | 79.2 | 0.0 | 67.8 | 0.0 | 0.0 | - |
| 1,2-butadiene | 6.4 | 1.9 | - | - | 1.4 | 0.0 | 4.8 | 0.0 | 4.7 | - |
| 1,2-diethylbenzene | 10.9 | 3.3 | 1.9 | 1.9 | - | - | - | - | - | - |
| 1,2,3-trimethylbenzene | 47.0 | 14.1 | 1.7 | 1.7 | 4.1 | 0.0 | 10.5 | 0.0 | 42.4 | - |
| 1,2,4-trimethylbenzene | 41.9 | 12.6 | 7.4 | 7.4 | 24.1 | 0.0 | 29.7 | 0.0 | 155.3 | - |
| 1,2,4,5-tetramethylbenzene | 27.2 | 8.2 | - | - | - | - | - | - | - | - |
| 1,3-butadiene | 230.3 | 69.1 | - | - | 379.0 | 2.7 | 75.2 | 1.3 | 0.0 | - |
| 1,3-diethylbenzene | 10.2 | 3.1 | 1.8 | 1.8 | 14.2 | 1.1 | 176.4 | 0.0 | 162.5 | - |
| 1,3,5-trimethylbenzene | 14.4 | 4.3 | 1.0 | 1.0 | 15.9 | 0.0 | 38.0 | 0.0 | 61.8 | - |
| 1,4-diethylbenzene | 46.7 | 14.0 | 1.9 | 1.9 | 3.6 | 3.8 | 73.7 | 0.0 | 88.4 | - |
| 2-ethyltoluene | 12.6 | 3.8 | 34.2 | 34.2 | 15.5 | 2.8 | 10.8 | 0.0 | 39.7 | - |
| 2-methyl-1-butene | 30.3 | 9.1 | 1.0 | 1.0 | 50.9 | 0.0 | 78.5 | 0.0 | 34.5 | - |
| 2-methyl-1-pentene | 10.6 | 3.2 | - | - | 5.0 | 0.0 | 10.4 | 0.0 | 5.3 | - |
| 2-methyl-2-butene | 6.0 | 1.8 | - | - | 9.3 | 0.0 | 21.2 | 0.0 | 31.2 | - |
| 2-methyl-2-pentene | 2.1 | 0.6 | 0.6 | 0.6 | - | - | - | - | - | - |
| 2-methylheptane | 7.1 | 2.1 | - | - | 8.6 | 0.0 | 5.4 | 0.0 | 11.2 | - |
| 2-methylhexane | 6.7 | 2.0 | - | - | 29.3 | 0.0 | 8.3 | 0.0 | 26.1 | - |
| 2-methylpentane | 50.2 | 15.1 | 1.0 | 1.0 | - | 2.1 | 11.1 | 0.0 | 22.0 | - |
| 2,2-dimethylbutane | 1.5 | 0.5 | - | - | 62.7 | 0.0 | 19.3 | 0.0 | 0.0 | - |
| 2,3-dimethyl-2-pentene | 7.5 | 2.3 | 1.0 | 1.0 | 14.3 | 0.0 | 5.1 | 0.0 | 18.7 | - |
| 2,3-dimethylbutane | 2.8 | 0.8 | 2.0 | 2.0 | 52.4 | 4.4 | 15.8 | 0.0 | 76.4 | - |
| 2,3,4-trimethylpentane | 5.3 | 1.6 | - | - | 8.2 | 0.0 | 27.2 | 0.0 | 30.8 | - |
| 2,4-dimethylpentane | - | - | - | - | 2.5 | 0.0 | 18.8 | 0.0 | 24.5 | - |

| | PIT-JP8 | | | | WPAT-JP8 | | WPAT-FT | | WPAT-Blend | |
|----------------------------|---------|-------|---------|---------|----------|--------|---------|--------|------------|--------|
| | Idle | Taxi | Landing | Takeoff | Idle | Cruise | Idle | Cruise | Idle | Cruise |
| 3-ethyltoluene | 15.8 | 4.7 | - | - | 8.8 | 0.5 | 33.8 | 0.0 | 24.5 | - |
| 3-methyl-1-butene | 29.5 | 8.9 | - | - | - | - | - | - | - | - |
| 3-methylheptane | 5.7 | 1.7 | 2.9 | 2.9 | - | 0.8 | 5.8 | 0.0 | 5.6 | - |
| 3-methylhexane | 24.5 | 7.4 | - | - | 2.5 | 0.8 | 9.3 | 0.0 | 20.3 | - |
| 3-methylpentane | 12.5 | 3.8 | - | - | 4.5 | 0.0 | 7.2 | 0.0 | 30.7 | - |
| 4-ethyltoluene | 7.7 | 2.3 | 3.1 | 3.1 | 26.3 | 0.0 | 64.4 | 0.0 | 85.4 | - |
| 4-methyl-1-pentene | 27.2 | 8.2 | 0.7 | 0.7 | - | - | - | - | - | - |
| 4-methylheptane | 5.6 | 1.7 | 1.8 | 1.8 | - | 0.0 | 9.1 | 0.0 | 8.9 | - |
| a-pinene | 6.2 | 1.9 | - | - | 16.9 | 0.8 | 85.7 | 0.0 | 78.6 | - |
| Acetylene | 2858.9 | 857.7 | 9.2 | 9.2 | 834.9 | 36.3 | 839.3 | 10.9 | 1080.9 | - |
| Benzene | 232.0 | 69.6 | 72.4 | 72.4 | 273.2 | 4.7 | 123.2 | 0.7 | 282.2 | - |
| Butane | 24.8 | 7.4 | 29.2 | 29.2 | 38.9 | 0.0 | 252.3 | 1.4 | 366.0 | - |
| Butylbenzene | 8.5 | 2.6 | - | - | 5.0 | 0.5 | 108.5 | 0.0 | 16.9 | - |
| c-1,3-dimethylcyclopentane | - | - | - | - | 0.7 | 0.0 | 11.8 | 0.0 | 2.8 | - |
| cis-2-butene | 11.7 | 3.5 | 0.9 | 0.9 | 14.7 | 0.5 | 85.5 | 1.0 | 78.9 | - |
| cis-2-hexene | 6.1 | 1.8 | 14.4 | 14.4 | 17.8 | 0.0 | 16.9 | 0.0 | 36.7 | - |
| cis-2-pentene | 8.4 | 2.5 | - | - | 59.6 | 0.0 | 66.9 | 0.0 | 45.3 | - |
| cis-3-hexene | 7.2 | 2.2 | - | - | - | - | - | - | - | - |
| Cyclohexane | 51.9 | 15.6 | - | - | 1.5 | 0.0 | 57.2 | 0.0 | 4.7 | - |
| Cyclohexene | 14.5 | 4.4 | 3.7 | 3.7 | 4.4 | 0.0 | 4.3 | 0.0 | 18.2 | - |
| Cyclopentane | 12.6 | 3.8 | 1.8 | 1.8 | 26.5 | 0.0 | 34.1 | 0.0 | 18.9 | - |
| Cyclopentene | 95.5 | 28.7 | - | - | 1.9 | 0.0 | 23.6 | 0.0 | 16.0 | - |
| Cyclopropane | 2.9 | 0.9 | - | - | - | - | - | - | - | - |
| Decane | 2.5 | 0.8 | 33.4 | 33.4 | 5.3 | 9.1 | 173.1 | 0.0 | 231.4 | - |
| Dodecane | 108.3 | 32.5 | 16.1 | 16.1 | - | - | - | - | - | - |
| Ethane | 115.5 | 34.7 | 83.3 | 83.3 | 149.6 | 26.6 | 143.7 | 0.0 | 158.6 | - |
| Ethene | 77.3 | 23.2 | 28.1 | 28.1 | 2865.5 | 49.6 | 1379.7 | 8.8 | 2984.4 | - |
| Ethylbenzene | 3.9 | 1.2 | 1.0 | 1.0 | 24.1 | 0.0 | 59.2 | 0.0 | 75.3 | - |
| Heptane | 5.9 | 1.8 | - | - | 132.8 | 0.0 | 16.3 | 0.0 | 114.0 | - |
| Hexane | 15.4 | 4.6 | 2.4 | 2.4 | 231.9 | 66.9 | 26.9 | 0.0 | 149.9 | - |

| | PIT-JP8 | | | | WPAT-JP8 | | WPAT-FT | | WPAT-Blend | |
|---------------------|---------|-------|---------|---------|----------|--------|---------|--------|------------|--------|
| | Idle | Taxi | Landing | Takeoff | Idle | Cruise | Idle | Cruise | Idle | Cruise |
| Hexylbenzene | 16.6 | 5.0 | - | - | - | - | - | - | - | - |
| Isobutene | 42.7 | 12.8 | 42.2 | 42.2 | 4.9 | 0.4 | 89.5 | 0.0 | 0.0 | - |
| Isobutene | 71.7 | 21.5 | 5.5 | 5.5 | 119.8 | 0.0 | 512.3 | 0.0 | 425.4 | - |
| Isopentane | 34.0 | 10.2 | 29.9 | 29.9 | 0.0 | 0.0 | 0.0 | 0.0 | 270.7 | - |
| Isoprene | 56.0 | 16.8 | - | - | 82.3 | 0.0 | 38.6 | 0.0 | 5.0 | - |
| Isopropylbenzene | 4.8 | 1.4 | 0.8 | 0.8 | 8.3 | 0.0 | 102.6 | 0.0 | 90.5 | - |
| limonene/indan | 7.9 | 2.4 | - | - | 0.0 | 0.0 | 0.0 | 0.0 | 0.0 | - |
| m-xylene | 26.4 | 7.9 | 1.1 | 1.1 | 37.6 | 0.0 | 55.5 | 0.0 | 7.3 | - |
| Methylcyclohexane | 14.4 | 4.3 | - | - | 5.1 | 0.0 | 5.8 | 0.0 | 15.9 | - |
| Methylcyclopentane | 11.2 | 3.4 | - | - | 2.6 | 0.0 | 11.8 | 0.0 | 14.2 | - |
| Naphthalene | 45.9 | 13.8 | 1.6 | 1.6 | - | - | - | - | - | - |
| Nonane | 36.1 | 10.8 | - | - | 112.5 | 0.0 | 3.4 | 0.0 | 121.3 | - |
| o-xylene | 5.2 | 1.6 | - | - | 24.1 | 0.0 | 66.4 | 0.0 | 80.9 | - |
| Octane | 7.5 | 2.3 | 0.9 | 0.9 | 14.9 | 0.0 | 3.4 | 0.0 | 21.7 | - |
| p-xylene | 4.8 | 1.4 | 3.8 | 3.8 | 19.6 | 1.0 | 44.4 | 0.0 | 95.8 | - |
| Pentane | 12.0 | 3.6 | 15.6 | 15.6 | 12.3 | 0.0 | 60.9 | 0.0 | 4.6 | - |
| Propane | 37.4 | 11.2 | 32.6 | 32.6 | 30.3 | 0.0 | 15.5 | 0.0 | 13.9 | - |
| Propene | 696.2 | 208.9 | 6.3 | 6.3 | 1087.8 | 5.3 | 1120.6 | 13.0 | 1545.6 | - |
| Propylbenzene | 16.6 | 5.0 | 1.4 | 1.4 | 14.6 | 0.0 | 35.3 | 0.0 | 38.4 | - |
| Propyne | 72.3 | 21.7 | - | - | 84.0 | 0.7 | 97.6 | 0.1 | 123.3 | - |
| sec-butylbenzene | 39.4 | 11.8 | 1.6 | 1.6 | - | - | - | - | - | - |
| Styrene | 8.2 | 2.5 | - | - | 12.4 | 0.0 | 7.5 | 0.0 | 24.2 | - |
| Tetradecane | 4.9 | 1.5 | 0.9 | 0.9 | - | - | - | - | - | - |
| Toluene | 84.7 | 25.4 | 3.0 | 3.0 | 108.5 | 1.5 | 34.0 | 0.3 | 98.6 | - |
| trans-1,3-hexadiene | 6.3 | 1.9 | - | - | 7.6 | 0.0 | 29.7 | 0.0 | 9.1 | - |
| trans-2-butene | 61.0 | 18.3 | 4.3 | 4.3 | 53.0 | 1.1 | 116.8 | 0.4 | 108.2 | - |
| trans-2-hexene | 9.5 | 2.9 | - | - | 9.9 | 0.0 | 13.0 | 0.0 | 13.4 | - |
| trans-2-pentene | 15.7 | 4.7 | - | - | 102.1 | 0.0 | 28.2 | 0.0 | 138.4 | - |
| Tridecane | 47.4 | 14.2 | 1.9 | 1.9 | - | - | - | - | - | - |
| Undecane | 93.7 | 28.1 | 15.8 | 15.8 | 2.2 | 2.5 | 45.4 | 0.0 | 99.1 | - |

| | | PIT-JP8 | | | WPAT-JP8 | | WPAT-FT | | WPAT-Blend | |
|------------------------------------|--------|---------|---------|---------|----------|--------|---------|--------|------------|--------|
| | Idle | Taxi | Landing | Takeoff | Idle | Cruise | Idle | Cruise | Idle | Cruise |
| POC | | | | | | | | | | |
| $C^* = 10^{-2} \mu\text{g m}^{-3}$ | 4.8 | 1.7 | 3.2 | 2.1 | 27.4 | 0.4 | 8.5 | NA | 15.3 | - |
| $C^* = 10^{-1} \mu\text{g m}^{-3}$ | 4.8 | 2.8 | 4.4 | 3.1 | 43.0 | 0.6 | 14.9 | NA | 24.1 | - |
| $C^* = 10^0 \mu\text{g m}^{-3}$ | 6.4 | 3.4 | 4.7 | 3.8 | 21.9 | 0.3 | 11.2 | NA | 16.3 | - |
| $C^* = 10^1 \mu\text{g m}^{-3}$ | 4.8 | 10.6 | 7.0 | 4.5 | 54.7 | 0.8 | 29.9 | NA | 49.2 | - |
| $C^* = 10^2 \mu\text{g m}^{-3}$ | 4.8 | 23.5 | 7.0 | 4.9 | 75.7 | 1.0 | 46.3 | NA | 64.2 | - |
| $C^* = 10^3 \mu\text{g m}^{-3}$ | 11.2 | 158.8 | 16.4 | 13.4 | 13.3 | 0.2 | 0.7 | NA | 7.0 | - |
| $C^* = 10^4 \mu\text{g m}^{-3}$ | 25.6 | 285.1 | 10.4 | 8.4 | 49.7 | 0.7 | 3.8 | NA | 23.2 | - |
| $C^* = 10^5 \mu\text{g m}^{-3}$ | 80.0 | 34.1 | 4.0 | 5.9 | 871.0 | 12.0 | 76.8 | NA | 429.8 | - |
| $C^* = 10^6 \mu\text{g m}^{-3}$ | 1459.4 | 39.1 | 20.0 | 11.3 | 4338.4 | 60.0 | 1403.5 | NA | 3323.0 | - |
| Summary | | | | | | | | | | |
| VOCs (SOA-forming) | 2503 | 751 | 342 | 342 | 2816 | 109 | 3359 | 6 | 4624 | - |
| VOCs (total) | 3903 | 1171 | 202 | 202 | 5057 | 119 | 3686 | 33 | 5907 | - |
| POCs | 1602 | 559 | 77 | 57 | 5495 | 76 | 1595 | 0 | 3952 | - |
| SOA | 936 | 101 | 117 | 17 | 2996 | 727 | 218 | 6 | 1897 | - |

T-SOA

Model predictions from the T-SOA module are compared to the measured SOA in Figure 33(a). The PIT and WPAT data are presented in separate rows of panels. These T-SOA predictions are an upper bound estimate since the SOA yields used in this work are at the high end of those reported in the literature. The model predicts that aromatics and alkenes are the most important T-SOA precursors. Except for the PIT-JP8-Takeoff and WPAT-FT-Idle experiments, the T-SOA module predicts less than half of the measured SOA production.

In order to quantify the model-measurement comparison, we calculate the fractional error:

$$Fractional\ Error = \frac{1}{N} \sum_{i=1}^N \frac{|P - M|}{\frac{P+M}{2}}$$

where, P is the predicted SOA, M is the measured SOA mass and N is number of data points. Fractional error values are listed in Figure 33(a). Both the PIT and WPAT experiments, the T-SOA predictions have a high fractional error. We hypothesize that the large unexplained SOA is a direct result of POC oxidation and is hereon referred to as NT-SOA.

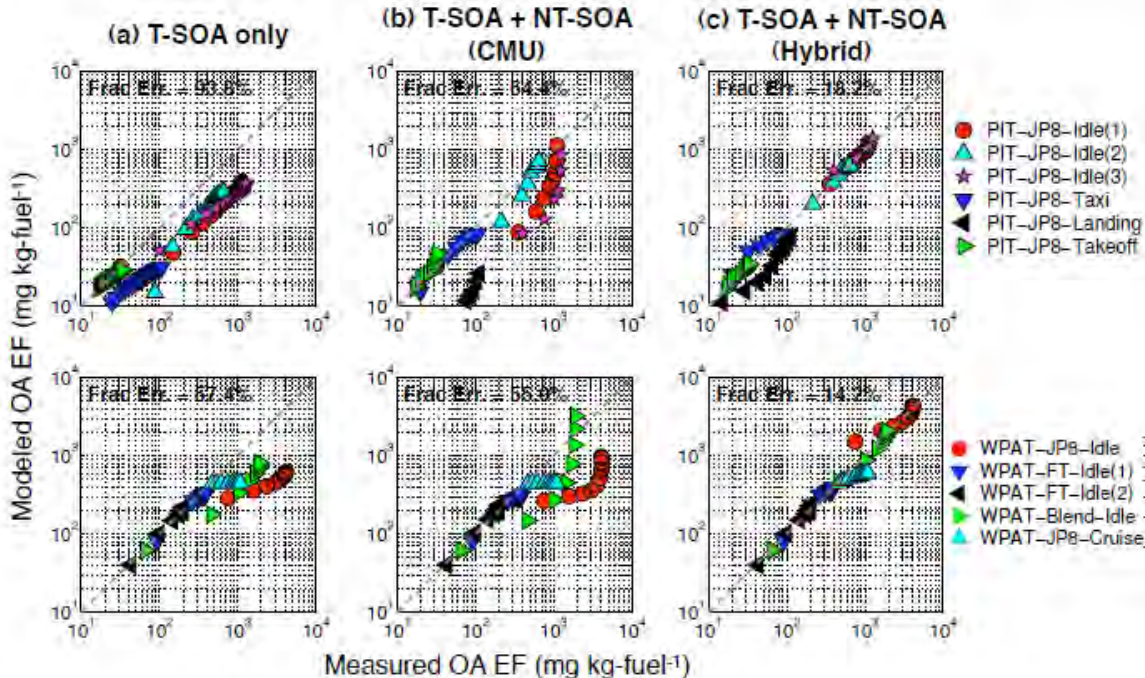


Figure 33. Modeled measured measured OA mass for the Pittsburgh / CFM56 (top row) and Wright Patterson / T63 (bottom row) field campaigns.

Mass balance: NT-SOA formed versus POC reacted

The NT-SOA is estimated by subtracting the predicted T-SOA mass from the measured SOA. Except for the WPAT-FT-Idle experiments, a large amount of NT-SOA is formed during the idle experiments (370-2600 mg kg-fuel⁻¹). Except for the WPAT-JP8-Cruise experiment, a significantly smaller amount of NT-SOA is also formed during the non-idle experiments (10-110 mg kg-fuel⁻¹). Apart from the WPAT-FT experiments, NT-SOA accounts for anywhere between 30 and 99% of the SOA measured in the chamber.

We evaluated a mass balance between the estimated NT-SOA that formed and the estimated fraction of the measured POC that reacted, assuming that the OH rate constant of the POCs is $4 \times 10^{-11} \text{ cm}^3 \text{ molecules}^{-1} \text{ s}^{-1}$. To quantify the mass balance, we calculate an effective NT-SOA yield,

$$\text{Effective NT-SOA Yield} = \frac{\text{NT-SOA formed}}{\text{POC reacted}}$$

Figure 34 plots the NT-SOA yield as a function of the organic aerosol concentration (C_{OA}). From a mass balance perspective, the NT-SOA yields appear reasonable, i.e. they are less than 1, which means that the amount of NT-SOA formed is less than the amount of POC reacted. The NT-SOA yields also appear reasonable when compared to the SOA yields for known IVOC compounds like *n*-dodecane, *n*-tridecane and *n*-heptadecane [92] and large (C_{10+}) branched and cyclic alkanes [93]. Finally, the NT-SOA yields increase with increasing C_{OA} , implying that POC oxidation products are semi-volatile, similar to those observed for VOCs. The low-load (idle, taxi) experiments appear to have higher yields compared to the non-idle experiments. This suggests that the idle emissions may be more efficient in forming NT-SOA than the non-idle emissions or that we are selectively underestimating emissions at idle conditions.

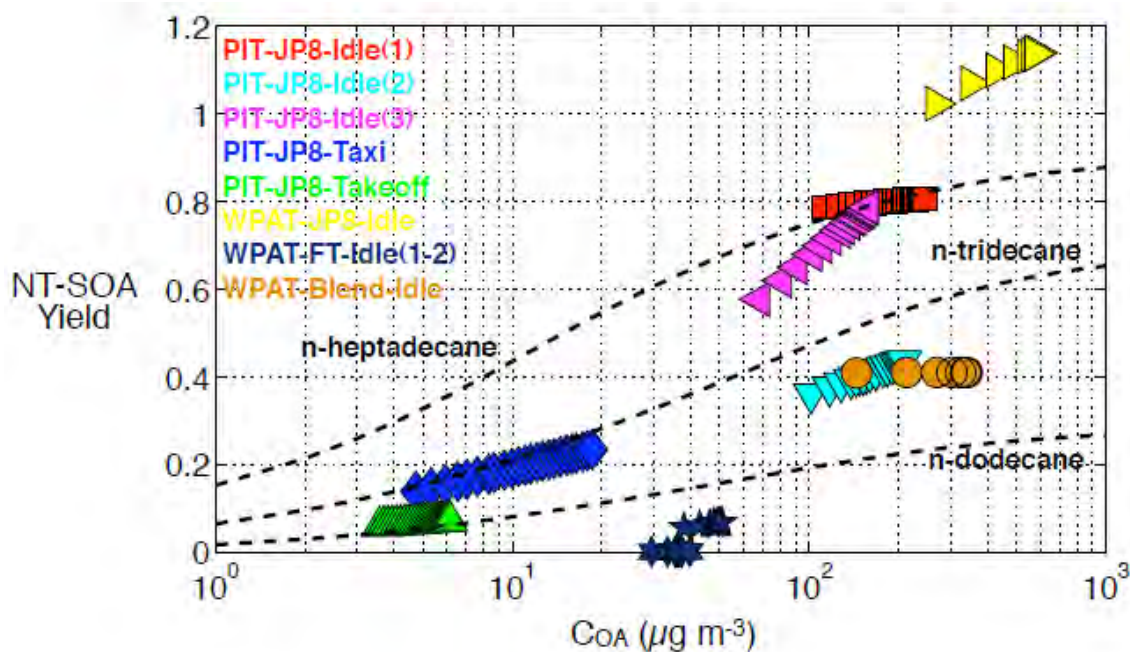


Figure 34. NT-SOA yield plotted as a function of COA. For reference, the dashed lines indicate SOA yields for *n*-dodecane, *n*-tridecane and *n*-heptadecane from Presto et al. [39].

NT-SOA

CMU method

The Robinson et al. [40] or Grieshop et al. [56] parameter sets severely under-predict SOA during the idle-experiments and over-predict SOA during the non-idle experiments. The problem is that the idle POC emissions are concentrated in the $10^6 \mu\text{g m}^{-3}$ bin and therefore require multiple generations of oxidation to reach the condensed phase. Therefore, we tried to fit the CMU method to the data to determine values for reaction rates (k_{OH}), fraction of oxygen added to the product per reaction (f_{oxy}) and shift in volatility (q). For each parameter we defined a physically plausible range of parameters and calculated the the value of $k_{OH} \cdot f_{oxy} \cdot q$ set that best fits the SOA data for each experiment. The set is chosen by minimizing the fractional error that quantifies how close the model predictions agree with measurements. For k_{OH} , we use a range of 1 to $5 \times 10^{-11} \text{ cm}^3 \text{ molecules}^{-1} \text{ s}^{-1}$ based on Atkinson and Arey [74]. For f_{oxy} , we use a range of 0.05 to 0.4, which corresponds to the addition of 1 to 5 oxygen atoms to a C_{15} alkane. For q , we use a range of 1 to 3, which corresponds to 1 to 3 orders of magnitude change in the product volatility.

We find that for all the idle experiments – except for the FT-Idle – a very aggressive parameter-set ($k_{OH} = 5 \times 10^{-11} \text{ cm}^3 \text{ molecules}^{-1} \text{ s}^{-1}$, $f_{oxy} = 0.4$, $q = 3$) is required to reproduce the measured SOA data. In comparison, a more modest parameter-set ($k_{OH} = 1\text{--}2 \times 10^{-11} \text{ cm}^3 \text{ molecules}^{-1} \text{ s}^{-1}$, $f_{oxy} = 0.05$, $q = 1$) is required to describe the non-idle SOA

data since a lot of the SOA formed in those experiments is explained by T-SOA. The results are illustrated in Figure 33(b), which plots model predictions using the CMU method with the best fit for each experiment against the SOA measured in the chamber. We find that there is modest improvement in model predictions for the PIT dataset but only very minor improvement for the WPAT study when compared to predictions from the T-SOA model alone; the trend is also reflected in the fractional error values listed in Figure 33.

The measured OA mass varies linearly or it rolls over with OH exposure in the chamber (Figure 35). In contrast, the NT-SOA predictions using the CMU method show the opposite trend, where very little NT-SOA is formed with the initial OH exposure and significantly more is formed with the later OH exposure; this effect is most clearly seen for the WPAT-Blend-Idle case (Figure 36). This happens because the CMU mechanism requires several generations of oxidation (a lot of OH exposure) before a large fraction of the products has a C^* low enough to partition into the particle phase. The problem is most severe in the idle experiments where most of the emissions are concentrated in the higher C^* bins (Table 13). The CMU method only works for the PIT-JP8-Taxi and PIT-JP8-Takeoff experiments primarily because a sizeable fraction of the emissions are found in lower C^* bins ($C^* = 10^2\text{-}10^4 \mu\text{g m}^{-3}$; Table 13).

Additional problems are revealed when we compare measured and predicted O:C ratios. The optimum (with respect to reproducing the measured SOA mass) parameter-set for the CMU mechanism significantly over-predicts the O:C ratio of OA for the JP8- and Blend-Idle experiments (>0.8). This occurs because the CMU mechanism requires high volatility POC precursors to go through several generations of oxidation before it reaches the particle phase and therefore ends up adding a lot of oxygen to the product, depending on the values of f_{oxy} and q . For example, for the optimized parameter-set for the PIT-JP8-Idle experiment ($k_{OH} = 4 \times 10^{-11} \text{ cm}^3 \text{ molecules}^{-1} \text{ s}^{-1}$, $f_{oxy} = 0.40$, $q = 2$), the O:C of the product would be close to 1 after only two generations of oxidation. An O:C ratio of 1 is very high and probably unrealistic considering that the AMS estimated O:C ratio of aged ambient OA rarely exceed 0.8 [94]. This result might imply that the NT-SOA formed during our experiments represents very few generations of oxidation with very modest amounts of oxygen added per reaction. This is further proof that a larger shift in volatility, as implemented by the Hybrid method, is more realistic than the CMU parameterization.

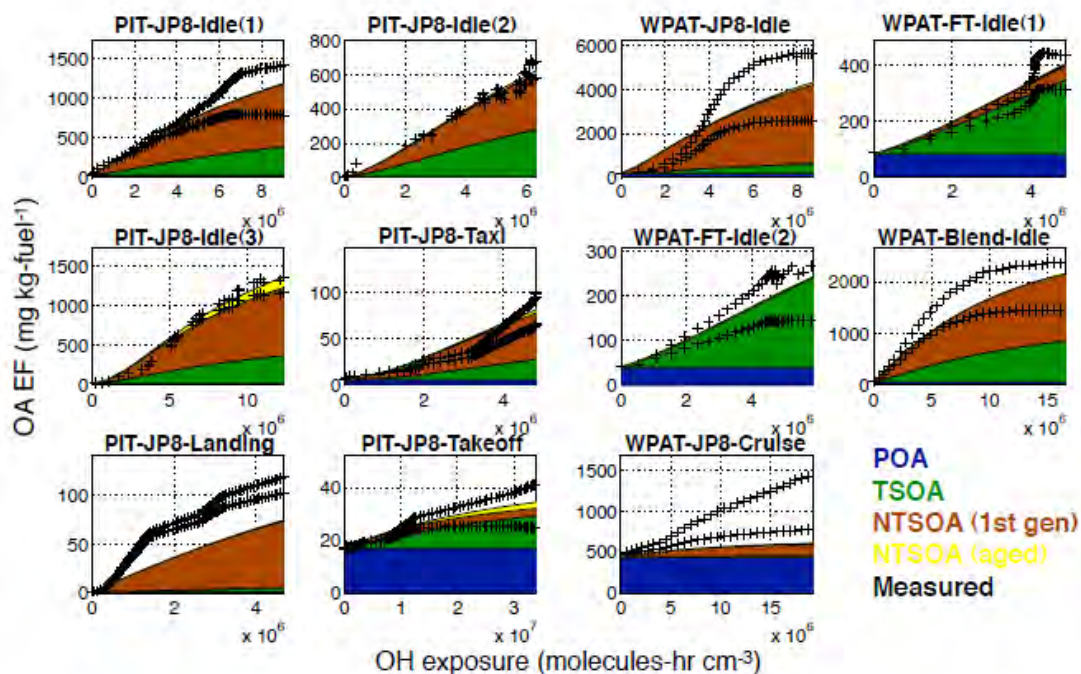


Figure 35. Model measurement comparison of SOA formation for each experiment. NT-SOA is predicted using the Hybrid method using best fits for each experiment.

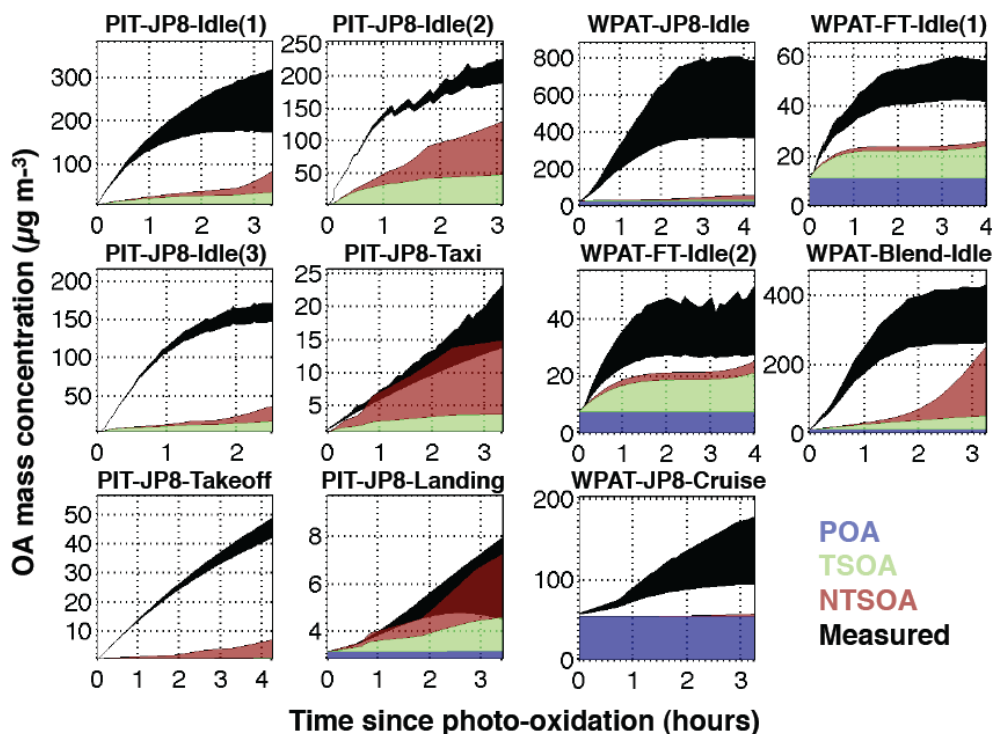


Figure 36. Same as Figure 35 but using optimized CMU parameterization for NT SOA formation.

Hybrid method

With this method, the data are fit to determine a set of VBS yields (α in equation 9) for each of the nine different POC precursors for each JP8 experiment. As described previously, the VBS yields for the different POC precursors are coupled and therefore there are only 4 free parameters. Figure 35 plots the model-measurement comparison for all the experiments, with the NT-SOA calculated using the best fit for the Hybrid method. The uncertainty in the measured SOA is shown through lower and upper bound estimates. The contribution from the first generation of oxidation is labeled 'NTSOA (1st gen)' and the contribution from multi-generational oxidation is labeled 'NTSOA (aged)'. The Hybrid method predictions are much closer to the data than the CMU method. The improved performance is clearly demonstrated in Figure 33(c) where, in both field campaigns, the optimized Hybrid mechanism parameter set results in a significantly lower fractional error than the optimized CMU mechanism parameter set.

Figure 35 indicates that the multi-generational oxidation mechanism (NT-SOA aged) used here makes a negligible contribution to the SOA mass over the range of oxidant exposures observed in these experiments. Therefore, these data can be used to determine NT-SOA yields that offer a realistic representation of the product distribution arising after the first few generations of oxidation.

To compare the NT-SOA yields across different experiments, the VBS yields are represented using a yield (Y), which is defined as the SOA formed by each POC precursor divided by the calculated mass of that precursor that reacted. Figure 37 plots the NT-SOA yields for select POC precursors as a function of C_{OA} ; Figure 37a shows yields for the POC precursors in the 10^6 and $10^5 \mu\text{g m}^{-3}$ bins and Figure 37b shows yields for POC precursors in 10^4 , 10^3 and $10^2 \mu\text{g m}^{-3}$ bins. For visual clarity, we have excluded all POC precursors that contribute less than 15% to the NT-SOA mass. The lower volatility components ($\leq 10^1 \mu\text{g m}^{-3}$; not shown) of the POC contribute little NT-SOA mass because these emissions are generally low or because very little of this mass is partitioned into the gas-phase and available for oxidation.

For all the idle experiments (Figure 37a), irrespective of the field campaign, almost all of the NT-SOA is produced from oxidation of POC in the highest C^* bins (10^5 and $10^6 \mu\text{g m}^{-3}$), which dominate the low volatility organics (Table 13). A major component of this material appears to be unburned fuel [95], which peaks at C_{11} or $C^*=10^6$ or $10^7 \mu\text{g m}^{-3}$. In fact, two of the PIT-JP8-Idle (except for PIT-JP8-Idle(2)) and WPAT-JP8-Idle experiments have similar yields even though the experiments were conducted using emissions from different engines. In comparison, for the non-idle experiments (Figure 37b), the NT-SOA arises from POC in the lower C^* bins (10^2 , 10^3 and $10^4 \mu\text{g m}^{-3}$). At higher engine loads the combustion efficiency is higher (essentially no unburned fuel) and low volatility organic emissions are dominated by slightly lower volatility (10^2 , 10^3 or $10^4 \mu\text{g m}^{-3}$).

The estimated yields for the JP8-Idle experiments are very close to or in some cases greater than 1. This is much higher than expected if one considers the yields of *n*-alkanes. For example, *n*-dodecane falls in the $10^6 \mu\text{g m}^{-3}$ bin; it has a yield of around 20-30% at the conditions (C_{OA}) of the idle experiments (Figure 37). A number of factors likely

contribute to the unexpectedly high yields. Mostly likely it is due to under-estimating the mass of POC emissions using the TD-GCMS. The technique used to quantify POC emissions works best for hydrocarbons that are reduced and less volatile than roughly a C_{12} alkane. Somewhat more volatile compounds ($C_9 - C_{11}$) likely also contribute to NT-SOA in the idle experiments. Second, the POC emissions likely also contain oxygenated species and more volatile species ($\sim C_{8-11}$), both of which are not characterized by the method but contribute to SOA formation. Since we do not account for these species while calculating the POC reacted, we overestimate the yields of the species included in the model (10^5 and $10^6 \mu g m^{-3}$ bins). Alternatively, the idle-yields could be greater than 1 simply because the POCs on oxidation might result in the product being larger than the precursor due to the addition of oxygen or other functional groups. In comparison, Figure 37b indicates that there is better agreement between the estimated yields of the lower volatility bins and yield data for *n*-alkanes.

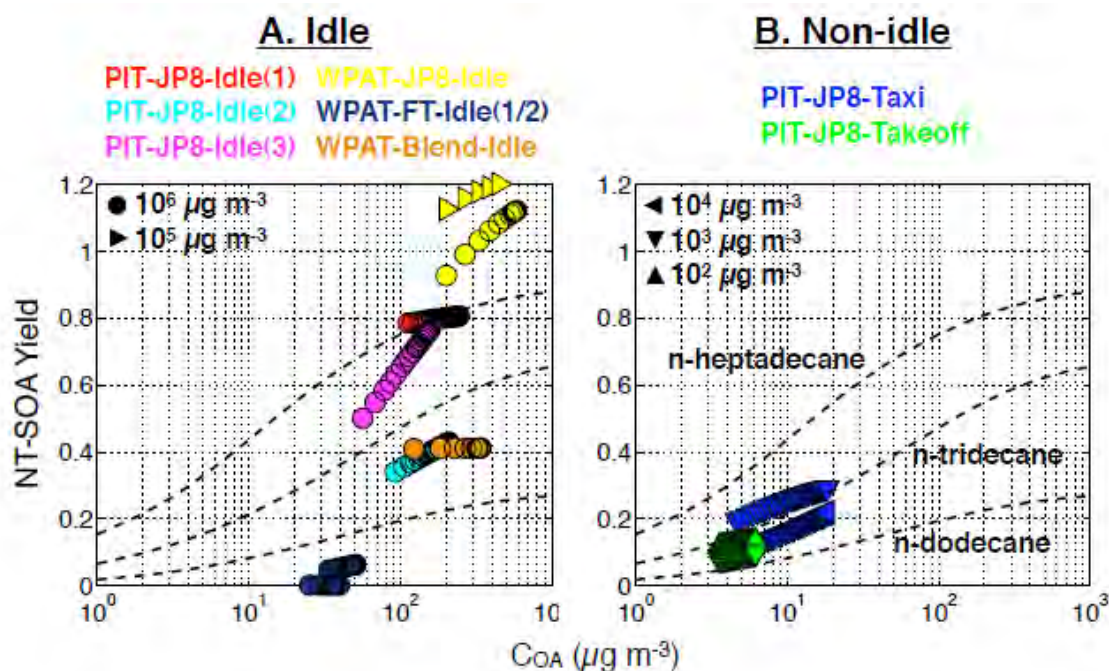


Figure 37. NT-SOA yield plotted for different POC precursors as a function of CO_A . For reference, we also include SOA yields for *n*-dodecane, *n*-tridecane and *n*-heptadecane (dotted black lines) from Presto et al. [39].

The variation in NT-SOA yields at different engine loads appears to be a complex function of the composition, volatility and CO_A . The data in Figure 37 suggests that SOA formation from the JP8-Taxi and JP8-Takeoff emissions are similar since they have essentially the same effective yields. The JP8-ground-idle data also appear to be self-consistent because the variability in estimated yields appears to be explained by the varying CO_A and therefore partitioning. However, it is uncertain if the ground idle and non-ground-idle emissions have the same NT-SOA yields since the experiments were performed at different CO_A . There are several pieces of evidence that suggest the yields

may be different. First, Figure 13c indicates that the m/z 57 chromatograms for the POC emissions (precursor) during the PIT-JP8-Idle(1) experiment was very different from those during the PIT-JP8-Taxi, -Landing and -Takeoff experiments. The signal-weighted average mass spectrum of the different emissions and the thermodenuder of the different aged aerosols support this conclusion.

For use in chemical transport models, we developed two parameterizations for aircraft NT-SOA – one for ground idle and a second for non-ground-idle emissions. We use all the JP8-Idle experiments – except PIT-JP8-Idle(2), which appears to be an outlier relative to the 3 other idle experiments – to derive NT-SOA yields (α) for the JP8-Idle emissions and we use the PIT-JP8-Taxi and PIT-JP8-Takeoff experiments to derive NT-SOA yields (α) for the JP8-Non-idle emissions. Table 14 lists the two parameterizations.

Figure 38 plots the model-measurement comparison using the (a) JP8-Idle and (b) JP8-Non-idle parameterizations to data from all the experiments. The JP8-Idle parameterization produces good model-measurement comparison for all the JP8 idle experiments in both campaigns but significantly overpredicts the non-ground-idle data. The JP8-Non-idle parameterization also produces good model measurement comparison for all the JP8 non-idle experiments but underpredicts the NT-SOA measured in ground idle experiments.

NT-SOA from FT: We also compared predictions of the hybrid model fit to the JP8-idle data to the measured NT-SOA from the neat FT and JP8-FT blend experiments. The JP8-ground-idle parameterization over-predicts the measured OA in the blend experiment by a factor of 2 over-predict the OA in the neat FT experiment by a factor of 4. Therefore, the JP8-based parameterization will always over-predict the NT-SOA formed from emissions of aircraft using FT fuels. The FT and JP8 emissions have similar volatility distributions, therefore the differences in NT-SOA formation must be due to the differences in the composition. This is to be expected given the differences in composition between JP8 and FT (Table 4). The key difference is that the JP8 contains 17% aromatics (which generate high SOA yields) versus essentially zero for the FT. This difference is important since unburned fuel appears to contribute a significant fraction of the organic emissions from the T63 (and CFM56) at idle.

To further investigate potential effects of fuel composition on SOA formation, we conducted smog chamber experiments using unburned fuel. Briefly, several hundred $\mu\text{g m}^{-3}$ of unburned fuel are added to a smog chamber and allowed to react with the OH radical under high NO_x conditions. Both the OH radical and NO_x are produced via photolysis of HONO, which is added to the chamber through a bubbler. The decay of the unburned fuel is measured using a GC-MS. The SOA formed from the fuel is measured using an SMPS and an AMS. We find that $\sim 600 \mu\text{g m}^{-3}$ of JP8 fuel forms $60\text{--}80 \mu\text{g m}^{-3}$ of SOA while the same amount of FT fuel forms less than $2 \mu\text{g m}^{-3}$ of SOA. Even when $\sim 1100 \mu\text{g m}^{-3}$ of FT fuel is added to the chamber, we only measure $3\text{--}6 \mu\text{g m}^{-3}$ of SOA. The large difference in SOA formation can be attributed to the chemical composition of the fuel. JP8 consists mostly of alkanes (straight and cyclic) and aromatics (70%), all of which have higher SOA yields than branched alkanes that mostly constitute FT fuel (88%) [75, 96].

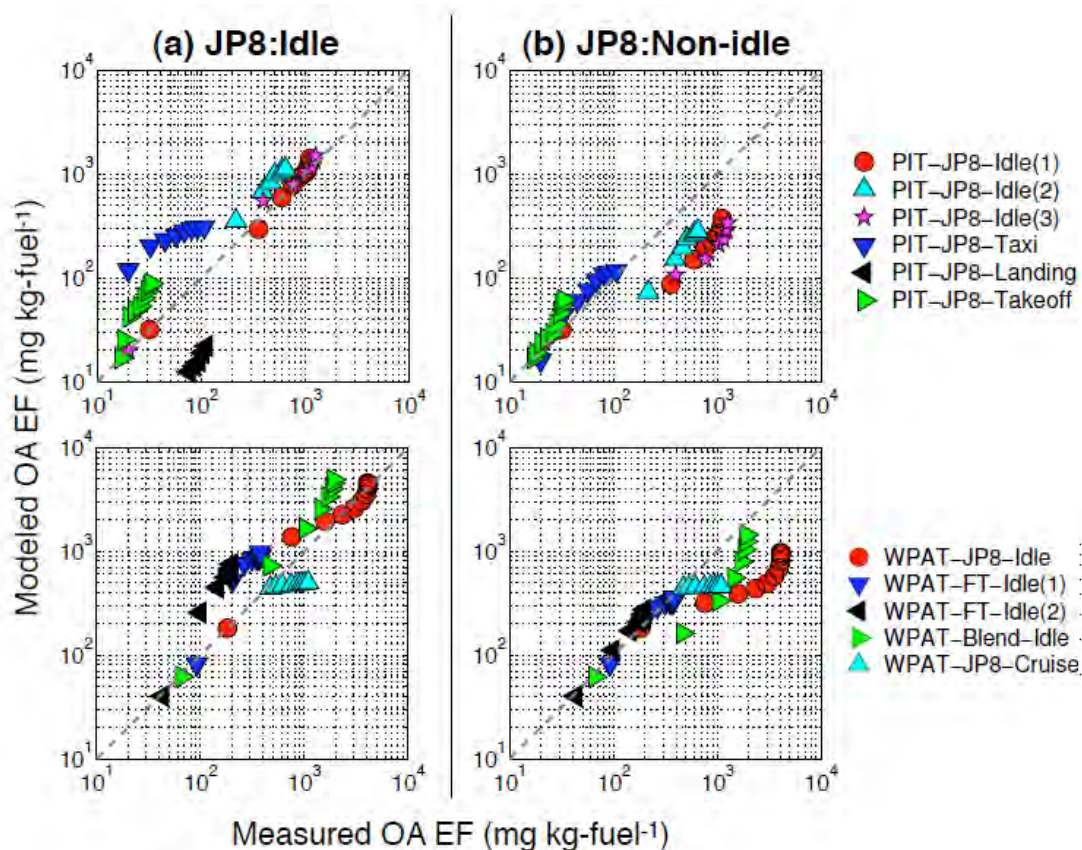


Figure 38. Model measurement comparison of OA concentrations using (a) JP8 ground idle parameterization and (b) JP8 non-idle parameterization. The top row shows data from the Pittsburgh experiments; the bottom row shows data for the Wright Patterson experiments.

Table 14. Parameters for hybrid NT-SOA model.

| C* of POC precursor bin ($\mu\text{g m}^{-3}$) | OH rate constant ($\text{cm}^3 \text{ molecule}^{-1} \text{ s}^{-1}$) | Non-ground-idle | | | | Ground idle | | | |
|--|---|-------------------|------|------|------|-------------------|------|------|------|
| | | Yields for C* bin | | | | Yields for C* bin | | | |
| | | 1 | 10 | 100 | 1000 | 1 | 10 | 100 | 1000 |
| 10^2 | 4.00E-11 | 0.00 | 0.46 | 0.39 | 0.00 | 0.14 | 0.99 | 0.33 | 0.00 |
| 10^3 | 4.00E-11 | 0.00 | 0.31 | 0.92 | 0.00 | 0.14 | 0.98 | 0.35 | 0.00 |
| 10^4 | 3.00E-11 | 0.00 | 0.00 | 1.45 | 0.00 | 0.18 | 0.82 | 0.48 | 0.00 |
| 10^5 | 3.00E-11 | 0.00 | 0.00 | 0.29 | 0.00 | 0.36 | 0.13 | 1.00 | 0.00 |
| 10^6 | 3.00E-11 | 0.00 | 0.00 | 0.03 | 0.00 | 0.13 | 0.00 | 1.00 | 0.00 |

Conclusions and Implications for Future Research/Implementation

Experiments were performed to measure the PM mass and organic vapor emissions from CFM56 and T63 gas turbine engines. The experiments were designed to investigate two major hypotheses and several scientific objectives. Specific technical objectives described in the proposal included:

1. Measure the chemical composition and properties of volatile PM in emissions from military aircraft as a function of dilution and photochemical age,
2. Quantify the effects of dilution, temperature, and photochemical age on gas-particle partitioning of volatile emissions from military aircraft, and
3. Develop a theoretical model to predict the volatile PM emissions across the entire range of atmospheric conditions from the engine exit plane to highly dilute background as a function of photochemical age.

The project accomplished all of these objectives and expanded its scope to investigate the effects of fuel composition on primary PM emissions and secondary PM production by conducting experiments with a Fischer-Tropsch (FT) fuel. In this section we summarize the major results of this project, focusing on conclusions that were consistent across experiments performed with different engines.

The composition of the primary PM mass emissions from CFM56 and T63 engines varied with engine load. For both engines, the PM emissions at low load are dominated by organics (volatile PM) and by EC (non-volatile PM) at high load. Although sampling artifacts and variable gas-particle partitioning complicated quantifying the POA emission factors, all of the data indicate that POA emissions are significant at every engine load. The volatile PM emissions were almost exclusively organics because measured emissions of primary sulfate were low at all loads (even when the engines were operated on fuels with significant sulfur content). This may have been due to the loss of SO_3 in the transfer line. Operating the T63 on FT fuel substantially reduced the primary PM emissions. Our conclusions regarding the effects of engine load and fuel composition on the primary PM emissions are consistent with results from previous studies.

The novel results from the primary emission work were the very large organic aerosol sampling artifacts and a comprehensive evaluation of the overall mass balance of the organic emissions that demonstrate the importance of low-volatility vapor emissions. Neither of these issues had been previously addressed in the context of aircraft emissions. For example, for the CFM56 engine, more than half of the organics collected on a quartz filter appear to be positive artifact (adsorbed vapors). Emissions of low volatility vapors were much larger than the organic emissions in the particulate phase, indicating a very large pool of secondary PM precursors.

Before this project, secondary PM production from photo-oxidation of aircraft exhaust had not been systematically investigated. Therefore, the smog chamber experiments were a novel, and important, component of this project. The results demonstrated that photo-oxidation creates substantial secondary particulate matter,

greatly exceeding (by as much as a factor of 60) the direct PM emissions after an hour or less of aging at typical summertime conditions. This was observed in every smog chamber experiment except one using exhaust from the T63 engine operating at cruise load on neat FT fuel; almost no secondary PM was formed during this experiment. For the CFM56 engine, the composition of secondary PM formed strongly depended on load. At 4% load, secondary PM was dominated by secondary organic aerosol (SOA). At higher engine loads, the secondary PM was mainly secondary sulfate with still significant contributions from SOA. SOA formation alone always exceeded the primary PM emissions; therefore, even completely removing sulfur from jet fuel will not solve the problem of secondary PM production. For the T63 engine, the secondary PM was always dominated by SOA because the organic emissions were much higher compared to the CFM56 engine.

The experiments with the T63 engine indicate that FT fuel can reduce SOA formation at both idle and cruise loads. For example, operating the T63 on neat FT reduced SOA formation by a factor of 40 at idle load, and there was no production of SOA at cruise load with the FT fuel. Although neat FT fuel significantly reduced primary PM emissions and secondary PM formation, it is not certified for use in operating aircraft because of problems such as leaking gaskets. A 50:50 FT/JP-8 blend has recently been certified under ASTM standard D7566, which specifies aviation turbine fuels containing synthesized hydrocarbons. This blend reduced both the primary PM and secondary PM formation (after accounting for partitioning effects) by about half.

The smog chamber data were used to test models that predict secondary PM formation. The sulfate production could be explained based on the measured SO_2 and oxidant concentrations. However, a model based on the oxidation of traditional SOA precursors (single ring aromatics and other VOCs) could not explain the measured SOA formation. Instead one needs to account for emissions of low-volatility, non-traditional SOA precursors, most of which cannot be speciated. We developed a semi-empirical model based on the measured low volatility organic emissions data to explain the measured SOA production. The NT-SOA formation has been parameterized using the volatility basis framework for use in chemical transport models, such as PMCAMx and CMAQ.

Hypothesis Testing

The research was designed to investigate two hypotheses, both of which addressed core knowledge gaps in our understanding of volatile PM emissions aircraft. The first was that volatile PM concentrations depend on gas-particle partitioning of compounds that are semivolatile at atmospheric conditions. The second hypothesis is that photo-oxidation in the exhaust plume will create significant volatile PM, greatly exceeding the non-volatile emissions or the volatile particles that form in the plume shortly after leaving engine. Neither of these hypotheses had been previously investigated in the context of aircraft emissions. This project demonstrated that both of these hypotheses are true based on multiple pieces of independent experimental evidence obtained from different types of aircraft engines.

The first hypothesis, semivolatile character of volatile PM, was directly demonstrated by perturbing the concentration and temperature of the exhaust and then measuring the

changes in gas-particle partitioning. First, modest heating in a thermodenuder caused a large fraction of the primary organic aerosol to evaporate. Second, isothermal addition of exhaust to the smog chamber caused the volatile PM emission factor to increase substantially (by more than a factor of 2) due to shifts in gas-particle partitioning. This was observed in experiments performed using the CFM56 and T63 engines. Although these engines had very different emission rates (T63 was much higher emitting) very similar partitioning behavior was observed for both engines.

The direct measurements of gas-particle partitioning are supported by results of GC-MS analysis of samples collected from CFM56 engines and a T63 engine. Organic emissions are comprised of a complex mixture of species that span a wide range of volatilities, from completely volatile to essentially non-volatile. The organic emissions are dominated by VOCs at all loads and only the lowest volatility portion of the organic emissions partition into the condensed phase to form volatile PM mass. However, the vast majority (80%+) of the lowest volatility organics are semivolatile organic compounds (SVOC) and therefore exist in both phases at typical atmospheric conditions. The gas-particle partitioning of these compounds, and thus the amount of volatile PM, will change with varying atmospheric temperature and pollution levels. Furthermore, gas-particle partitioning predictions based on the GC-MS quantitatively agreed with measured changes in partitioning.

The finding that a significant fraction of the volatile PM is semivolatile at atmospheric conditions has important implications for how we measure and simulate volatile PM emissions from aircraft. Partitioning depends on the temperature and composition of the plume; therefore one cannot define PM emission from an aircraft using a traditional PM emissions factor. Neglecting the dynamic gas-particle partitioning of primary organic aerosol emissions will lead to errors in volatile PM mass by a factor of 4 or more (Figure 39). It also makes it difficult to precisely define standards for certification testing. To account for this dynamic character one must measure the total emissions rate of semivolatile species and the volatility distribution of the emissions. These data can then be used by a gas-particle partitioning model to predict the fraction of these emissions that exist in the particle phase. In this project we have obtained this information for three engines (two CFM56 engines and a T63 engine). Parameterizations of the data were developed for use in chemical transport models such as PMCAMx or CMAQ that have implemented the volatility basis set approach for simulating organic aerosols.

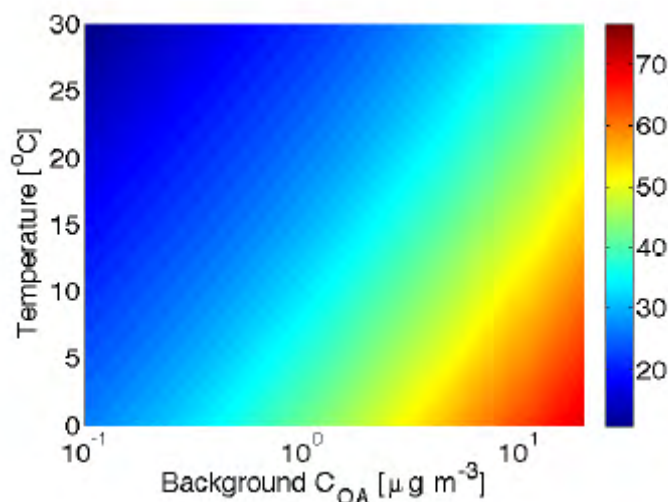


Figure 39. Variation in primary organic aerosol emissions (units of color bar -- mg kg-fuel⁻¹) from the T63 across atmospheric conditions (temperature and organic aerosol concentration). The emission factors are calculated using the volatility distribution of POC emissions listed in Table 13, equilibrium partitioning theory (equation 7), and the enthalpy of vaporization values in Ranjan et al. [42].

The second hypothesis, that photo-oxidation in the exhaust plume will create significant volatile PM, was directly evaluated by conducting smog chamber experiments with dilute exhaust. As discussed previously, these experiments indicate that photo-oxidation of aircraft emissions produces significant amounts of secondary PM, which, under typical summertime conditions, can exceed the primary emissions within minutes of the exhaust leaving the engine. This was observed in all experiments except those using neat FT fuel (a fuel not certified for use in operating aircraft). Therefore secondary PM production must be accounted for in order to assess the contribution of aircraft emissions to urban and regional air pollution.

The conclusion of substantial SOA production is supported by precursor emissions data. For example, the emissions of intermediate volatility organic compounds from a CFM56 engine are ~70 and ~3 times larger than the POA emissions at 4% and 85% load, respectively. Therefore, assuming reasonable SOA yields [89, 97, 98], secondary organic aerosol formation from the photo-oxidation of exhaust plumes should eclipse POA at all loads – exactly what was observed in the smog chamber experiments.

Research needs

This project has identified some important future research needs. In particular the fact that secondary PM production may dominate the primary PM emissions (both volatile and non-volatile) means that more research is needed to better constrain the secondary PM production.

- In this project we tested two different types of engines, neither of which represent the latest, state-of-the-art technology. Similar experiments are needed to evaluate the potential for secondary PM formation from a broader

range of engines, in particular new technologies. These data will allow additional testing of the hypothesis regarding the importance of secondary PM production. They are also needed to develop more robust secondary PM parameterizations for chemical transport models.

- SVOC and IVOC emissions need to be measured more routinely in aircraft testing across a range of engine loads. The SVOC data are needed to predict the dynamic gas-particle partitioning of volatile PM emissions across the entire range of atmospheric conditions from the engine exit plane to the dilute remote atmosphere. The IVOC data are needed as a critical input for secondary organic aerosol modules. Data are needed across the entire range of important engine technologies to develop robust emission inventories for chemical transport modeling.
- Previous research has shown that changing the VOC/NO_x ratio can have a substantial influence on SOA production [99-102]. In this project, the smog experiments were conducted using emissions mixed with clean air. Therefore the VOC/NO_x ratio was determined by emissions. At low engine load, the emissions are dominated by VOCs while at high load they are dominated by NO_x. In real atmosphere, the VOC/NO_x of the plume will be strongly influenced by background conditions. A good target VOC/NO_x ratio is ~3:1 ppbC/ppbNO_x, which is representative of a typical urban area. The VOC/NO_x ratio of the high load emissions is generally much lower than 3:1 ppbC/ppbNO_x while the ratio at low load is much higher than 3:1 ppbC/ppbNO_x. Research is needed to systematically evaluate the effects of VOC/NO_x ratio on SOA formation in aircraft exhaust.
- The results of this project (and other research) have shown that organic vapor emissions (VOC and IVOC) can increase exponentially at loads less than 7% (the lowest load of the ICAO LTO cycle). These loads are commonly encountered during ground operations [103] but have not been formally incorporated into standard aircraft duty cycles such as the ICAO LTO. Research is needed to better characterize the duty cycle associated with ground operations and incorporate this information into inventories.
- Previous modeling studies [104, 105] have found that aircraft emissions can contribute significantly to ground-level PM concentrations in urban environments. However, these studies have not accounted for the secondary PM production observed in our work. This suggests that these previous modeling studies have underestimated the impact of aircraft exhaust on ambient pollution levels. The new SOA parameterizations developed by this project need to be incorporated into modeling studies to better constrain the contribution of ambient pollution.

Implementation

The major direct implementation of the results from this project is by two research groups into chemical transport models to evaluate the effects of aircraft emissions on

local, regional and global air quality. The first group is that of Dr. Sarav Arunachalam who is using a plume in grid approach with CMAQ to simulate air pollution levels around airfields. The second is the group of Dr. Steven Barrett at the Massachusetts Institute of Technology, who use GEOS-CHEM and other chemical transport models. These groups will hopefully use these models to begin to address one of the aforementioned research needs. Furthermore, formally incorporating the secondary PM module developed by this project will lead to more robust assessment of the impacts of both military and civilian aircraft on urban and regional air pollution.

Literature Cited

1. Penner, J.E., et al., *Aviation and the Global Atmosphere* 1999, Cambridge, UK: Cambridge University Press.
2. Robinson, A.L., et al., *Updating the Conceptual Model for Fine Particle Mass Emissions from Combustion Systems*. Journal of the Air & Waste Management Association, 2010. **60**(10): p. 1204–1222.
3. Agrawal, H., et al., *Characterization of chemical and particulate emissions from aircraft engines*. Atmospheric Environment, 2008. **42**: p. 4380–4392.
4. Anderson, B.E., et al., *Experiment to Characterize Aircraft Volatile Aerosol and Trace-Species Emissions (EXCAVATE)*, 2005.
5. Lobo, P., et al., *Physical characterization of aerosol emissions from a commercial gas turbine engine*. Journal of Propulsion and Power, 2007. **23**: p. 919-929.
6. Onasch, T.B., et al., *Chemical Properties of Aircraft Engine Particulate Exhaust Emissions*. Journal of Propulsion and Power, 2009. **25**(5): p. 1121-1137.
7. Petzold, A. and F.R. Schroder, *Jet engine exhaust aerosol characterization*. Aerosol Science & Technology, 1998. **28**: p. 62-76.
8. Schumann, U., et al., *Influence of fuel sulfur on the composition of aircraft exhaust plumes: The experiments SULFUR 1-7*. Journal of Geophysical Research-Atmospheres, 2002. **107**(D15).
9. Timko, M.T., et al., *Gas Turbine Engine Emissions---Part II: Chemical Properties of Particulate Matter*. Journal of Engineering for Gas Turbines and Power, 2010. **132**(6): p. 061505.
10. Wey, C.C., et al., *Aircraft Particle Emissions eXperiment (APEX)*, 2006, National Aeronautics and Space Administration, Glenn Research Center: Cleveland OH.
11. Yu, Z., et al., *Characterization of Lubrication Oil Emissions from Aircraft Engines*. Environmental Science & Technology, 2010. **44**(24): p. 9530-9534.
12. England, G.C., et al., *Dilution-Based Emissions Sampling from Stationary Sources: Part I—Compact Sampler Methodology and Performance*. Journal of the Air & Waste Management Association, 2007. **7**(1): p. 65-78.
13. Hildemann, L.M., G.R. Cass, and G.R. Markowski, *A dilution stack sampler for collection of organic aerosol emissions: design characterization and field tests*. Aerosol Science and Technology, 1989. **10**: p. 193-204.
14. Wong, H.-W., et al., *Design Parameters for an Aircraft Engine Exit Plane Particle Sampling System*. Journal of Engineering for Gas Turbines and Power, 2011. **133**(2): p. 021501.
15. Starik, A.M., et al., *Effect of aerosol precursors from gas turbine engines on the volatile sulfate aerosols and ion clusters formation in aircraft plumes*. Physical Chemistry Chemical Physics, 2004. **6**(13): p. 3426-3436.

16. Yu, F.Q. and R.P. Turco, *The formation and evolution of aerosols in stratospheric aircraft plumes: Numerical simulations and comparisons with observations*. Journal of Geophysical Research-Atmospheres, 1998. **103**(D20): p. 25915-25934.
17. Yu, F.Q. and R.P. Turco, *The role of ions in the formation and evolution of particles in aircraft plumes*. Geophysical Research Letters, 1997. **24**(15): p. 1927-1930.
18. Karcher, B., et al., *A unified model for ultrafine aircraft particle emissions*. Journal of Geophysical Research-Atmospheres, 2000. **105**(D24): p. 29379-29386.
19. Flagan, R.C. and J.H. Seinfeld, *Fundamentals of Air Pollution Engineering* 1988, Englewood Cliffs, NJ: Prentice-Hall.
20. Schroder, F., et al., *In situ studies on volatile jet exhaust particle emissions: Impact of fuel sulfur content and environmental conditions on nuclei mode aerosols*. Journal of Geophysical Research-Atmospheres, 2000. **105**(D15): p. 19941-19954.
21. Karcher, B., et al., *Ultrafine aerosol particles in aircraft plumes: Analysis of growth mechanisms*. Geophysical Research Letters, 1998. **25**(15): p. 2793-2796.
22. Yu, F.Q., R.P. Turco, and B. Karcher, *The possible role of organics in the formation and evolution of ultrafine aircraft particles*. Journal of Geophysical Research-Atmospheres, 1999. **104**(D4): p. 4079-4087.
23. Spicer, C.W., et al., *Chemical-Composition of Exhaust from Aircraft Turbine-Engines*. Journal of Engineering for Gas Turbines and Power-Transactions of the Asme, 1992. **114**(1): p. 111-117.
24. Spicer, C.W., et al., *Chemical-Composition and Photochemical Reactivity of Exhaust from Aircraft Turbine-Engines*. Annales Geophysicae-Atmospheres Hydrospheres and Space Sciences, 1994. **12**(10-11): p. 944-955.
25. Herndon, S.C., et al., *Hydrocarbon emissions from in-use commercial aircraft during airport operations*. Environmental Science & Technology, 2006. **40**(14): p. 4406-4413.
26. Anderson, B.E., G. Chen, and D.R. Blake, *Hydrocarbon emissions from a modern commercial airliner*. Atmospheric Environment, 2006. **40**(19): p. 3601-3612.
27. Schauer, J.J., et al., *Measurement of emissions from air pollution sources. 2. C-1 through C-30 organic compounds from medium duty diesel trucks*. Environmental Science & Technology, 1999. **33**(10): p. 1578-1587.
28. Schauer, J.J., et al., *Measurement of emissions from air pollution sources. 3. C-1-C-29 organic compounds from fireplace combustion of wood*. Environmental Science & Technology, 2001. **35**(9): p. 1716-1728.
29. Schauer, J.J., et al., *Measurement of emissions from air pollution sources. 5. C-1-C-32 organic compounds from gasoline-powered motor vehicles*. Environmental Science & Technology, 2002. **36**(6): p. 1169-1180.

30. Slemr, F., et al., *In-flight measurement of aircraft CO and nonmethane hydrocarbon emission indices*. Journal of Geophysical Research-Atmospheres, 2001. **106**(D7): p. 7485-7494.
31. Slemr, F., et al., *In-flight measurement of aircraft non-methane hydrocarbon emission indices*. Geophysical Research Letters, 1998. **25**(3): p. 321-324.
32. Grieshop, A.P., et al., *Constraining the Volatility Distribution and Gas-Particle Partitioning of Combustion Aerosols Using Isothermal Dilution and Thermodenuder Measurements*. Environmental Science & Technology, 2009. **43**(13): p. 4750-4756.
33. Lipsky, E.M. and A.L. Robinson, *Effects of Dilution on Fine Particle Mass and Partitioning of Semivolatile Organics in Diesel Exhaust and Wood Smoke*. Environmental Science & Technology, 2006. **40**(1): p. 155-162.
34. Shrivastava, M.K., et al., *Modeling Semivolatile Organic Aerosol Mass Emissions From Combustion Systems*. Environmental Science & Technology, 2006. **40**(8): p. 2671-2677.
35. Tremmel, H.G., et al., *Observations and model calculations of jet aircraft exhaust products at cruise altitude and inferred initial OH emissions*. Journal of Geophysical Research-Atmospheres, 1998. **103**(D9): p. 10803-10816.
36. Seinfeld, J.H. and S.N. Pandis, *Atmospheric chemistry and physics: From air pollution to climate change* 1998, New York: John Wiley & Sons Inc.
37. Herndon, S.C., et al., *Aircraft hydrocarbon emissions at Oakland International Airport*. Environmental Science & Technology, 2009. **43**: p. 1730-1736.
38. Miracolo, M.A., et al., *Photo-oxidation of Low-Volatility Organics found in Motor Vehicle Emissions: Production and chemical evolution of organic aerosol mass*. Environmental Science & Technology, 2010. **44**(5): p. 1638–1643.
39. Presto, A.A., et al., *Secondary Organic Aerosol Formation from High-NO_x Photo-Oxidation of Low Volatility Precursors: n-Alkanes*. Environmental Science & Technology, 2010. **44**(6): p. 2029-2034.
40. Robinson, A.L., et al., *Rethinking organic aerosol: Semivolatile emissions and photochemical aging*. Science, 2007. **315**: p. 1259-1262.
41. Donahue, N.M., A.L. Robinson, and S.N. Pandis, *Atmospheric Organic Particulate Matter: From Smoke to Secondary Organic Aerosol*. Atmospheric Environment, 2009. **43**(1): p. 97-109.
42. Ranjan, M., et al., *Temperature Dependence of Gas-Particle Partitioning of Primary Organic Aerosol Emissions from a Small Diesel Engine*. Aerosol Science and Technology, 2012. **46**(1): p. 13-21.
43. Corporan, E., M. DeWitt, and M. Wagner, *Evaluation of soot particulate mitigation additives in a T63 engine*. Fuel Processing Technology, 2004. **85**: p. 727-742.

44. Corporan, E., et al., *Emissions Characteristics of a Turbine Engine and Research Combustor Burning a Fischer–Tropsch Jet Fuel*. Energy & Fuels, 2007. **21**(5): p. 2615-2626.
45. Corporan, E., et al., *Chemical, Thermal Stability, Seal Swell, and Emissions Studies of Alternative Jet Fuels*. Energy & Fuels, 2011. **25**(3): p. 955-966.
46. Anderson, B.E., et al., *Alternative Aviation Fuel Experiment (AAFEX)*, 2011, NASA Glenn Research Center; Langley Research Center.
47. Lipsky, E.M. and A.L. Robinson, *Design and evaluation of a portable dilution sampling system and the effects of residence time on mass emission rates*. Aerosol Science and Technology, 2005. **39**(6): p. 542-553.
48. Subramanian, R., et al., *Positive and Negative Artifacts in Particulate Organic Carbon Measurements with Denuded and Undenuded Sampler Configurations*. Aerosol Science & Technology, 2004. **38**(S1): p. 27-48.
49. Turpin, B.J., P. Saxena, and E. Andrews, *Measuring and simulating particulate organics in the atmosphere: problems and prospects*. Atmospheric Environment, 2000. **34**(18): p. 2983-3013.
50. Lee, T., S.M. Kreidenweis, and J.L. Collett, *Aerosol ion characteristics during the Big Bend Regional Aerosol and Visibility Observational Study*. Journal of the Air & Waste Management Association, 2004. **54**(585-592).
51. Canagaratna, M.R., et al., *Chemical and microphysical characterization of ambient aerosols with the aerosol mass spectrometer*. Mass Spectrometry Reviews, 2007. **26**: p. 185-222.
52. Jayne, J.T., et al., *Development of an aerosol mass spectrometer for size and composition analysis of submicron particles*. Aerosol Science and Technology, 2000. **33**(1-2): p. 49-70.
53. Allan, J.D., et al., *A generalised method for the extraction of chemically resolved mass spectra from Aerodyne aerosol mass spectrometer data*. Journal of Aerosol Science, 2004. **35**(7): p. 909-922.
54. Matsunaga, A. and P.J. Ziemann, *Gas-Wall Partitioning of Organic Compounds in a Teflon Film Chamber and Potential Effects on Reaction Product and Aerosol Yield Measurements*. Aerosol Science and Technology, 2010. **44**(10): p. 881-892.
55. Weitkamp, E.A., et al., *Organic Aerosol Formation from Photochemical Oxidation of Diesel Exhaust in a Smog Chamber*. Environmental Science & Technology, 2007. **41**(20): p. 6969-6975.
56. Grieshop, A.P., et al., *Laboratory investigation of photochemical oxidation of organic aerosol from wood fires 1: Measurement and simulation of organic aerosol evolution*. Atmospheric Chemistry and Physics, 2009. **9**: p. 1263-1277.
57. Huffman, J.A., et al., *Development and Characterization of a Fast-Stepping/Scanning Thermodenuder for Chemically-Resolved Aerosol Volatility Measurements*. Aerosol Science and Technology, 2008. **42**(5): p. 395 - 407.

58. An, W.J., et al., *Aerosol volatility measurement using an improved thermodenuder: Application to secondary organic aerosol*. Journal of Aerosol Science, 2007. **38**(3): p. 305-314.
59. Donahue, N., et al., *Coupled partitioning, dilution, and chemical aging of semivolatile organics*. Environ. Sci. Technol, 2006. **40**(8): p. 2635--2643.
60. Pankow, J.F., *An absorption model of gas/particle partitioning of organic compounds in the atmosphere*. Atmospheric Environment, 1994. **28**(2): p. 185--188.
61. Shrivastava, M.K., et al., *Effects of Gas-Particle Partitioning and Aging of Primary Emissions on Urban and Regional Organic Aerosol Concentrations*. Journal of Geophysical Research, 2008. **113**(D18301): p. doi:10.1029/2007JD009735.
62. Murphy, B.N. and S.N. Pandis, *Exploring summertime organic aerosol formation in the eastern United States using a regional-scale budget approach and ambient measurements*. Journal of Geophysical Research, 2010. **115**(D24): p. D24216.
63. Murphy, B. and S. Pandis, *Simulating the formation of semivolatile primary and secondary organic aerosol in a regional chemical transport model*. Environmental science & technology, 2009. **43**(13): p. 4722.
64. Shrivastava, M.K., et al., *Effects of gas particle partitioning and aging of primary emissions on urban and regional organic aerosol concentrations*. Journal of Geophysical Research-Atmospheres, 2008. **113**(D18): p. D18301.
65. Farina, S.C., P.J. Adams, and S.N. Pandis, *Modeling global secondary organic aerosol formation and processing with the volatility basis set: Implications for anthropogenic secondary organic aerosol*. Journal of Geophysical Research, 2010. **115**(D9): p. D09202.
66. Jathar, S., et al., *The influence of semi-volatile and reactive primary emissions on the abundance and properties of global organic aerosol*. Atmospheric Chemistry and Physics Discussions, 2011. **11**(2): p. 5493-5540.
67. Dzepina, K., et al., *Modeling the Multiday Evolution and Aging of Secondary Organic Aerosol During MILAGRO 2006*. Environmental Science & Technology, 2011. **45**(8): p. 3496-3503.
68. Dzepina, K., et al., *Evaluation of recently-proposed secondary organic aerosol models for a case study in Mexico City*. Atmos. Chem. Phys. J1 - ACP, 2009. **9**(15): p. 5681-5709.
69. Hodzic, A., et al., *Modeling organic aerosols in a megacity: potential contribution of semi-volatile and intermediate volatility primary organic compounds to secondary organic aerosol formation*. Atmos. Chem. Phys., 2010. **10**: p. 5491-5514.
70. Kroll, J.H. and J.H. Seinfeld, *Chemistry of secondary organic aerosol: Formation and evolution of low-volatility organics in the atmosphere*. Atmospheric Environment, 2008. **42**(16): p. 3593-3624.

71. Ng, N., et al., *Secondary organic aerosol formation from m-xylene, toluene, and benzene*. Atmospheric Chemistry and Physics Discussions, 2007. **7**(2): p. 4085--4126.
72. Hildebrandt, L., N. Donahue, and S. Pandis, *High formation of secondary organic aerosol from the photo-oxidation of toluene*. Atmospheric Chemistry and Physics, 2009. **9**(9): p. 2973--2986.
73. Ng, N., et al., *Secondary organic aerosol formation from m-xylene, toluene, and benzene*. Atmos. Chem. Phys, 2007. **7**: p. 3909-3922.
74. Atkinson, R. and J. Arey, *Atmospheric degradation of volatile organic compounds*. Chemical Reviews, 2003. **103**(12): p. 4605-4638.
75. Lim, Y.B. and P.J. Ziemann, *Effects of Molecular Structure on Aerosol Yields from OH Radical-Initiated Reactions of Linear, Branched, and Cyclic Alkanes in the Presence of NOx*. Environmental Science & Technology, 2009. **43**(7): p. 2328--2334.
76. Aiken, A.C., et al., *O/C and OM/OC ratios of primary, secondary, and ambient organic aerosols with high-resolution time-of-flight aerosol mass spectrometry*. Environ. Sci. Technol, 2008. **42**(12): p. 4478--4485.
77. Chhabra, P.S., R.C. Flagan, and J.H. Seinfeld, *Elemental analysis of chamber organic aerosol using an aerodyne high-resolution aerosol mass spectrometer*. Atmospheric Chemistry and Physics, 2010. **10**(9): p. 4111-4131.
78. Turpin, B.J. and H.J. Lim, *Species contributions to PM_{2.5} mass concentrations: Revisiting common assumptions for estimating organic mass*. Aerosol Science and Technology, 2001. **35**(1): p. 602-610.
79. Chase, R.E., et al., *PM Measurement Artifact: Organic Vapor Deposition on Different Filter Media*, 2004, Society of Automotive Engineers: Warrendale, PA.
80. Donahue, N.M., et al., *The coupled partitioning, dilution and chemical aging of semivolatile organics*. Environmental Science & Technology, 2006. **40**(8): p. 2635-2643.
81. Hildemann, L.M., et al., *Quantitative Characterization of Urban Sources of Organic Aerosol By High-Resolution Gas-Chromatography*. Environmental Science & Technology, 1991. **25**(7): p. 1311-1325.
82. Hinckley, D.A., et al., *Determination of vapor pressures for nonpolar and semipolar organic compounds from gas chromatographic retention data*. J. Chem. Eng. Data, 1990. **35**: p. 232-237.
83. Jensen, D.J. and E.D. Schall, *Determination of vapor pressures of some phenoxyacetic herbicides by gas-liquid chromatography*. J. Agric. Food Chem., 1966. **14**: p. 123-126.
84. Schauer, J.J., et al., *Measurement of emissions from air pollution sources. 4. C-1-C-27 organic compounds from cooking with seed oils*. Environmental Science & Technology, 2002. **36**(4): p. 567-575.

85. Seinfeld, J.H. and S.N. Pandis, *Atmospheric Chemistry and Physics*. 2006.
86. Zhang, Q., et al., *Hydrocarbon-like and oxygenated organic aerosols in Pittsburgh: insights into sources and processes of organic aerosols*. *Atmospheric Chemistry and Physics*, 2005. **5**: p. 3289-3311.
87. Sage, A.M., et al., *Evolving mass spectra of the oxidized component of organic aerosol: results from aerosol mass spectrometer analyses of aged diesel emissions*. *Atmospheric Chemistry and Physics*, 2008. **8**: p. 1139-1152.
88. Grieshop, A.P., N.M. Donahue, and A.L. Robinson, *Laboratory Investigation of Photochemical Oxidation of Organic Aerosol from Wood Fires 2: Analysis of Aerosol Mass Spectrometer Data*. *Atmospheric Chemistry and Physics*, 2009. **9**: p. 2227-2240.
89. Ng, N.L., et al., *Secondary organic aerosol formation from m-xylene, toluene, and benzene*. *Atmos. Chem. Phys.*, 2007. **7**(14): p. 3909-3922.
90. Liu, P.S.K., et al., *Transmission Efficiency of an Aerodynamic Focusing Lens System: Comparison of Model Calculations and Laboratory Measurements for the Aerodyne Aerosol Mass Spectrometer*. *Aerosol Science and Technology*, 2007. **41**(8): p. 721-733.
91. Wey, C., et al., *Aircraft particle emissions experiment (APEX)*. NASA TM-2006, 2006.
92. Presto, A.A., et al., *Secondary organic aerosol formation from high-NO_x photo-oxidation of low volatility precursors: n-alkanes*. *Environmental Science & Technology*, 2010. **44**(6): p. 2029--2034.
93. Lim, Y.B. and P.J. Ziemann, *Chemistry of secondary organic aerosol formation from OH radical-initiated reactions of linear, branched, and cyclic alkanes in the presence of NO_x*. *Aerosol Science and Technology*, 2009. **43**(6): p. 604-619.
94. Ng, N., et al., *Organic aerosol components observed in Northern Hemispheric datasets from Aerosol Mass Spectrometry*. *Atmospheric Chemistry and Physics*, 2010. **10**(10): p. 4625-4641.
95. Presto, A.A., et al., *Fine particle and organic vapor emissions from staged tests of an in-use aircraft engine*. *Atmospheric Environment*, 2011. **45**(21): p. 3603-3612.
96. Lim, Y.B. and P.J. Ziemann, *Products and mechanism of secondary organic aerosol formation from reactions of n-alkanes with OH radicals in the presence of NO_x*. *Environmental Science & Technology*, 2005. **39**(23): p. 9229-9236.
97. Chan, A.W.H., et al., *Secondary organic aerosol formation from photooxidation of naphthalene and alkyl naphthalenes: implications for oxidation of intermediate volatility organic compounds (IVOCs)*. *Atmos. Chem. Phys.*, 2009. **9**(9): p. 3049-3060.
98. Presto, A.A., et al., *Secondary organic aerosol formation from high-NO_x photo-oxidation of low volatility precursors: n-alkanes*. *Environ. Sci. Technol.*, 2010. **44**(6): p. 2029-2034.

99. Ng, N.L., et al., *Secondary organic aerosol formation from m-xylene, toluene, and benzene*. Atmospheric Chemistry and Physics, 2007. **7**: p. 3909-3922.
100. Presto, A.A., K.E.H. Hartz, and N.M. Donahue, *Secondary organic aerosol production from terpene ozonolysis. 2. Effect of NO_x concentration*. Environmental Science & Technology, 2005. **39**(18): p. 7046-7054.
101. Lane, T.E., N.M. Donahue, and S.N. Pandis, *Effect of NO_x on Secondary Organic Aerosol Concentrations*. Environmental Science & Technology, 2008. **42**(16): p. 6022–6027.
102. Song, C., K. Na, and D.R. Cocker, *Impact of the Hydrocarbon to NO_x Ratio on Secondary Organic Aerosol Formation*. Environmental Science & Technology, 2005. **39**(9): p. 3143-3149.
103. Kim, B. and J. Rachami *Aircraft Emissions Modeling Under Low Power Conditions*.
104. Unal, A., et al., *Airport related emissions and impacts on air quality: Application to the Atlanta International Airport*. Atmospheric Environment, 2005. **39**(32): p. 5787-5798.
105. Barrett, S.R.H., R.E. Britter, and I.A. Waitz, *Global Mortality Attributable to Aircraft Cruise Emissions*. Environmental Science & Technology, 2010. **44**(19): p. 7736-7742.

Appendix A. Supporting Data

Table A1. VOC emission factors for CFM56 engine in mg kg-fuel⁻¹ measured during Pittsburgh experiments.

| Load | 4% ^a | 7% ^b | 30% ^b | 85% ^a |
|--|-------------------|-----------------|-------------------|------------------|
| Ethene | 77.3 ^c | | | 28.1 |
| Acetylene | 2858.9 | | | 9.2 |
| Ethane | 115.5 | | | 83.3 |
| Propene | 696.2 | 273.34 | N.D. ^d | 6.3 |
| Propane | 37.4 | | | 32.6 |
| Propyne | 72.3 | | | N.D. |
| Cyclopropane | 2.9 | | | N.D. |
| Isobutane | 42.7 | | | 42.2 |
| Isobutene | 71.7 | | | 5.5 |
| 1-butene | 194.6 | | | 2.2 |
| 1,3-butadiene | 230.3 | 15.56 | N.D. | N.D. |
| Butane | 24.8 | | | 29.2 |
| Trans-2-butene | 61.0 | | | 4.3 |
| Cis-2-butene | 11.7 | | | 0.9 |
| 1,2-butadiene | 6.4 | | | N.D. |
| 3-methyl-1-butene | 29.5 | | | N.D. |
| Isopentane | 34.0 | | | 29.9 |
| 1-pentene | 91.2 | | | 10.8 |
| 2-methyl-1-butene | 30.3 | | | 1.0 |
| Pentane | 12.0 | | | 15.6 |
| Isoprene | 56.0 | | | N.D. |
| Trans-2-pentene | 15.7 | | | N.D. |
| Cis-2-pentene | 8.4 | | | N.D. |
| 2-methyl-2-butene | 6.0 | | | N.D. |
| 2,2-dimethylbutane | 1.5 | | | N.D. |
| Cyclopentene | 95.5 | | | N.D. |
| 4-methyl-1-pentene and 3-methyl-1-pentene | 27.2 | | | 0.7 |
| Cyclopentane | 12.6 | | | 1.8 |
| 2,3-dimethylbutane | 2.8 | | | 2.0 |
| 2-methylpentane | 50.2 | | | 1.0 |
| 3-methylpentane | 12.5 | | | N.D. |
| 2-methyl-1-pentene | 10.6 | | | N.D. |
| 1-hexene | 81.1 | | | N.D. |
| Hexane | 15.4 | | | 2.4 |
| Cis-3-hexene | 7.2 | | | N.D. |
| Trans-2-hexene | 9.5 | | | N.D. |
| 2-methyl-2-pentene | 2.1 | | | 0.6 |
| Cis-2-hexene | 6.1 | | | 14.4 |
| Trans-1,3-hexadiene | 6.3 | | | N.D. |
| Methylcyclopentane | 11.2 | | | N.D. |
| Benzene | 232.0 | 124.1 | | 72.4 |

| Load | 4% ^a | 7% ^b | 30% ^b | 85% ^a |
|--|-----------------|-------------------|-------------------|------------------|
| Cyclohexane | 51.9 | 7.36 | 6.54 | N.D. |
| 2-methylhexane and 2,3-dimethylpentane | 6.7 | | | N.D. |
| Cyclohexene | 14.5 | | | 3.7 |
| 3-methylhexane | 24.5 | | | N.D. |
| 1-heptene and 2,2,4-trimethylpentane | 61.5 | | | N.D. |
| Heptane | 5.9 | | | N.D. |
| 2,3-dimethyl-2-pentene | 7.5 | | | 1.0 |
| Methylcyclohexane | 14.4 | | | N.D. |
| 2,3,4-trimethylpentane | 5.3 | | | N.D. |
| Toluene | 84.7 | 39.95 | N.D. | 3.0 |
| 2-methylheptane | 7.1 | | | N.D. |
| 1-methylcyclohexene | 5.2 | | | N.D. |
| 4-methylheptane | 5.6 | | | 1.8 |
| 3-methylheptane | 5.7 | | | 2.9 |
| 1-octene | 5.9 | | | 1.2 |
| Octane | 7.5 | | | 0.9 |
| Ethylbenzene | 3.9 | | | 1.0 |
| m-xylene | 26.4 | 9.46 ^e | N.D. ^e | 1.1 |
| p-xylene | 4.8 | | | 3.8 |
| Styrene | 8.2 | 4.42 | N.D. | N.D. |
| o-xylene | 5.2 | 4.63 | N.D. | N.D. |
| Nonane | 36.1 | | | N.D. |
| Isopropylbenzene | 4.8 | | | 0.8 |
| α-pinene | 6.2 | | | N.D. |
| Propylbenzene | 16.6 | | | 1.4 |
| 3-ethyltoluene | 15.8 | | | N.D. |
| 4-ethyltoluene | 7.7 | | | 3.1 |
| 1,3,5-trimethylbenzene | 14.4 | | | 1.0 |
| 2-ethyltoluene | 12.6 | | | 34.2 |
| 1,2,4-trimethylbenzene and tert-butylbenzene | 41.9 | 6.73 | N.D. | 7.4 |
| Decane | 2.5 | | | 33.4 |
| Sec-butylbenzene | 39.4 | | | 1.6 |
| 1,2,3-trimethylbenzene | 47.0 | | | 1.7 |
| Limonene/indan | 7.9 | | | |
| 1,3-diethylbenzene | 10.2 | | | 1.8 |
| 1,4-diethylbenzene | 46.7 | | | 1.9 |
| Butylbenzene | 8.5 | | | |
| 1,2-diethylbenzene | 10.9 | | | 1.9 |
| Undecane | 93.7 | | | 15.8 |
| 1,2,4,5-tetramethylbenzene | 27.2 | | | |
| Naphthalene | 45.9 | | | 1.6 |
| Dodecane | 108.3 | | | 16.1 |
| Hexylbenzene | 16.6 | | | |
| Tridecane | 47.4 | | | 1.9 |

| Load | 4%^a | 7%^b | 30%^b | 85%^a |
|-------------|-----------------------|-----------------------|------------------------|------------------------|
| Tetradecane | 4.9 | | | 0.9 |

^aCanister analyzed by University of Miami.

^bCanister analyzed by EMSL, Inc.

^cBlank spaces indicate that compound was not measured.

^dNot detected.

^em+p-xylene

Table A2. Low-volatility organic emission factors (mg kg-fuel⁻¹) for CFM56 engine measured from Tenax sorbent and quartz samples collected at the Pittsburgh airport.

| Load | 4% | 7% | 30% | 85% |
|--------------------------|-----------|------------|------------|-------------|
| n-C12 ^a | 47.1±4.2 | 0.30±0.01 | 0.37±0.004 | 0.03±0.008 |
| n-C13 | 25.2±5.6 | 0.21±0.005 | 0.25±0.03 | 0.01±0.02 |
| n-C14 | 10.0±0.4 | 0.32±0.08 | 0.13±0.006 | 0.01±0.03 |
| n-C15 | 2.01±1.1 | 0.16±0.02 | 0.06±0.004 | 0.03±0.03 |
| n-C16 | 0.33±0.3 | 0.10±0.03 | 0.03±0.004 | 0.03±0.03 |
| n-C17 | 0.34±0.1 | 0.61±0.2 | 0.05±0.002 | 0.14±0.05 |
| Pristane | 0.26±0.04 | 0.39±0.09 | 0.03±0.001 | 0.007±0.04 |
| n-C18 | 0.11±0.1 | 1.32±0.4 | 0.03±0.005 | 0.03±0.02 |
| Phytane | 0.19±0.3 | 0.65±0.04 | 0.02±0.009 | 0.01±0.04 |
| n-C19 | 0.23±0.02 | 3.71±2.1 | 0.07±0.01 | 0.07±0.02 |
| n-C20 | 0.10±0.1 | 2.08±1.2 | 0.09±0.03 | 0.07±0.04 |
| n-C21 | 0.29±0.03 | 1.00±0.5 | 0.08±0.02 | 0.08±0.05 |
| n-C22 | 0.26±0.4 | 0.65±0.3 | 0.07±0.006 | 0.08±0.05 |
| n-C23 | 0.28±0.4 | 0.48±0.2 | 0.07±0.002 | 0.08±0.05 |
| n-C24 | 0.54±0.3 | 0.46±0.1 | 0.06±0.02 | 0.09±0.05 |
| n-C25 | 0.36±0.5 | 0.38±0.1 | 0.08±0.02 | 0.04±0.01 |
| n-C26 | 0.53±0.3 | 0.32±0.1 | 0.08±0.02 | 0.04±0.01 |
| n-C27 | 0.51±0.7 | 0.33±0.07 | 0.11±0.03 | 0.03±0.01 |
| n-C28 | 0.58±0.8 | 0.37±0.07 | 0.12±0.03 | 0.03±0.02 |
| n-C29 | 0.56±0.8 | 0.37±0.07 | 0.11±0.03 | 0.02±0.03 |
| n-C30 | 0.39±0.5 | 0.37±0.04 | 0.08±0.002 | 0.06±0.006 |
| n-C31 | BDL | 0.34±1e-4 | 0.09±7E-4 | BDL |
| n-C32 | BDL | BDL | 0.10±0.07 | BDL |
| n-C33 | BDL | BDL | 0.12±0.08 | 0.05±0.04 |
| n-C34 | BDL | BDL | BDL | 0.03±0.02 |
| n-C35 | BDL | BDL | BDL | BDL |
| n-C36 | BDL | BDL | BDL | BDL |
| n-C37 | BDL | BDL | BDL | BDL |
| n-C38 | BDL | BDL | BDL | BDL |
| n-C39 | BDL | BDL | BDL | BDL |
| n-undecyl cyclohexane | 0.11±0.2 | 0.16±0.01 | 0.03±0.001 | 0.009±0.009 |
| n-decyl cyclohexane | 0.74±0.2 | 0.27±0.07 | 0.05±0.008 | 0.06±0.06 |
| n-nonyl cyclohexane | 0.59±0.05 | 0.02±0.02 | 0.03±0.02 | 0.08±0.08 |
| n-octyl cyclohexane | 1.48±0.41 | 0.07±0.03 | 0.03±0.003 | 0.01±0.01 |
| n-heptyl cyclohexane | 3.20±1.0 | 0.09±0.001 | 0.05±0.003 | 0.02±0.02 |
| Naphthalene | 44.8±4.2 | 1.93±1.1 | 0.39±0.08 | 0.04±0.04 |
| 1,4-dimethyl naphthalene | 2.61±0.9 | 0.17±0.01 | 0.07±0.02 | 0.01±0.003 |
| 1,2-dimethyl naphthalene | 1.63±0.1 | 0.14±0.003 | 0.06±0.007 | 0.03±0.008 |
| 1,7-dimethyl naphthalene | 5.67±0.3 | 0.27±0.01 | 0.09±0.03 | 0.07±0.02 |

| Load | 4% | 7% | 30% | 85% |
|------------------------------|-----------|--------------|-------------|--------------|
| 2,6-dimethyl naphthalene | 7.53±1.0 | 0.37±0.01 | 0.11±0.03 | 0.07±0.02 |
| 1-methyl naphthalene | 25.2±0.8 | 1.41±0.07 | 0.27±0.05 | 0.05±0.01 |
| 2-methyl naphthalene | 44.8±0.9 | 2.55±0.1 | 0.49±0.08 | 0.11±0.03 |
| 6,10,14-TM2PD | BDL | BDL | 0.005±0.003 | BDL |
| abb-Cholestane | BDL | BDL | 0.008±0.006 | BDL |
| 18a-Trisnorhopane | BDL | BDL | BDL | BDL |
| 17a-Trisnorhopane | BDL | BDL | BDL | BDL |
| Norhopane | BDL | 0.01±1E-4 | BDL | BDL |
| 17a,21b-Hopane | BDL | BDL | BDL | BDL |
| S-Homohopane | BDL | BDL | BDL | BDL |
| R-Homohopane | 0.08±0.1 | 1.3E-03±9E-4 | BDL | BDL |
| 17b,21b-Hopane | BDL | BDL | BDL | BDL |
| S-Bishomohopane | BDL | BDL | BDL | BDL |
| R-Bishomohopane | BDL | BDL | BDL | BDL |
| Acenaphthylene | 1.75±0.03 | 0.14±0.02 | 0.04±0.006 | BDL |
| Acenaphthene | 0.41±0.05 | 0.02±0.01 | BDL | BDL |
| Fluorene | 0.57±0.06 | 0.15±0.02 | 0.03±0.003 | 6.7E-03±9E-4 |
| 9-Fluorenone | 0.68±0.2 | 0.66±0.2 | 0.09±0.01 | 0.12±0.06 |
| Phenanthrene | 0.44±0.1 | 0.75±0.4 | 0.01±0.01 | 0.05±0.06 |
| Anthracene | BDL | 0.09±0.2 | 0.03±0.002 | 0.01±0.004 |
| 9,10-Anthracenedione | 1.15±0.7 | 0.98±0.1 | 0.34±0.2 | 0.31±0.2 |
| Fluoranthene | BDL | 0.17±0.05 | 0.06±0.01 | 0.04±0.02 |
| Pyrene | BDL | 0.23±0.04 | 0.06±0.01 | 0.05±0.03 |
| Retene | BDL | BDL | 0.06±0.04 | 0.02±0.01 |
| Benzo[c]phenanthrene | BDL | BDL | 0.04±0.02 | 0.02±0.01 |
| Benz[a]anthracene + Chrysene | BDL | BDL | 0.09±0.06 | 0.03±0.03 |
| IVOC UCM | 1340±400 | 469±141 | 40±12 | 39±16 |
| SVOC UCM | 27±8 | 38±11 | 33±10 | 16±6 |
| Σ 3-ring PAH | 5.00 | 2.79 | 0.61 | 0.52 |
| Σ 4-ring PAH | 0.0 | 0.40 | 0.25 | 0.14 |
| Σ Naphthalenes | 132.3 | 6.85 | 1.49 | 0.38 |
| Σ Speciated IVOC | 227.4 | 18.2 | 2.59 | 1.08 |
| Σ Speciated SVOC | 6.2 | 6.79 | 1.58 | 1.14 |
| Σ Speciated LVOC/ELVOC | 0.0 | 0.34 | 0.31 | 0.09 |

^an-CXX indicates *n*-alkanes. ^bBDL = Below detection limit

Table A3. VOC emission factors for T63 engine in mg kg-fuel⁻¹ measured during Wright Patterson experiments

| Emission Factors (mg/kg-Fuel) | Idle | | | Cruise | |
|----------------------------------|--------|-------|--------|--------|-------|
| | JP8 | FT | Blend | JP8 | FT |
| Ethene | 176.14 | 99.59 | 186.35 | 3.73 | 0.86 |
| Acetylene | 59.84 | 75.45 | 81.30 | 2.77 | 0.78 |
| Ethane | 7.37 | 10.15 | 10.02 | 2.69 | 0.31 |
| Propene | 29.98 | 34.24 | 43.40 | 0.10 | 0.28 |
| Propane | 0.02 | 0.45 | 0.28 | -0.21 | -0.14 |
| Propyne | 2.53 | 3.44 | 3.80 | 0.04 | 0.02 |
| i-Butane | -0.01 | 3.31 | 0.03 | 0.01 | -0.02 |
| i-Butene | 1.81 | 8.61 | 6.62 | 0.00 | 0.00 |
| 1-Butene | 5.92 | 2.83 | 5.98 | 0.02 | 0.02 |
| 1,3-Butadiene | 6.22 | 3.22 | 0.00 | 0.04 | 0.02 |
| Butane | 0.13 | 5.95 | 5.04 | 0.07 | 0.06 |
| t-2-Butene | 0.78 | 1.99 | 1.66 | 0.02 | 0.01 |
| c-2-Butene | 0.21 | 1.49 | 1.24 | 0.01 | 0.02 |
| 1,2-Butadiene | 0.02 | 0.20 | 0.08 | 0.00 | 0.00 |
| i-Pentane | 0.00 | 0.00 | 0.12 | 0.00 | 0.00 |
| 1-Pentene | 0.77 | 0.18 | 0.34 | 0.00 | 0.00 |
| 2-Methyl-1-Butene | 0.49 | 0.00 | 0.30 | 0.00 | 0.00 |
| Pentane | 0.10 | 1.07 | 0.02 | 0.00 | 0.00 |
| Isoprene | 0.85 | 0.37 | 1.19 | 0.00 | 0.00 |
| t-2-Pentene | 1.00 | 0.46 | 0.97 | 0.00 | 0.00 |
| c-2-Pentene | 0.58 | 1.33 | 0.38 | 0.00 | 0.00 |
| 2-Methyl-2-Butene | 0.09 | 0.23 | 0.31 | 0.00 | 0.00 |
| 2,2-Dimethylbutane | 0.41 | 0.10 | 0.25 | 0.00 | 0.00 |
| Cyclopentene | 0.02 | 0.64 | 0.17 | 0.00 | 0.00 |
| Cyclopentane | 0.26 | 0.76 | 0.35 | 0.00 | 0.00 |
| 2,3-Dimethylbutane | 0.34 | 0.24 | 0.54 | 0.03 | 0.00 |
| 2-Methylpentane | 0.00 | 0.02 | 0.04 | 0.01 | 0.00 |
| 3-Methylpentane | 0.07 | 0.08 | 0.23 | 0.00 | 0.00 |
| 2-Methyl-1-Pentene | 0.03 | 0.01 | 0.04 | 0.00 | 0.00 |

| Emission Factors (mg/kg-Fuel) | Idle | | | Cruise | |
|--------------------------------------|------|------|-------|--------|------|
| | JP8 | FT | Blend | JP8 | FT |
| Hexane | 1.49 | 0.19 | 0.99 | 0.43 | 0.00 |
| t-2-Hexene | 0.07 | 0.09 | 0.10 | 0.00 | 0.00 |
| c-2-Hexene | 0.13 | 0.20 | 0.24 | 0.00 | 0.00 |
| 1,3-Hexadiene | 0.05 | 0.17 | 0.07 | 0.00 | 0.00 |
| Methylcyclopentane | 0.02 | 0.09 | 0.07 | 0.00 | 0.00 |
| 2,4-Dimethylpentane | 0.01 | 0.17 | 0.15 | 0.00 | 0.00 |
| Benzene | 2.14 | 1.18 | 2.25 | 0.03 | 0.00 |
| Cyclohexane | 0.02 | 0.37 | 0.04 | 0.00 | 0.00 |
| 2-Methylhexane + 2,3-Dimethylpentane | 0.14 | 0.06 | 0.17 | 0.00 | 0.00 |
| Cyclohexene | 0.03 | 0.06 | 0.15 | 0.00 | 0.00 |
| 3-Methylhexane | 0.02 | 0.01 | 0.05 | 0.00 | 0.00 |
| c-1,3-Dimethylcyclopentane | 0.00 | 0.07 | 0.01 | 0.00 | 0.00 |
| 1-Heptene | 0.01 | 0.05 | 0.06 | 0.00 | 0.00 |
| Heptane | 0.64 | 0.09 | 0.56 | 0.00 | 0.00 |
| 2,3-Dimethyl-2-Pentene | 0.07 | 0.03 | 0.02 | 0.00 | 0.00 |
| Methylcyclohexane | 0.03 | 0.03 | 0.08 | 0.00 | 0.00 |
| 2,3,4-Trimethylpentane | 0.04 | 0.13 | 0.13 | 0.00 | 0.00 |
| Toluene | 0.61 | 0.23 | 0.58 | 0.01 | 0.00 |
| 2-Methylheptane | 0.04 | 0.03 | 0.05 | 0.00 | 0.00 |
| 4-Methylheptane | 0.02 | 0.04 | 0.03 | 0.00 | 0.00 |
| 3-Methylheptane | 0.03 | 0.02 | 0.02 | 0.00 | 0.00 |
| Octane | 0.11 | 0.02 | 0.08 | 0.00 | 0.00 |
| Ethylbenzene | 0.10 | 0.27 | 0.35 | 0.00 | 0.00 |
| m-Xylene | 0.16 | 0.25 | 0.06 | 0.00 | 0.00 |
| p-Xylene | 0.08 | 0.15 | 0.14 | 0.00 | 0.00 |
| Styrene | 0.05 | 0.02 | 0.15 | 0.00 | 0.00 |
| o-Xylene | 0.09 | 0.30 | 0.41 | -0.01 | 0.00 |
| Nonane | 0.32 | 0.01 | 0.42 | 0.00 | 0.00 |
| i-Propylbenzene | 0.03 | 0.36 | 0.34 | 0.00 | 0.00 |
| a-Pinene | 0.04 | 0.25 | 0.23 | 0.00 | 0.00 |
| Propylbenzene | 0.05 | 0.13 | 0.16 | 0.00 | 0.00 |

| Emission Factors (mg/kg-Fuel) | Idle | | | Cruise | |
|--|-------------|-----------|--------------|---------------|-----------|
| | JP8 | FT | Blend | JP8 | FT |
| 3-Ethyltoluene | 0.04 | 0.26 | 0.10 | 0.00 | 0.00 |
| 4-Ethyltoluene | 0.09 | 0.22 | 0.34 | 0.00 | 0.00 |
| 1,3,5-Trimethylbenzene | 0.06 | 0.02 | 0.25 | 0.00 | 0.00 |
| 2-Ethyltoluene | 0.06 | 0.04 | 0.17 | 0.01 | 0.00 |
| 1,2,4-Trimethylbenzene/tert-Butylbenzene | 0.07 | 0.11 | 0.70 | 0.00 | 0.00 |
| Decane | 0.01 | 0.45 | 0.84 | 0.04 | 0.00 |
| 1,2,3-Trimethylbenzene | 0.01 | 0.04 | 0.21 | 0.00 | 0.00 |
| Indan | 0.05 | 0.07 | 0.21 | 0.00 | 0.00 |
| 1,3-Diethylbenzene | 0.04 | 0.51 | 0.63 | 0.00 | 0.00 |
| 1,4-Diethylbenzene | 0.01 | 0.21 | 0.35 | 0.01 | 0.00 |
| Butylbenzene | 0.01 | 0.31 | 0.09 | 0.00 | 0.00 |
| Undecane | 0.01 | 0.10 | 0.64 | 0.00 | 0.00 |

Table A4. Low-volatility organic emission factors (mg kg-fuel⁻¹) for T63 engine measured from Tenax sorbent and quartz samples collected at the Wright Patterson Air Force Base.

| Compound | IDLE | | | CRUISE | |
|----------------------|--------|--------|--------|--------|--------|
| | JP8 | Blend | FT | JP8 | FT |
| 17b,21b-Hopane | 0.0023 | 0.0021 | 0.0000 | 0.0 | 0.0 |
| R-Homohopane | 0.002 | 0.001 | 0.000 | 0.0 | 0.0 |
| Benz[a]anthracene | 0.042 | 0.028 | 0.015 | 0.0054 | 0.0004 |
| Benzo[c]phenanthrene | 0.005 | 0.004 | 0.003 | 0.0039 | 0.0002 |
| Retene | 0.022 | 0.029 | 0.017 | 0.00 | 0.00 |
| Pyrene | 0.058 | 0.037 | 0.086 | 0.144 | 0.006 |
| Fluoranthene | 0.057 | 0.042 | 0.099 | 0.155 | 0.010 |
| 9,10-Anthracenedione | 0.25 | 0.57 | 0.41 | 2.64 | 3.08 |
| Anthracene | 1.12 | 0.055 | 0.049 | 0.0000 | 0.0000 |
| Phenanthrene | 0.017 | 0.003 | 1.133 | 0.0810 | 0.018 |
| 9-Fluorenone | 1.12 | 0.018 | 0.27 | 0.15 | 0.074 |
| Fluorene | 3.13 | 0.16 | 0.42 | 0.012 | 0.0004 |
| Acenaphthene | 0.90 | 0.005 | 0.035 | 0.0008 | 0.0006 |
| Acenaphthylene | 1.23 | 0.00 | 0.40 | 0.00 | 0.000 |
| Naphthalene | 11.23 | 17.59 | 1.07 | 0.32 | 0.047 |
| 17a-Trisnorhopane | 0.000 | 0.000 | 0.012 | 0.000 | 0.000 |
| abb-Cholestane | 0.000 | 0.000 | 0.000 | 0.000 | 0.000 |
| 6,10,14-TM2PD | 0.007 | 0.000 | 0.000 | 0.012 | 0.000 |
| C39 n-alkane | 0.000 | 0.008 | 0.000 | 0.000 | 0.000 |
| C38 n-alkane | 0.000 | 0.006 | 0.000 | 0.000 | 0.000 |
| C37 n-alkane | 0.004 | 0.031 | 0.017 | 0.000 | 0.000 |
| C36 n-alkane | 0.000 | 0.002 | 0.000 | 0.002 | 0.000 |
| C35 n-alkane | 0.04 | 0.29 | 0.12 | 0.0013 | 0.0021 |
| C34 n-alkane | 1.80 | 0.85 | 0.65 | 0.0003 | 0.0000 |
| C33 n-alkane | 1.71 | 0.74 | 0.57 | 0.0031 | 0.014 |
| C32 n-alkane | 2.11 | 1.21 | 1.00 | 0.0089 | 0.025 |
| C31 n-alkane | 2.54 | 1.60 | 1.30 | 0.034 | 0.038 |
| C30 n-alkane | 1.51 | 0.99 | 0.78 | 0.034 | 0.028 |
| C29 n-alkane | 0.86 | 0.64 | 0.45 | 0.0253 | 0.0075 |
| C28 n-alkane | 0.23 | 0.14 | 0.087 | 0.019 | 0.0059 |
| C27 n-alkane | 2.10 | 1.76 | 1.25 | 0.14 | 0.068 |
| C26 n-alkane | 0.25 | 0.29 | 0.0057 | 0.027 | 0.008 |
| C25 n-alkane | 4.72 | 4.41 | 3.08 | 1.86 | 0.26 |
| C24 n-alkane | 1.52 | 0.15 | 0.00 | 0.00 | 0.00 |
| C23 n-alkane | 6.62 | 5.98 | 4.69 | 3.69 | 0.45 |
| C22 n-alkane | 0.0 | 0.2931 | 0.00 | 0.00 | 0.00 |

| Compound | IDLE | | | CRUISE | |
|-------------------------|--------|--------|-------|--------|--------|
| | JP8 | Blend | FT | JP8 | FT |
| C21 n-alkane | 0.48 | 0.68 | 0.46 | 0.11 | 0.00 |
| C20 n-alkane | 0.0 | 0.0705 | 0.00 | 0.0132 | 0.00 |
| C19 n-alkane | 0.012 | 0.00 | 0.00 | 0.32 | 0.0045 |
| Phytane | 0.71 | 0.26 | 0.04 | 0.19 | 0.0088 |
| C18 n-alkane | 1.57 | 0.43 | 0.07 | 0.43 | 0.0096 |
| n-Undecylcyclohexane | 0.37 | 0.13 | 0.01 | 0.0057 | 0.0015 |
| Pristane | 6.33 | 2.29 | 0.39 | 0.30 | 0.12 |
| 1,4-Dimethylnaphthalene | 27.98 | 16.73 | 0.13 | 0.00 | 0.01 |
| n-Nonylcyclohexane | 6.12 | 4.44 | 0.40 | 0.07 | 0.08 |
| C17 n-alkane | 12.28 | 5.90 | 0.91 | 0.49 | 0.23 |
| n-Decylcyclohexane | 2.25 | 0.93 | 0.11 | 0.01 | 0.03 |
| C16 n-alkane | 37.61 | 22.48 | 3.32 | 0.96 | 1.23 |
| 1,2-Dimethylnaphthalene | 9.30 | 5.60 | 0.57 | 0.18 | 0.13 |
| n-Octylcyclohexane | 8.94 | 6.53 | 0.25 | 0.03 | 0.02 |
| C15 n-alkane | 64.20 | 41.38 | 4.10 | 0.74 | 0.97 |
| 1,7-Dimethylnaphthalene | 56.72 | 36.97 | 0.88 | 0.16 | 0.18 |
| C14 n-alkane | 102.44 | 55.55 | 3.19 | 0.41 | 0.34 |
| 2,6-Dimethylnaphthalene | 43.50 | 22.07 | 0.69 | 0.12 | 0.12 |
| n-Heptylcyclohexane | 11.93 | 7.98 | 0.14 | 0.00 | 0.00 |
| 1-Methylnaphthalene | 18.50 | 13.71 | 0.20 | 0.06 | 0.02 |
| C13 n-alkane | 114.99 | 69.15 | 3.10 | 0.21 | 0.19 |
| 2-Methylnaphthalene | 31.49 | 16.97 | 0.26 | 0.11 | 0.04 |
| C12 n-alkane | 116.35 | 63.85 | 3.55 | 0.00 | 0.06 |
| Totals | | | | | |
| spec IVOC | 693.06 | 412.78 | 26.56 | 8.10 | 7.03 |
| spec SVOC | 22.47 | 17.17 | 12.65 | 5.84 | 0.89 |
| spec LVOC/ELVOC | 3.55 | 1.89 | 1.35 | 0.007 | 0.016 |

Appendix B. List of Scientific/Technical Publications

Articles in peer-reviewed journals

- Grieshop, A. P., M. A. Miracolo, N. M. Donahue and A. L. Robinson (2009). "Constraining the Volatility Distribution and Gas-Particle Partitioning of Combustion Aerosols Using Isothermal Dilution and Thermodenuder Measurements." Environmental Science & Technology **43**(13): 4750-4756.
- Robinson, A. L., A. P. Grieshop, N. M. Donahue and S. W. Hunt (2010). "Updating the Conceptual Model for Fine Particle Mass Emissions from Combustion Systems." Journal of the Air & Waste Management Association **60**(10): 1204–1222.
- Presto, A. A., N. T. Nguyen, M. Ranjan, A. J. Reeder, E. M. Lipsky, C. J. Hennigan, M. A. Miracolo, D. D. Riemer and A. L. Robinson (2011). "Fine particle and organic vapor emissions from staged tests of an in-use aircraft engine." Atmospheric Environment **45**(21): 3603-3612.
- Miracolo, M. A., C. J. Hennigan, M. Ranjan, N. T. Nguyen, T. D. Gordon, E. M. Lipsky, A. A. Presto, N. M. Donahue and A. L. Robinson (2011). "Secondary aerosol formation from photochemical aging of aircraft exhaust in a smog chamber." Atmospheric Chemistry and Physics **11**(9): 4135-4147.
- Ranjan, M., A. A. Presto, A. A. May and A. L. Robinson (2012). "Temperature Dependence of Gas–Particle Partitioning of Primary Organic Aerosol Emissions from a Small Diesel Engine." Aerosol Science and Technology **46**(1): 13-21.

In preparation

- Miracolo, M. A., G. T. Drozd, S. Jathar, A. A. Presto, E. M. Lipsky, E. Corporan, A. L. Robinson "Alternative aviation fuels and air pollution emissions: 2. secondary particulate matter formation" to be submitted to Environmental Science & Technology
- Drozd, G.T., M. A. Miracolo, A. A. Presto, E. M. Lipsky, E. Corporan, A. L. Robinson "Alternative aviation fuels and air pollution emissions: 1. primary particulate matter emissions" to be submitted to Energy & Fuels
- Jathar, S., M. A. Miracolo, A. A. Presto, C. J. Hennigan, A. May, N. M. Donahue, P. J. Adams, A. L. Robinson "Modeling the formation and properties of secondary organic aerosol from the photo-oxidation of low volatility organics: Problem

formulation and application to aircraft exhaust,” to be submitted to Atmospheric Chemistry and Physics.

Hennigan, C. J., A. A. Presto, N. Nguyen, A.L. Robinson "Determination of volatility distributions from combustion systems using Gas Chromatography Mass Spectroscopy: 2. Method Development" to be submitted to Aerosol Science & Technology.

Presto, A.A., C.J. Hennigan, N. Nguyen, A.L. Robinson "Determination of volatility distributions from combustion systems using Gas Chromatography Mass Spectroscopy: 2. Demonstration and application" to be submitted to Aerosol Science & Technology.

Conference or symposium abstracts

S. H. Jathar, M. A. Miracolo, N. T. Nguyen, A. A. Presto, A. L. Robinson, "Modeling the Formation and Properties of Secondary Organic Aerosol From Aircraft Exhaust", 14th Annual Environmental Chemistry Student Symposium, Pennsylvania State University, PA, April 8-9 2011.

A.L. Robinson, "Measurement and simulation of volatile particle emissions from military aircraft," Partners in Environmental Technology Technical Symposium & Workshop Washington DC, November 29 – December 1, 2011.

A.L. Robinson, A.A. Presto, M. Ranjan, N. Nguyen, C.J. Hennigan, M.A. Miracolo, G. Drozd, A. Reeder, E.M. Lipsky, P.J. Adams, N.M. Donahue "Measurement and Modeling of Volatile Particle Emissions from Military Aircraft," Partners in Environmental Technology Technical Symposium & Workshop Washington DC, November 29 – December 1, 2011.

S. H. Jathar, M. A. Miracolo, N. T. Nguyen, A. A. Presto, G. T. Drozd, A. L. Robinson, "Modeling Fine Particle Pollution From Aircraft Using JP8, Fischer-Tropsch and Blend Fuels", 28th Annual International Pittsburgh Coal Conference, Pittsburgh, PA, September 12-15 2011.

S. H. Jathar, A. A. Presto, M. A. Miracolo, N. T. Nguyen, A. A. May, P. J. Adams, A. L. Robinson, "Modeling SOA Formation from Combustion Emissions: Application to Aircraft Exhaust", American Association for Aerosol Research 30th Annual Conference, Orlando, FL, October 3-7 2011.

S. H. Jathar, A. A. Presto, M. A. Miracolo, N. T. Nguyen, A. A. May, P. J. Adams, A. L. Robinson, "Modeling the Formation and Properties of Secondary Organic Aerosol From Low-Volatility Organic Emissions of Combustion Systems", 3rd International Aerosol Modeling Algorithms, Davis, CA, November 30 - December 2, 2011.

- A.L. Robinson, A.A. Presto, M. Ranjan, N. Nguyen, C.J. Hennigan, M.A. Miracolo, G. Drozd, A. Reeder, E.M. Lipsky, P.J. Adams, N.M. Donahue “Measurement and Modeling of Volatile Particle Emissions from Military Aircraft,” Partners in Environmental Technology Technical Symposium & Workshop Washington DC, November 30 – December 2, 2010.
- A.L. Robinson, A.A. Presto, M. Ranjan, N. Nguyen, C.J. Hennigan, M.A. Miracolo, G. Drozd, A. Reeder, E.M. Lipsky, P.J. Adams, N.M. Donahue “Measurement and Modeling of Volatile Particle Emissions from Military Aircraft,” Partners in Environmental Technology Technical Symposium & Workshop Washington DC, November 30 – December 2, 2010.
- M.A. Miracolo, A.A. Presto, C.J. Hennigan, N.T. Nguyen, M. Ranjan, A.L. Robinson, “Secondary Aerosol Formation from Photo-oxidation of Aircraft Exhaust,” 2010 International Aerosol Conference, Helsinki Finland, August 29-September 3, 2010.
- A.L. Robinson, A.A. Presto, M. Ranjan, N. Nguyen, C.J. Hennigan, M.A. Miracolo, G. Drozd, A. Reeder, E.M. Lipsky, P.J. Adams, N.M. Donahue “Measurement and Modeling of Volatile Particle Emissions from Military Aircraft,” Partners in Environmental Technology Technical Symposium & Workshop Washington DC, November 30 – December 2, 2009.
- A. L. Robinson, C. J. Hennigan, M. A. Miracolo, M. Ranjan, N. Nguyen, A. A. Presto, N. M. Donahue, “Secondary Organic Aerosol Formation from Photochemical Aging of Aircraft Exhaust,” American Association of Aerosol Research 28th Annual Conference (AAAR 2009), Minneapolis, MN, October 26–30, 2009.
- M. Ranjan, A. Reeder, N. Nguyen, M. A. Miracolo, C. J. Hennigan, A. A. Presto, B. Anderson, S. Herndon, R. Miake-Lye, A. L. Robinson, “Volatile Particle Matter and Primary Organic Aerosol Emissions from Civilian and Military Aircraft,” American Association of Aerosol Research 28th Annual Conference (AAAR 2009), Minneapolis, MN, October 26–30, 2009.